PENETRATING PROBES IN RELATIVISTIC HEAVY ION COLLISIONS

GuangYou Qin

Department of Physics
McGill University
Montréal, Québec H3A 2T8
Canada

A Thesis submitted to the
Faculty of Graduate Studies and Research
in partial fulfillment of the requirements for the degree of
Doctor of Philosophy

Your file Votre référence
ISBN: 978-0-494-66657-9
Our file Notre référence
ISBN: 978-0-494-66657-9

TO MY FATHER AND IN MEMORY OF MY MOTHER

Contents

List of Figures

Statement of originality

The work embodied in this dissertation incorporates the outcome of original research that I have undertaken during my doctoral study at McGill. I acknowledge the important guidance of my supervisor Prof. Charles Gale and helpful discussions with my collaborators. I have performed all the calculations in this thesis and participated in the writing of all the papers listed below.

In Chapter 2, we present a new channel of photon production from a charge-asymmetric hot and dense matter. This material has been published in: *Guang-You Qin, Abhijit Majumder and Charles Gale, Phys. Rev.* **C75**, *064909 (2007), hep-ph/0703312.* The results were also presented in the proceedings of *the 19th International Conference on Ultra-Relativistic Nucleus-Nucleus Collisions (QM2006): International Journal of Modern Physics* **E16**, *Issue 7/8, 2350 (2007), hep-ph/0703026.*

In Chapter 4, we perform a systematic analysis of the radiative jet energy loss at high transverse momentum in a relativistic hydrodynamical medium. The results have been published in: *Guang-You Qin, Jörg Ruppert, Simon Turbide, Charles Gale, Chiho Nonaka and Steffen A. Bass, Phys. Rev.* **C76**, *064907 (2007), arXiv:0705.2575 [hep-ph].* The LHC prediction was presented at *the Workshop on Heavy Ion Collisions at the LHC: Last Call for Predictions (2007): Guang-You Qin, Jörg Ruppert, Simon Turbide, Charles Gale and Sangyong Jeon, arXiv:0705.4468 [hep-ph].*

In Chapter 5, we develop the first fully consistent model to incorporate both radiative and collisional energy loss of hard jets in a quark-gluon plasma in the same formalism. This work has been published in: *Guang-You Qin, Jörg Ruppert, Charles Gale, Sangyong Jeon, Guy D. Moore and Munshi G. Mustafa, Phys. Rev. Lett.* **100**, *072301 (2008), arXiv:0710.0605.* The results were also presented in the proceedings of *the 20th International Conference on Ultra-Relativistic Nucleus-Nucleus Collisions*

(QM2008): arXiv:0805.4594 [hep-ph].

In Chapter 6, we discuss the radiative and collisional energy loss of photon-tagged jets at high transverse momentum in relativistic heavy ion collisions including all sources of photon production. The paper for this work is *in preparation.*

Chapter 1 and Chapter 3 constitute a review; the relevant articles have been acknowledged in the text and a list of references is also given in the bibliography.

Abstract

In this dissertation, the phenomenology of electromagnetic radiation and high transverse momentum jets in relativistic heavy ion collisions is investigated. These are two very important probes to study the strongly interacting matter at extreme temperatures and/or densities and to investigate the possibility of a phase transition between hadronic matter and quark-gluon plasma (QGP). First, a new channel of direct photon production from a charge-asymmetric QGP is explored in the effective theory of quantum chromodynamics (QCD) at high temperature. The photon production from this new channel is found to be suppressed compared to QCD annihilation process and Compton scattering at low baryon density, but might assume significance in baryon-rich matter. Second, the radiative jet energy loss in a three-dimensional ideal hydrodynamical medium is studied for Au+Au collisions at Relativistic Heavy Ion Collider (RHIC). A systematic analysis of the nuclear modification factor R_{AA} is presented for π^0 production at high p_T in central and non-central collisions, at mid and forward rapidity. Third, jet energy loss by elastic collisions is consistently incorporated in the same formalism and applied to the study of jet quenching at RHIC. It is found that the nuclear modification factor R_{AA} for π^0 in relativistic heavy ion collisions is sensitive to both collisional and radiative energy loss, while the average energy loss is less affected by the inclusion of collisional energy loss. Last, the nuclear suppression of photon-tagged jets at high p_T is studied by incorporating not only direct photons, but the additional sources from fragmentation and jet-plasma interaction. We find that these additional sources are very important for a complete study of the correlations between hard photons and hadrons and even dominate in some kinetic regime.

Résumé

Dans cette dissertation, nous étudions la phénomenologie de la radiation électromagnétique et des jets à grande quantité de mouvement transverse dans les collisions d'ions lourds relativistes. Ces observables permettent de sonder la matière en intéraction forte à des conditions extrêmes de température et/ou de densité et d'investiguer la possibilité qu'il y ait une transition de phase de la matière hadronique au plasma quark-gluon (QGP). En premier lieu, nous explorons un nouveau mode de production des photons directs à partir d'un QGP chargé, à l'aide d'une théorie effective de la chromodynamique quantique (QCD) à haute température. Nous démontrons que la production de photons dans ce mode n'est pas favorisée à basse densité de baryon, par rapport aux processus d'annihilation par l'intéraction forte et de la diffusion de Compton. Par contre, cette production de photons devient significative dans la matière riche en baryons. En deuxième lieu, nous étudions la perte d'énergie radiative des jets dans un milieu hydrodynamique parfait en trois dimensions, d'espace pour les collisions Au+Au au "Relativistic Heavy Ion Collider (RHIC)". Une analyse systématique du facteur de modification nucléaire est présentée pour la production de π^0 à haut p_T dans les collisions centrales et non-centrales, ainsi qu'à rapidité centrale et non-centrale. En troisième lieu, la perte en énergie des jets par collisions élastiques est inclue dans le même formalisme et appliquée à l'étude de "l'extinction des jets" à RHIC. Nous trouvons que le facteur de modification nucléaire R_{AA} pour le π_0 dans les collisions d'ions lourds relativistes est sensible et à la perte en énergie par collisions, et à la perte en énergie par rayonnement, tandis que la moyenne de la perte en énergie est moins touchée par l'inclusion de la perte en énergie par collisions. Finalement, la suppression nucléaire des jets avec photons marqués à haut p_T est étudiée en incluant les photons directs, ainsi que les contributions venant de la fragmentation et de l'intéraction des jets avec le plasma. Nous démontrons que ces contributions additionnelles sont nécessaires dans l'étude des corrélations entre les photons durs et les hadrons, et peut même dominer dans certaines régions cinématiques.

Acknowledgments

I would like to express my deep and sincere gratitude to my supervisor, Prof. Charles Gale, for his important help and support throughout my study at McGill. It was my honor to be his graduate student and pursue my doctoral degree under his guidance. I benefited so much from his great knowledge and deep insight in physics as well as in life. His vital contribution made him a backbone of this dissertation.

I am grateful to Prof. Sangyong Jeon and Prof. Guy D. Moore for their constructive comments and insightful suggestions. I am deeply indebted to Dr. Abhijit Majumder, Dr. Jörg Ruppert and Dr. Simon Turbide for a variety of important assistances. I give my warm thanks to Prof. Steffen A. Bass, Prof. Jean Barrette, Prof. Subal Das Gupta, Prof. Munshi M. Mustafa, Prof. Chiho Nonaka, Dr. Thorsten Renk and Prof. Dinesh K. Srivastava for valuable discussions. I would like to address my special thanks to Prof. Ulrich Heniz and Prof. Berndt Müller for their encouragement.

I appreciate many stimulating and interesting conversations with my colleagues, Dr. Alex Bourque, Dr. Jean-Sebastien Gagnon, Francois Fillion-Gourdeau, Simon Caron-Huot, Mohammed Mia and Gojko Vujanovic. I am thankful to all my Chinese friends for a lot of help and fun during my stay in Montreal.

I would like to thank my family for their constant love and unconditional support throughout my life. I give my deepest gratitude to my wife Yang Li for her understanding, patience and endless encouragement. This dissertation would have been impossible without them.

1

Basic phenomenology of relativistic heavy ion collisions

1.1 Introduction

One of main reasons for physicists around the world being interested in studying physical phenomena in relativistic heavy-ion collisions is the large amount of energy involved in those collisions. For example, the Relativistic Heavy-Ion Collider (RHIC) at Brookhaven National Laboratory (BNL) was designed to accelerate gold (Au) nuclei to an energy of about 200 GeV per nucleon pair [1]. At the Large Hadron Collider (LHC) at the European Organization for Nuclear Research (CERN), lead (Pb) nuclei will be accelerated up to 5.5 TeV per nucleon pair, and the center-of-mass energy for lead-lead collisions at the LHC will exceed that available for gold-gold collisions at RHIC by a factor of about 30.

On the other hand, experimental results have shown that the collisions between two high energy nuclei have large cross sections, and are highly inelastic [8]. The two nuclei, after they collide with each other, lose a large fraction of their initial energies. The deposited energy is then transformed into intense heat and new particles, which are captured by the detectors. Furthermore, since the two nuclei are travelling at nearly the speed of light, they appear initially as two very thin disks (pancakes), owing to Lorentz contraction. Therefore, the elementary nucleon-nucleon collisions in the two colliding nuclei occur very close in space and nearly at the same time. As a result, a large amount of energy is deposited in a small space-time volume, leading to very high energy densities in the center-of-mass region. In fact, the study of nuclear

[1] For the details of the latest developments at RHIC, please refer to the review papers [1, 2, 3, 4, 5, 6, 7].

matter under extreme conditions is one of the important objectives of relativistic heavy ion collisions.

Theoretically, high energy heavy ion collisions may provide a valuable tool to further our understanding of strongly-interacting matter. The deep inelastic electron-proton experiments in the early 1970s indicated that nucleons have an internal structure, made out of strongly-interacting quarks and gluons. It is unanimously acknowledged that quantum chromodynamics (QCD) [9, 10] is the well-established theory of strong interaction as it is able to correctly describe the most important features of quark-gluon interactions and provided plenty of successful predictions.

According to QCD, quarks and gluons are confined inside hadrons; free quarks and gluons are never observable in physical vacuum. One of the predictions of QCD is that a deconfined state of quarks and gluons called quark-gluon plasma (QGP) is expected to exist at sufficiently high energy density. This has been confirmed by lattice QCD calculations [11, 12, 13], which simulate the strong interaction between quarks and gluons on a discrete lattice. It is the hope of heavy ion physicists to create such a new phase of matter in high energy nuclear collisions and study the critical phenomena related to the phase transition between hadronic matter and quark-gluon plasma, such as color confinement and chiral symmetry breaking [14, 15]. From a general point of view, it is also of great theoretical interest and importance to investigate the physics of nuclear matter under extremely high temperatures and densities. In a word, relativistic heavy ion collisions may provide new insights into the physics of strongly-interacting QCD matter and permit the exploration of the detailed structure of the QCD phase diagram.

1.2 Confinement and chiral symmetry breaking in QCD

Quantum chromodynamics is a non-Abelian gauge field theory of $SU(3)$ group describing the dynamic of interactions between colors. The fundamental color degrees of freedoms are spin-$\frac{1}{2}$ particles called quarks with $N_c = 3$ colors, and spin-1 gauge bosons known as gluons with $N_c^2 - 1 = 8$ colors. There are at least six different flavors

of quarks: up, down, strange, charm, beauty and top.

Let ψ_f denote the quark field of flavor f, with flavor index $f = u, d, s, c, b, t$. From quantum field theory [16, 17], the Lagrangian for free quarks is

$$\mathcal{L}_0 = \sum_f \bar{\psi}_f (i\gamma^\mu \partial_\mu - m_f)\psi_f \tag{1.1}$$

where $\bar{\psi} = \psi^\dagger \gamma^0$. The Dirac matrices γ^μ are defined by the anti-commutators $\{\gamma^\mu, \gamma^\nu\} = 2g^{\mu\nu}$, and m_f is the quark mass of flavor f. The free Lagrangian has a global symmetry under $SU(3)$ transformation

$$\psi_f \rightarrow \psi'_f = \exp\left(ig_s T^a \theta_a\right) \psi_f \tag{1.2}$$

where T^a denote the generators of the Lie algebra of $SU(3)$ group, with $a = 1, \cdots, 8$, and θ_a are arbitrary phase parameters. In the fundamental representation of the $SU(3)$ group, $T^a = \lambda_a/2$, where $\lambda_1, \cdots, \lambda_8$ are eight independent Hermitian traceless 3×3 Gell-Mann matrices [18].

The gauge invariant QCD Lagrangian is built by applying the gauge principle to non-Abelian $SU(3)$ group. The gauge principle requires the Lagrangian to be invariant under local SU(3) transformation, $\theta_a = \theta_a(x)$. This is achieved by replacing the derivative of the quark field $\partial_\mu \psi_f$ by its covariant derivative,

$$D_\mu \psi_f = \left(\partial_\mu - ig_s T^a A^a_\mu\right) \psi_f, \tag{1.3}$$

where A^a_μ denotes the gluon field. The gauge invariant QCD Lagrangian is

$$\mathcal{L}_{QCD} = \sum_f \bar{\psi}_f \left(i\gamma^\mu D_\mu - m_f\right) \psi_f - \frac{1}{4} G^a_{\mu\nu} G^{a\mu\nu}. \tag{1.4}$$

The gluon field strength tensor $G^a_{\mu\nu}$ is

$$G^a_{\mu\nu} = \partial_\mu A^a_\nu - \partial_\nu A^a_\mu - g_s f_{abc} A^b_\mu A^c_\nu, \tag{1.5}$$

where f_{abc} are anti-symmetric structure constants of $SU(3)$ group, defined by the commutation relations, $[T^a, T^b] = i f_{abc} T^c$ [18].

QCD theory exhibits a number of remarkable features of quark-gluon dynamics. Like all other renormalizable gauge theories, the coupling constant $\alpha_s = g_s^2/(4\pi)$ is a function of the energy scale Q [19],

$$\alpha_s(Q) = \frac{4\pi}{(11 - \frac{2}{3}N_f)\ln(Q/\Lambda_{\rm QCD})}, \tag{1.6}$$

where $\Lambda_{\rm QCD}$ is the energy scale where the coupling becomes strong as Q^2 is decreased, and N_f is the number of flavor considered in the theory. At short distances or high energies, the effective coupling constant decreases logarithmically; quarks and gluons appear to be weakly coupled. This famous feature is called asymptotic freedom [20]. At large distances or low energies, the effective coupling becomes strong, resulting in the phenomena of color confinement [21]. This leads to the conclusion that quarks cannot be isolated in nature but are found in hadronic bound states – mesons and baryons. All observable particles in our physical world must be colorless or color neutral. Even if we try to separate the quark and anti-quark, they cannot be forced apart. Indeed, it is postulated that at large distance, the phenomenological potential between a pair of quark and anti-quark increases linearly[1]. Beyond some critical distance, the potential energy becomes large enough so that a new quark-anti-quark pair can be created from the vacuum: the original quark-anti-quark pair becomes two pairs.

Another important aspect of QCD is the spontaneous breaking of chiral symmetry [23]. More specifically, we introduce the left-handed and right-handed quarks,

$$\psi_L = \frac{1}{2}(1-\gamma_5)\psi, \quad \psi_R = \frac{1}{2}(1+\gamma_5)\psi. \tag{1.7}$$

where $\gamma_5 = i\gamma^0\gamma^1\gamma^2\gamma^3$. It is straightforward to check that the QCD Lagrangian with massless quarks is invariant under global chiral $SU_L(N_f) \times SU_R(N_f)$ rotation,

$$\psi_L \to \Lambda_L\psi_L = \exp\left(i\frac{\lambda^a}{2}\theta_L^a\right)\psi_L, \quad \psi_R \to \Lambda_R\psi_R = \exp\left(i\frac{\lambda^a}{2}\theta_R^a\right)\psi_R, \tag{1.8}$$

[1] One of the most popular models for the quark-antiquark potential is called Cornell potential [22], $V_{q\bar{q}}(r) = -\frac{a}{r} + br$, where the first term is the Coulomb part of potential, and the second term is linear in distance, which enforces confinement.

where Λ_L (Λ_R) is an element of $SU_L(N_f)$ ($SU_R(N_f)$) group, and $\vec{\theta}_{L,R}$ are arbitrary phases. As far as three massless u, d, s quarks are considered, λ^a are $N_f^2 - 1 = 8$ Hermitian traceless 3×3 Gell-Mann matrices. The conserved currents associated with chiral symmetry are

$$J_L^{\mu a} = \bar{\psi}_L \gamma^\mu \frac{\lambda^a}{2} \psi_L, \quad J_R^{\mu a} = \bar{\psi}_R \gamma^\mu \frac{\lambda^a}{2} \psi_R. \tag{1.9}$$

The invariant charges are $Q_L^a = \int d^3x J_L^{0a}$ and $Q_R^a = \int d^3x J_R^{0a}$. It is equivalent to say that the QCD Lagrangian with massless quarks is invariant under the $SU_V(N_f) \times SU_A(N_f)$ transformation

$$\psi \to \Lambda_V \psi = \exp\left(i \frac{\lambda^a}{2} \theta_V^a\right) \psi, \quad \psi \to \Lambda_A \psi = \exp\left(i \gamma_5 \frac{\lambda^a}{2} \theta_A^a\right) \psi, \tag{1.10}$$

where $\vec{\theta}_{V,A}$ are arbitrary phases. The associated conserved currents are vector current $V^{\mu a}$ and axial-vector current $A^{\mu a}$,

$$J_V^{\mu a} = J_R^{\mu a} + J_L^{\mu a} = \bar{\psi} \gamma^\mu \frac{\lambda^a}{2} \psi, \quad J_A^{\mu a} = J_R^{\mu a} - J_L^{\mu a} = \bar{\psi} \gamma^\mu \gamma_5 \frac{\lambda^a}{2} \psi. \tag{1.11}$$

The conserved charges are $Q_V^a = Q_R^a + Q_L^a$ and $Q_A^a = Q_R^a - Q_L^a$. The key point is that Q_V^a and Q_A^a have different behaviors under parity transformation,

$$Q_V^a \to Q_V^a, \quad Q_A^a \to -Q_A^a. \tag{1.12}$$

If chiral symmetry was respected by the QCD vacuum, then for each positive parity state, there should be a negative parity state with equal energy (mass). However, this parity-doubling pattern is not observed in hadron spectra [8]. The light pseudoscalar ($J^P = 0^-$) mesons (π, K, η) have considerably smaller masses than scalar ($J^P = 0^+$) mesons. This implies that the QCD vaccum (the ground state) is not invariant under axial-vector transformation Λ_A,

$$Q_V^a |0\rangle = 0, \quad Q_A^a |0\rangle \neq 0. \tag{1.13}$$

The chiral $SU_L(N_f) \times SU_R(N_f)$ symmetry of QCD Lagrangian is said to be spontaneously broken down to $SU_V(N_f)$ (The axial-vector symmetry $SU_A(N_f)$ is spontaneously broken). This requires that the scalar product of quark fields $\bar{\psi}\psi$ has a

non-zero vacuum expectation value (as it carries the quantum number of the vacuum),

$$\langle 0|\bar{\psi}\psi|0\rangle = \langle 0|\bar{\psi}_L\psi_R + \bar{\psi}_R\psi_L|0\rangle \neq 0. \tag{1.14}$$

Thus, the quark condensate serves as the order parameter of the spontaneous breaking of chiral symmetry in QCD. This is analogous to Cooper pairs and superconductivity in metals, where the order parameter is the pairing of two electrons with opposite spins $e_\uparrow e_\downarrow$.

From Goldstone's theorem [24], spontaneous breaking of a continuous symmetry generates massless spin-0 particles called Goldstone bosons. In the case of massless $SU(3)$ QCD, the eight axial charges Q_A^a create eight degenerate states from the vacuum, $|\phi^a\rangle = Q_A^a|0\rangle$, giving rise to eight massless pseudoscalar bosons. However, due to the nonzero masses of the light quarks, the chiral symmetry is also broken explicitly, leading to Goldstone bosons (π, K, η) that are not exactly massless. However, the explicit breaking is small and can be treated perturbatively.

It is noted that at extremely high temperatures, chiral symmetry is expected to be restored, while at extremely high baryon density, the system exhibits a different type of symmetry breaking pattern – color superconductivity [25, 26].

1.3 Quark-gluon plasma

The asymptotic freedom of QCD tells us that at sufficiently high energy densities, quarks and gluons will interact with each other very weakly, and the hadronic matter will become a deconfined state of quarks and gluons – quark-gluon plasma. QGP can be achieved either by heating the QCD matter up to high temperature or compressing the system to high density (or equivalently large chemical potential [1]). There are three places where we should expect to find QGP: in the early Universe, at the center of compact stars, and in the initial stage of relativistic heavy ion collisions.

[1] From the definition of single particle phase space distribution $f(x,p) = (2\pi)^3 dN/d^3x d^3p$, the number density is exponentially proportional to the chemical potential $n = \int d^3p/(2\pi)^3 f(x,p) \propto \exp(\mu/T)$ for a relativistic Boltzmann distribution.

It is believed that our Universe originated from the Big Bang, a state of almost infinite energy density, 13.7 billions year ago. During the first few microseconds of its life, the energy density and temperature were so high that quarks and gluons could not be bound to form hadrons. Instead, they were deconfined from hadrons and permeated the entire Universe in a thermalized QGP [27]. Besides, in the core of super-dense stars such as neutron stars and quark stars, the density in the center of the stars is about several to tens times larger than that of normal nuclear matter, there might be the possibility of the existence of deconfined QCD matter.

Relativistic heavy ion collisions provide another possibility to create quark-gluon plasma in the laboratories by compressing and heating the heavy nuclei so much that their individual protons and neutrons will overlap, and a large energy density can be created. Either high temperature or high density matter might be formed by colliding heavy nuclei at high energies. High baryon densities could be achieved when the two colliding nuclei stop each other in the center-of-mass region, which happens in relatively low energy nuclear collisions (about a few to a few tens of GeV per nucleon). On the other hand, when the two colliding nuclei have sufficiently high energies, they will pass through each other, and high temperature and low density could be created in the center-of-mass region behind the receding nuclei.

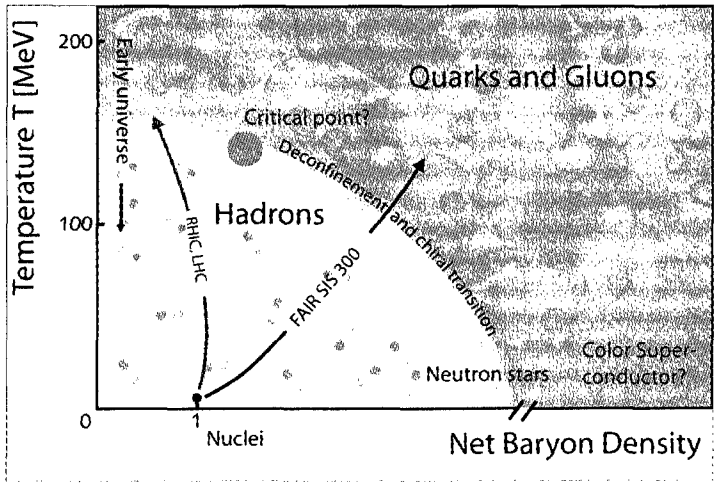

Figure 1.1: A schematic view of the phase diagram of strongly interacting matter. The net baryon density is the density of baryons minus the density of anti-baryons [28].

The study of QGP is not only a key issue for the understanding of quark confinement, but allow us to explore the phase diagrams of the theory of strongly interacting matter: QCD. Clarifying the thermodynamics of QCD is important not only from a fundamental point of view, but may also have an important impact on astrophysics and cosmology [28]. In Fig. 1.1 we show a schematic view of the phase digram of QCD matter in the plane of temperature T and baryon density ρ (or baryon chemical potential μ) [29]. At low temperature and nuclear density, the nuclear matter is in the hadronic phase. As the temperature and nuclear density become sufficiently large, quarks and gluons will deconfined from hadrons and form a quark-gluon plasma phase. Currently, it is not totally clear what are all the possible phases of QCD matter and the precise locations of critical lines and critical points. In fact, the exploration of the detailed structure of QCD phase digram is one of the main objectives in the field of hot and dense QCD.

1.4 The bag model

The MIT bag model [30] is one of the simplest models to incorporate the main features of QCD (color confinement and asymptotic freedom) and examine the possibility of a phase transition between hadronic matter and quark-gluon plasma.

In the bag model, hadrons are considered as bubbles of a QCD vacuum (called bags) in a confining medium. Inside the bag, quarks and gluons interact very weakly and may be considered almost as free particles. To incorporate the properties of color confinement so that no quarks and gluons live outside the bag, a constant energy density B, called the bag constant, is introduced for the vacuum. Assuming the bag is spherical, the total hadron energy is given by

$$E_H = \frac{4\pi}{3} R^3 B + \frac{C_H}{B}, \tag{1.15}$$

where the first term is the potential associated with the finite volume of the bag due to the finite energy density of the vacuum, and the second term C_H/B is the kinetic energy of quarks and gluons inside the bag. By minimizing the energy, we obtain the

size of hadrons

$$\frac{\partial E_H}{\partial R} = 0 \implies R = \left(\frac{C_H}{4\pi B}\right)^{1/4}. \tag{1.16}$$

We may employ the bag model to describe the phase transition between hadronic matter and quark-gluon plasma. As a first approximation, we may assume a gas of free pions in the low temperature limit and a gas of free quarks and gluons in the high temperature limit.

From statistical mechanics, the pressure, energy density and entropy density for a gas of non-interacting massless pions are

$$P_H = d_H \frac{\pi^2}{90} T^4, \ \epsilon_H = 3 d_H \frac{\pi^2}{90} T^4, \ s_H = 4 d_H \frac{\pi^2}{90} T^3, \tag{1.17}$$

where d_H is the hadronic degrees of freedom for N_f flavors of quarks, $d_H = N_f^2 - 1$. The above equations are the equations of state for a massless pion gas, which determines the thermodynamic properties of the pion system.

In the quark-gluon plasma phase, the equations of states read,

$$P_{QGP} = d_{QGP} \frac{\pi^2}{90} T^4 - B, \ \epsilon_{QGP} = 3 d_{QGP} \frac{\pi^2}{90} T^4 + B, \ s_{QGP} = 4 d_{QGP} \frac{\pi^2}{90} T^3, \tag{1.18}$$

where d_{QGP} is an effective degeneracy of the quarks and gluons in the QGP phase,

$$d_{QGP} = \frac{7}{8} d_q + d_g, \ d_q = 2_{q\bar{q}} \times 2_{\text{spin}} \times 3_{\text{color}} \times N_f, \ d_g = 2_{\text{spin}} \times (N_c^2 - 1). \tag{1.19}$$

The factor 7/8 comes from the difference between Fermi-Dirac statistics for quarks and Bose-Einstein statistics for gluons.

Now we are in a position to describe the phase transition in the bag model. The critical temperature T_c is obtained from the phase equilibrium condition,

$$P_H(T_c) = P_{QGP}(T_c) \implies T_c = \left(\frac{90}{\pi^2} \frac{B}{d_{QGP} - d_H}\right)^{1/4}. \tag{1.20}$$

Using the value $B \sim (200 \text{ MeV})^4$, we obtain the critical temperature $T_c \sim 144$ MeV for two flavors $N_f = 2$. The critical energy density required to realize QGP is estimated to be $\epsilon_{\text{crit}} \equiv \epsilon_{QGP}(T_c) \sim 1$ GeV/fm^3. This is the typical behavior of the first order

phase transition, and the energy density ϵ and the entropy density $s = (\epsilon + P)/T$ are discontinuous at $T = T_c$.

Suppose that the equations of state lead to a second-order phase transition, then P and s are continuous, but ds/dT is discontinuous. This may be realized by parameterizing the effective numbers of degrees of freedom in two phases as

$$d_H \to d_H^{\text{eff}} = d_H + be^{(T-T_c)/d}, \quad d_{QGP} \to d_{QGP}^{\text{eff}} = d_{QGP} - ce^{(T-T_c)/d}. \tag{1.21}$$

It is straightforward that as long as $b+c = d_H + d_{QGP}$, $b > 0$, $b \neq (d_H + d_{QGP})/2$, the above parametrizations lead to a second-order phase transition. Besides, the scenario of a smooth crossover from QGP phase to hadronic phase may be produced by the following parametrizations

$$d_H, d_{QGP} \to d^{\text{eff}} = \frac{1}{2}(d_{QGP} + d_H) + (d_{QGP} - d_H)\tanh\left(\frac{T - T_c}{d}\right). \tag{1.22}$$

In the above parametrizations of equations of state, we have completely neglected the effect of the interaction among particles. Such interactions must be taken into account in order to have a full understanding of the physics related to the phase transition between hadronic matter and quark-gluon plasma. At extremely low temperature, chiral perturbation theory [31, 32, 33, 34, 35] may be used to study the interaction between pions. Due to asymptotic freedom, at extremely high temperature, perturbative QCD is a suitable tool to calculate the interaction between quarks and gluons. To study the physics near the critical points, we have to resort to non-perturbative approaches, such as lattice QCD simulations [11, 12, 13], and renormalization group methods [36, 37] .

1.5 The evolution of a relativistic heavy ion collision

The space-time history of a relativistic heavy ion collision begins from the colliding of two Lorentz-contracted nuclei. Then two nuclei cross each other and recede from each other at high velocity in the opposite direction from the interaction region. A large amount of lost energy by the two nuclei will be deposited in the center-of-mass region,

producing very excited nuclear matter. In Fig. 1.2, we show a schematic view of the entire history of a relativistic heavy ion collision with a space-time diagram [38]. Since the excited strongly-interacting system moves with relativistic velocity, the evolution of the system is characterized by the proper time in its rest frame $\tau = \sqrt{t^2 - z^2}$. Each hyperbola in the diagram has a constant proper time.

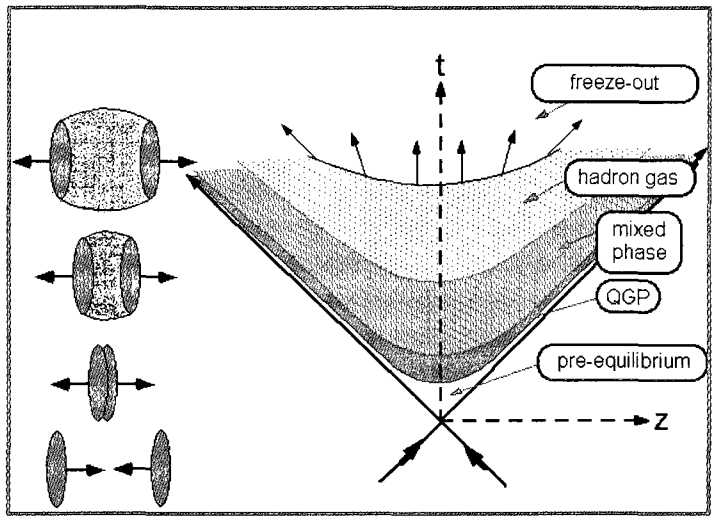

Figure 1.2: A schematic view of the space-time evolution of the system produced in a heavy ion collision [37].

1.5.1 Pre-equilibrium

The very early stage of relativistic heavy ion collisions is a highly non-equilibrium process in which large entropy is produced. Theoretically, entropy production in these processes is one of the most difficult questions to answer since it involves non-Abelian gauge field theory. Many theoretical models have been proposed to understand the entropy production process, such as mini-jets from the incoherent sum of incoming partons followed by the equilibration process [39, 40, 41, 42], and a coherent classical configuration of low-x gluon associated with incoming nuclei to form the color glass condensate (CGC) [43].

In the present study, we simply assume that the entropy production and subsequent local thermalization take place before certain proper time $\tau = \tau_i$. Then the evolution

of the created system in the collisions after that time will be controlled by relativistic hydrodynamics [44, 45, 46]). It has already been shown that the collective behavior of soft particle production at RHIC may be well described by assuming a perfect fluid for the created matter [47, 48, 49, 50, 51, 52], with a thermal equilibrium time τ_i of the system less than 1 fm/c.

1.5.2 Hydrodynamical evolution

In this period, the evolution of the quark-gluon plasma and its transition to the hadronic phase take place. Suppose local thermal equilibrium is achieved at a certain stage of the collisions, $\tau = \tau_i$, then we may study the evolution of the system using relativistic hydrodynamics as long as the mean free path of constituent particles is much smaller than the typical length scale of the system.

For a system in local thermal equilibrium, its energy momentum tensor and baryon number density may be parameterized only by the local energy density ϵ and pressure P. Assuming the system can be approximated by a perfect fluid (without viscosity and thermal conductivity), the energy-momentum tensor is given by,

$$T^{\mu\nu}(x) = (\epsilon(x) - P(x))u^{\mu}(x)u^{\nu}(x) - P(x)g^{\mu\nu}, \tag{1.23}$$

where $x^{\mu} = (t, \vec{x})$. $\epsilon(x)$ is the local energy density, $P(x)$ is the local pressure, and $u^{\mu}(x) = \gamma(x)(1, \vec{v}(x))$ is the four velocity of the fluid with respect to some fixed reference frame. It is straightforward to check that in the local frame of the fluid, $u^{\mu} = (1, 0, 0, 0)$, the energy-momentum tensor is diagonal, $T^{00} = \epsilon$, $T^{ij}(x) = P(x)\delta_{ij}$ and $T^{i0}(x) = T^{0i}(x) = 0$. In general, the trace of the energy momentum tensor is $T^{\mu}_{\mu}(x) = \epsilon(x) - 3P(x)$. For a non-interacting gas of massless particles, $P(x) = \epsilon(x)/3$, the trace vanishes.

The dynamics of the fluid is described by equations of motion based on the conservation of the local energy and momentum, which can be expressed as

$$\partial_{\mu} T^{\mu\nu}(x) = 0. \tag{1.24}$$

If there are conserved charges, such as baryon number or electric charge, there is an additional conservation law for each. For example, the baryon number $j^{\mu}_{B}(x)$ is given

by

$$j_B^\mu(x) = n_B(x)u^\mu(x), \tag{1.25}$$

where $n_B(x) = j_B^0(x)$ is the baryon number density measured in the local frame of the fluid. The corresponding conservation law is

$$\partial_\mu j_B^\mu(x) = 0. \tag{1.26}$$

The above conservation laws contain five independent scalar equations, and are supplemented by equation of state, $\epsilon = \epsilon(P)$. The local energy density, pressure and baryon density may be expressed in terms of the temperature and chemical potential as a function of space and time. By solving these six equations, the space-time evolution of six thermodynamic variables, $\epsilon(x)$, $P(x)$, $n_B(x)$ and three components of the flow vector, $v_x(x)$, $v_y(x)$ and $v_z(x)$ can be determined. In general, the above equation cannot be solved analytically and we have to resort to numerical methods unless some simplified assumptions are placed on the symmetry of the system. Given certain initial conditions at $\tau = \tau_i$, the hydrodynamical equations can predict the subsequent development of the system until it undergoes freeze-out at $\tau = \tau_f$.

1.5.3 *Post-freeze-out*

The freeze-out of the hadronic matter happens at $\tau = \tau_f$, when the constituents of the system begin free-streaming towards the detectors. The freeze-out is defined by the space-time hyper-surface Σ_f, where the mean free paths λ of the plasma particles are compatible to the spatial dimensions of the system R (or the time scale of the system expansion),

$$\lambda \sim \frac{1}{n\sigma} \sim R. \tag{1.27}$$

We may define the freeze-out temperature T_f for each particle species, and as the temperature of a volume of the fluid is equal to the freeze-out temperature T_f, the freeze-out process happens for this particle species. The particle spectrum at freeze-out (the number of particle passing through the freeze-out hyper-surface) is computed

from the Cooper-Frye formula [53],

$$E\frac{dN}{d^3p} = \int_{\Sigma_f} \frac{g}{(2\pi)^3} d\sigma_\mu p^\mu f(x,p) = \int_{\Sigma_f} \frac{g}{(2\pi)^3} d\sigma_\mu p^\mu \frac{1}{\exp[(p_\nu u^\nu - \mu_f)/T_f] \pm 1} \quad (1.28)$$

where $d\sigma_\mu$ is the normal vector to this hyper-surface, p^μ is the particle momentum, f is the single particle phase space distribution function, and μ_f is chemical potential at freeze-out.

There are two types of freeze-out: chemical freeze-out and thermal freeze-out. Chemical freeze-out means the number of each particle species is frozen and no longer changes. Thermal freeze-out is achieved as the kinetic equilibrium is no longer maintained for the system. Since the inelastic interactions have energy thresholds, whereas elastic interactions do not, the chemical freeze-out temperature must be higher than that of the thermal freeze-out.

It is noted that even after freeze-out, hadrons can still interact with each other in a non-equilibrium way which may be described by the Boltzmann equation at the hadronic level. The particle spectra at freezeout can serve as the initial conditions for the microscopic transport models, such as hadronic cascade [54, 55, 56], Ultra-relativistic Quantum Molecular Dynamics (UrQMD) [57, 58], etc.

1.6 The Glauber model

The basic idea of the Glauber model [59, 60, 61, 62] is to describe the nucleus-nucleus collisions as a collection of independent individual nucleon-nucleon collisions. The space distribution of the nucleons is determined from experimental measurements of nuclear density distributions, i.e., low-energy electron-nucleus scattering. Consequently, the collisions of the two heavy nuclei can be treated as the uncorrelated individual interactions of the constituent nucleons. Another assumption in the model is that the individual nucleons carry so high energies that their linear trajectories are maintained as the nuclei pass through each other. This hypothesis make is possible to derive simple analytical expressions for nucleus-nucleus cross sections in terms of fundamental nucleon-nucleon cross sections. The nuclear density distribution and

inelastic nucleon-nucleon cross section are two important experimental inputs when a Glauber approach is employed to calculate the geometry of the nuclear collisions.

The nucleon density function is usually parameterized by a Fermi distribution,

$$\rho(r) = \frac{\rho_0}{1 + e^{(r-R)/d}} \left[1 + w\left(r\right)\right], \tag{1.29}$$

where ρ_0 corresponds to the nucleon density in the center of the nucleus, R represents the average nuclear radius, d is the surface diffuseness and w characterizes deviations from a spherical shape. The distribution for a spherical shape with $w = 0$ is often called Woods-Saxon distribution. The integral of the nuclear density function over all space gives the atomic number of the nuclei, $\int d^3r\rho(r) = A$. Those parameters are determined by low-energy electron-nucleus scattering [63], i.e., $R = 6.38$ fm, $a = 0.535$ fm and $w = 0$ for ^{197}Au, and $R = 4.20641$ fm, $a = 0.5977$ fm and $w = 0$ for ^{63}Cu.

Another input of the model is the inelastic nucleon-nucleon cross section. Since low momentum transfer processes are involved in the collisions, it is impossible to calculate it from perturbative QCD. Experimental results have shown that the inelastic nucleon-nucleon cross section is an increasing function of the beam-energy [8]. For nucleon-nucleon collisions at $\sqrt{s_{NN}} = 200$ GeV at RHIC, the inelastic cross section $\sigma_{NN} \sim 42$ mb.

Now we consider two nuclei, target "A" and projectile "B", colliding with each other with relativistic energies at impact parameter b, as shown in Fig. 1.3. The probability for a nucleon being located in the unit transverse area in one of the nuclei is called the thickness function

$$T_A(\vec{r}_\perp) = \int dz \rho_A(\vec{r}_\perp, z). \tag{1.30}$$

The overlap function of two colliding nuclei is defined by

$$T_{AB}(\vec{b}) = \int d^2\vec{r}_\perp T_A(\vec{r}_\perp + \vec{b}/2) T_B(\vec{r}_\perp - \vec{b}/2), \tag{1.31}$$

which represents the effective overlap area for which a specific nucleon in "A" can interact with a given nucleon in "B". Then it is straightforward to obtain the total

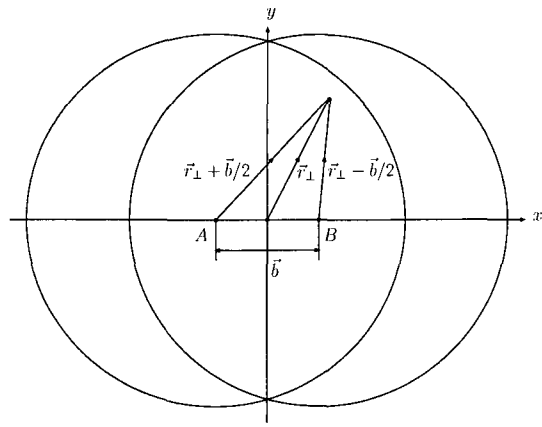

Figure 1.3: The interaction zone of the collisions between two identical nuclei with impact parameter b viewed in the transverse plane.

number of elementary nucleon-nucleon collisions at impact parameter b, called the number of binary collisions

$$N_{\rm coll}(b) = T_{AB}(b)\sigma_{NN}. \tag{1.32}$$

Since the total possible number of nucleon-nucleon collisions in a A+B collision is AB, the probability of having one such collision will be $N_{\rm coll}/(AB)$. Therefore, the probability of having n such collisions between "A" and "B" is given by a binomial distribution,

$$P(n,\vec{b}) = C_{AB}^{n}\left(\frac{T_{AB}\sigma_{NN}}{AB}\right)^{n}\left(1-\frac{T_{AB}\sigma_{NN}}{AB}\right)^{AB-n}. \tag{1.33}$$

The differential cross section between the collisions between "A" and "B" is then given by

$$\frac{d^2\sigma_{AB}}{d^2\vec{b}} = \sum_{n=1}^{AB} P(n,\vec{b}) = 1-\left(1-\frac{T_{AB}\sigma_{NN}}{AB}\right)^{AB}. \tag{1.34}$$

The number of participants ("wounded nucleons") in such a collision at impact parameter b is given by [62]

$$N_{\rm part}(b) = \int d^2\vec{r}_\perp T_A(\vec{r}_\perp + \vec{b}/2)\left[1-\left(1-\frac{T_B(\vec{r}_\perp - \vec{b}/2)\sigma_{NN}}{B}\right)^{B}\right]$$

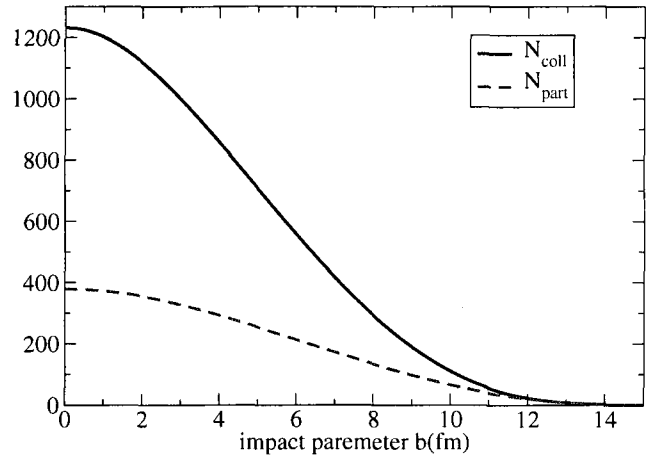

Figure 1.4: Numbers of binary collisions $N_{\rm coll}$ and wounded nucleon $N_{\rm part}$ as a function of impact parameter in Au+Au collisions at $\sqrt{s_{NN}} = 200$ GeV.

$$+\int d^2\vec{r}_\perp T_B(\vec{r}_\perp - \vec{b}/2)\left[1-\left(1-\frac{T_A(\vec{r}_\perp-\vec{b}/2)\sigma_{NN}}{A}\right)^A\right]. \qquad (1.35)$$

In Fig. 1.4, the binary collision number $N_{\rm coll}$ and the participant number $N_{\rm part}$ are shown as a function of impact parameter b for Au+Au collisions at $\sqrt{s_{NN}} = 200$ GeV at RHIC, where $d = 0.535$ fm, $R = 6.38$ fm and $\sigma_{NN} = 42$ mb are used in the Woods-Saxon distribution.

Often, the *centrality* $x\%$ as a function of impact parameter b is defined,

$$x\%(b) = \frac{\int_0^b d^2\vec{b}\; d\sigma_{AB}/d^2\vec{b}}{\int_0^\infty d^2\vec{b}\; d\sigma_{AB}/d^2\vec{b}}. \qquad (1.36)$$

Then a centrality class $x-y\%$ may be used to represent all the collisions with an impact parameter $b(x) < b < b(y)$. The average number of binary collisions in a centrality class $x-y\%$ is calculated by

$$\langle N_{\rm coll}\rangle = \frac{\int_{b(x)}^{b(y)} d^2\vec{b}\; N_{\rm coll}(b)}{\int_{b(x)}^{b(y)} d^2\vec{b}\; d\sigma_{AB}/d^2\vec{b}}. \qquad (1.37)$$

In Fig. 1.5, the centrality $x\%$ and the differential cross section $d\sigma_{AB}$ are shown as a function of impact parameter b for Au+Au collisions at $\sqrt{s_{NN}} = 200$ GeV at RHIC.

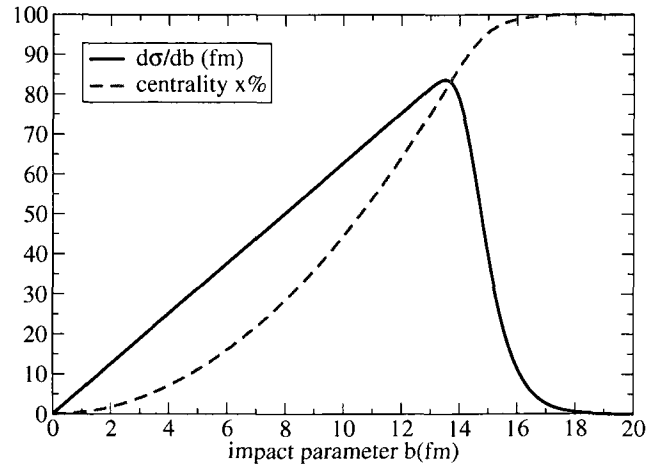

Figure 1.5: The differential cross section $d\sigma_{AB}/db$ and the centrality $x\%$ as a function of impact parameters in Au+Au collisions at $\sqrt{s_{NN}} = 200$ GeV.

1.7 The Bjorken model

The Bjorken model [44] is one of the simplest models to describe the evolution of the system created in heavy ion collisions provided that the local thermal equilibrium is assumed to be achieved at $\tau = \tau_i$. A lot of intuitive information about the evolution of the excited matter created in relativistic heavy ion collisions may be extracted from this approach. The motivation of the Bjorken model came from the experimental data which indicated that the charged particle multiplicities are approximately independent of the rapidity in the central rapidity region, i.e., they are invariant under Lorentz boosts of moderate rapidity [64, 65, 66]. Since the reaction region in the collisions has strong expansion along the longitudinal beam direction, it is reasonable to first approximation to drop the transverse spatial dimension (x, y) and describe the central rapidity region of the system in $(1+1)$ dimensions, z and t. Now we transform the coordinate system to the longitudinal proper time τ and the space-time rapidity η,

$$\tau = \sqrt{t^2 - z^2}, \quad \eta = \frac{1}{2} \ln \frac{t+z}{t-z}. \tag{1.38}$$

The inverse transformation reads,

$$t = \tau \cosh \eta, \quad z = \tau \sinh \eta. \tag{1.39}$$

The flow four velocity of the fluid is dependent on τ and η,

$$u^\mu = \frac{dx^\mu}{d\tau} = (\cosh\eta, 0, 0, \sinh\eta). \tag{1.40}$$

It is straightforward to check $u^\mu u_\mu = 1$. Another approximation in the Bjorken model is that the baryon number is set to be zero in the central rapidity region, $n_B = 0$. In the collision of two heavy nuclei with relativistic energies, the baryon number is supposed to be carried away essentially by the nucleons leaving the interaction region. Therefore, we only need to solve the equation for the conservation of energy and momentum

$$\begin{aligned}\partial_\mu T^{\mu\nu} =& \frac{\partial}{\partial x^\mu}[(\epsilon + P)u^\mu u^\nu - P g^{\mu\nu}] \\ =& \frac{\partial(\epsilon + P)}{\partial\tau}\frac{\partial\tau}{\partial x^\mu}u^\mu u_\nu + (\epsilon + P)\frac{\partial u^\mu}{\partial x^\mu}u^\nu + (\epsilon + P)u^\mu\frac{\partial u^\nu}{\partial x^\mu} - g^{\mu\nu}\frac{\partial P}{\partial\tau}\frac{\partial\tau}{\partial x^\mu} \\ =& 0.\end{aligned} \tag{1.41}$$

The above equation can be simplified by using the following relations:

$$\frac{\partial\tau}{\partial x^\mu} = u_\mu, \quad \frac{\partial u^\mu}{\partial x^\mu} = \frac{1}{\tau}, \quad u^\mu\frac{\partial}{\partial x^\mu} = \frac{\partial}{\partial\tau}. \tag{1.42}$$

Note that $\frac{\partial u^\mu}{\partial\tau} = 0$ from Eq. (1.40), then we obtain the evolution equation of the system,

$$\frac{\partial\epsilon}{\partial\tau} + \frac{\epsilon + P}{\tau} = 0. \tag{1.43}$$

From the thermodynamic relation $s = (\epsilon + P)/T$, and $ds = d\epsilon/T$ at constant volume, we have,

$$\frac{\partial s}{\partial\tau} + \frac{s}{\tau} = 0. \tag{1.44}$$

The solution of the above equation is

$$s(\tau)\tau = s(\tau_i)\tau_i = \text{const}, \tag{1.45}$$

where τ_i is the initial proper time. As the volume element dV is given by $d^2r_\perp\tau d\eta$, the above relation implies that

$$\frac{dS}{d^2r_\perp d\eta} = s\tau = \text{const}. \tag{1.46}$$

As transverse expansion is excluded for consideration in the model, we obtain

$$\frac{d}{d\tau}\left(\frac{dS}{d\eta}\right) = 0. \tag{1.47}$$

Thus, the hydrodynamical motion of the fluid in the Bjorken model is characterized by the constant entropy per unit rapidity with respect to the proper time.

To further describe the evolution of the system, we have to specify the equation of state for the system. Here, we assume a first order transition between the QGP phase and the hadronic phase. Above the critical temperature, the system is described by the bag model with massless quarks and gluons, with the equation of state given by $P = \epsilon/3$. Then the evolution equations for the energy density and pressure of the system are

$$\frac{d\epsilon}{d\tau} + \frac{4}{3}\frac{\epsilon}{\tau} = 0, \quad \frac{dP}{d\tau} + \frac{4}{3}\frac{P}{\tau} = 0, \tag{1.48}$$

which have the solutions

$$\epsilon(\tau)\tau^{4/3} = \epsilon(\tau_i)\tau_i^{4/3}, \quad P(\tau)\tau^{4/3} = P(\tau_i)\tau_i^{4/3}. \tag{1.49}$$

From the equation of state, we may get the evolution of the temperature as a function of the proper time,

$$T(\tau) = T(\tau_i)\left(\frac{\tau_i}{\tau}\right)^{1/3}. \tag{1.50}$$

As for a first-order phase transition from quark-gluon plasma to the hadronic phase, the temperature of the plasma drops down to T_c at the proper time determined by

$$\tau_c = \left(\frac{T(\tau_i)}{T_c}\right)^3 \tau_i. \tag{1.51}$$

After this proper time, the system enters a mixed phase of quark-gluon plasma and hadronic matter. The entropy density of the matter is given by

$$s(\tau) = f_{QGP}(\tau)s_{QGP}(T_c) + [1 - f_{QGP}(\tau)]\, s_H(T_c), \tag{1.52}$$

where $f_{QGP}(\tau)$ is the fraction of matter in the QGP phase. By employing the relation $s(\tau)\tau = s(\tau_c)\tau_c = s(\tau_h)\tau_h$, we may derive the evolution of $f_{QGP}(\tau)$ as a function of

the proper time,

$$f_{QGP}(\tau) = \frac{1}{r-1}\left(r\frac{\tau_c}{\tau} - 1\right), \tag{1.53}$$

where $r = d_{QGP}/d_H$ is the ratio of the numbers of degrees of freedom between two phases. The entropy density drops to $s_H(T_c)$ at $\tau_h = r\tau_c$, when all the quark-gluon plasma matter are converted into hadronic matter, $f_{QGP}(\tau_h) = 0$.

In the case that the system starts from the mixed phase at τ_i, with QGP fraction $f_{QGP}(\tau_i)$, we have the general expression for the QGP fraction $f_{QGP}(\tau)$,

$$[(r-1)f_{QGP}(\tau) + 1]\,\tau = [(r-1)f_{QGP}(\tau_i) + 1)]\,\tau_i. \tag{1.54}$$

Then the system arrives at hadronic phase at τ_h given by

$$\tau_h = [(r-1)f_{QGP}(\tau_i) + 1]\,\tau_i. \tag{1.55}$$

After this proper time, the system will be in the hadronic phase. The dynamics of hadronic system can still be described by relativistic hydrodynamics, with the appropriate hadron equation of state. The temperature of the hadronic matter will decrease until it reaches the freeze-out temperature at τ_f.

Now we relate the initial conditions, i.e., entropy density $s(\tau_i)$ and energy density $\epsilon(\tau_i)$, to the experimental observables such as the emitted particle per unit rapidity $dN/d\eta$ and transverse energy per unit rapidity $d\langle E_T\rangle/d\eta$. Since the volume element on the freeze-out hypersurface at τ_f is $\pi R^2\tau_f d\eta$ in a (1+1)-dimensional expansion, the rapidity distribution of emitted particles is given by

$$\frac{dN}{d\eta} = \pi R^2 \tau_f n(\tau_f), \tag{1.56}$$

where $n(\tau_f)$ is the number density of constituent particles. As the baryon number vanishes in the central region, the entropy is mostly carried by pions. From the relation between entropy density and particle number density is

$$s = \frac{2\pi^4}{45\zeta(3)}n = \lambda n \approx 3.6n. \tag{1.57}$$

we obtain the relation between initial entropy density and rapidity distribution of particles, by using the relation $s(\tau)\tau = s(\tau_i)\tau_i$ during the expansion,

$$s(\tau_i) = \lambda \frac{1}{\pi R^2 \tau_i} \frac{dN}{d\eta} = \frac{2\pi^4}{45\zeta(3)} \frac{1}{\pi R^2 \tau_i} \frac{dN}{d\eta}. \tag{1.58}$$

From Eq. (1.18), it is straightforward to write down the relation between the initial proper time τ_i and temperature $T(\tau_i)$ to the particle rapidity distribution [67],

$$T^3(\tau_i)\tau_i = \frac{\pi^2}{d_{QGP}\zeta(3)} \frac{1}{\pi R^2} \frac{dN}{d\eta}. \tag{1.59}$$

Similar to $dN/d\eta$, the total energy produced per unit rapidity is given by

$$\frac{d\langle E\rangle}{d\eta} = \pi R^2 \tau_f \epsilon(\tau_f). \tag{1.60}$$

Again, by using the relation $\epsilon(\tau)\tau^{4/3} = \epsilon(\tau_i)\tau_i^{4/3}$ during the expansion, we find

$$\epsilon(\tau_i) = \frac{1}{\pi R^2 \tau_i} \left.\frac{d\langle E_T\rangle}{d\eta}\right|_{\eta=0} \left(\frac{\tau_f}{\tau_i}\right)^{1/3} = \frac{\langle E_T\rangle}{\pi R^2 \tau_i} \left.\frac{dN}{d\eta}\right|_{\eta=0} \left(\frac{\tau_f}{\tau_i}\right)^{1/3}, \tag{1.61}$$

where we have used $\langle E_T\rangle = \langle E\rangle$ at $\eta = 0$. In the case of free streaming, by setting $\tau_f = \tau_i$, we may reproduce the famous Bjorken formula [44]. Thus, the factor $(\tau_f/\tau_i)^{1/3}$ is a measure of the energy transfer due to the work done by the pressure during the hydrodynamical expansion.

Another way to estimate the energy density is to apply the equation of state,

$$\epsilon = \frac{3}{4} sT = \frac{3}{4} \lambda n T. \tag{1.62}$$

Then, the initial energy density may be related to the rapidity distribution as

$$\epsilon(\tau_i) = \frac{3}{4} \left(\frac{45}{2\pi^2 d_{QGP}}\right)^{1/3} \left(\frac{1}{\pi R^2 \tau_i} \frac{dN}{d\eta}\right)^{4/3}. \tag{1.63}$$

It should be noted that hydrodynamics itself cannot tell the initial conditions, i.e., the initial time τ_i, the spatial profiles of the energy density, and the baryon chemical potential at τ_i. The initial conditions are usually adjusted to fit the final experimental observables. A more fundamental approach would be to calculate the initial conditions from microscopic theories. If we assume the thermallization of quarks and gluons

immediately happens upon their production [68], we may obtain a rough estimation of the initial conditions by employing the uncertainty principle of quantum mechanics at that time, $\langle E(\tau_i)\rangle\tau_i \approx 1$, where $\langle E(\tau_i)\rangle$ is the average energy of partons at proper time τ_i. For simplicity, here we neglected the effects of Bose or Fermi statistics, then Eq. (1.59) becomes,

$$T^3(\tau_i)\tau_i = \frac{\pi^2}{d_{QGP}} \frac{1}{\pi R^2} \frac{dN}{d\eta}, \tag{1.64}$$

where $d_{QGP} = 12N_f+16$. Furthermore, the average particle energy is about $\langle E\rangle \approx 3T$, then we obtain,

$$T(\tau_i)\tau_i = \frac{1}{3}. \tag{1.65}$$

Putting together, we obtain the temperature at initial thermalization time τ_i,

$$T(\tau_i) = \left(\frac{3\pi^2}{d_{QGP}} \frac{dN/d\eta}{\pi R^2}\right)^{1/2}. \tag{1.66}$$

For central Au+Au collisional at $\sqrt{s_{NN}} = 200$ GeV at RHIC, we take $dN_{ch}/d\eta|_{\eta=0} \approx 700$ based on the charged particle pseudorapidity densitity measured by the PHOBOS experiment [69]. Thus for three flavors $N_f = 3$, the initial conditions are estimated to be $\tau_i \approx 0.17$ fm/c and $T(\tau_i) \approx 400$ MeV.

1.8 Signatures of QGP in relativistic heavy ion collisions

Relativistic heavy ion collisions are designed to create and study a new state of QCD matter – quark-gluon plasma and investigate the critical phenomena related to its phase transition to the confined hadronic matter. One of the most important tasks in relativistic heavy ion collisions is to find clear and unambiguous signatures for observing the formation of quark-gluon plasma and studying its properties. This turns out to be complicated. The deconfined degrees of freedom (quarks and gluons) are not directly observable. If a QGP is produced in a collision it will quickly cool down, expand and hadronize into a plethora of mesons and baryons, which fly off to the detectors. The QGP created in the collisions has very small size and lifetime,

at most a few fermis and perhaps $5 - 10$ fm/c in duration. In order to observe the QGP formation in the collisions, we have to resort to a variety of indirect probes by looking at the particles that stream out from the collisions. Moreover, signals of the quark-gluon plasma compete with many backgrounds from the hot hadronic matter and are modified by final-state interactions in the hadronic phase.

In spite of this, a wealth of ideas has been proposed in the past few decades to identify and investigate the short-lived quark-gluon plasma phase, such as strangeness enhancement [70, 71], heavy quarkonium suppression [72], electromagnetic radiation [73, 74, 75], correlations and fluctuations [76, 77, 78], high p_T jet quenching [79, 80], etc. The basic idea is that a collision that produces QGP will send out different signals than a collision that does not produce QGP. A comprehensive survey of the quark-gluon plasma signatures is beyond the scope of this thesis, and I will concentrate on two very important and promising ones: electromagnetic radiation and high transverse momentum jets.

1.8.1 *Electromagnetic radiation in relativistic heavy ion collisions*

Real photons and lepton pairs (virtual photons) have been proposed as one of the most promising probes of quark-gluon plasma, and are currently under active investigations. As they carry no color charge, these particles will interact only electromagnetically with the surrounding matter. As the coupling constant α_e for the electromagnetic interaction is much smaller than the coupling constant α_s for strong interaction ($\alpha_e \sim 1/137$ and $\alpha_s \sim 1/3$ for QGP at temperature $T \sim 300$ MeV), the mean free path of the photon is much larger than the typical size of a QGP. As a result, once they are produced, photons will leave the medium immediately and fly off to the detectors without further rescattering, thus carrying information about the interior of the quark-gluon plasma during the earliest and hottest phase of the evolution of the fireball. Another advantage of small α_e is that it allows the application of perturbation theory to calculate photon production rates from QGP.

However, this ideal scenario is complicated by the fact that photons and dileptons may be produced from various sources. During the early stage of the collisions,

photons may be produced either from initial hard collisions between the two nuclei by Compton and annihilation processes, or by pre-equilibrium interactions. If a thermalized QGP is created in a collision, the collisions among the medium partons, such as annihilation processes and Compton scattering may create thermal photons. Photons may also come from hard jets, either through direct jet-medium interaction during their passage, i.e., the photon bremsstrahlung and $2 \rightarrow 2$ jet-photon conversion processes, or through fragmentation after their passing through the QGP. In the subsequent hadronic phase, photons may be produced by inelastic collisions of hadrons, like $\pi + \rho \rightarrow \pi + \gamma$ and $\pi + N \rightarrow N + \gamma$. Finally, the decay of neutral hadrons, such as π^0 and η, may produce photons. Thus we have to take into account all the contributions from both QGP sources and non-QGP sources in order to have a comprehensive understanding of the physics of the photon production in relativistic heavy ion collisions. In Chapter 2 [81, 82], we will present a new channel of photon production which arises solely when the charge symmetry in hot and dense QCD matter is explicitly broken.

1.8.2 *High p_T jets as probes of QGP*

Large transverse momentum (p_T) jets of partons are regarded as good tools to probe the color structure of hot and dense QCD matter in relativistic heavy ion collisions. They are produced in the early state of the collisions and therefore have the capability to probe all the stages of system by interacting directly with the hot and dense medium during their path. At this point, hard jets stand in an excellent position to make a bridge between the experimental data and the theoretical understanding of the medium properties.

Experimental results at RHIC have shown that high p_T hadrons in central A+A collisions are significantly suppressed in comparison with those in binary scaled p+p collisions [83, 84, 61]. Moreover, the disappearance of back-to-back azimuthal correlations have been observed in central A+A collisions, in contrast to the strong back-to-back correlations in p+p and peripheral A+A collisions [85]. Those results have been attributed to the strong interaction between hard partonic jets produced

in the early stage of the collisions and the hot and dense nuclear medium created in those collisions, and are commonly referred to as jet-quenching [86].

A lot of effort has gone into quantitatively calculating jet-quenching processes taking place inside the soft matter. Gluon bremsstrahlung have been proposed to be one of the dominant mechanisms for the energy loss of jets when traversing through the medium. In a thermal medium, it has been shown that the coherence effect called Landau-Pomeranchuk-Migdal (LPM) [87] effect controls the strength of the induced bremsstrahlung gluon emission. Several theoretical formalisms have been elaborated to describe the energy loss by the gluon bremsstrahlung: here we mention the work by Baier-Dokshitzer-Mueller-Peigne-Schiff (BDMPS) [88], Gyulassy-Levai-Vitev (GLV) [89], Kovner-Wiedemann (KW) [90], Zakharov [91], Majumder-Wang-Wang (Higher Twist) [92], and Arnold-Moore-Yaffe (AMY) [93, 94, 95]. Another important energy loss mechanism experienced by the color charges in the medium is by scattering off the thermal partons from the nuclear medium through $2 \rightarrow 2$ elastic collisions. The collisional energy loss of jets has also been extensively studied in several different approaches and scenarios [96, 97, 98, 99, 100, 101, 102, 103]. The first consistent study of radiative and collisional energy loss in the same energy loss formalism (AMY [93, 94, 95]) was carried out in [104, 105] and is described in this thesis (see Chapter 5 for details).

All these studies have given rise to the hope that jets may be seen as a "tomographic tool" to study the hot and dense core of the early evolution of the nuclear medium in some detail. Several quantities have been suggested as such "tomographic tools". One of those is the nuclear modification factor R_{AA}, defined as the ratio of the hadron yield in A+A collisions to that in p+p interactions scaled by the number of binary collisions. Since R_{AA} is a rather averaged quantity (over jets' origin and in-medium path length), it cannot provide us much of detailed information about the hot matter created in collisions. More detailed information about the medium properties may be obtained by studying R_{AA} as a function of azimuth and p_T in non-central collisions [106] (see Chapter 4). This effectively corresponds to studying

different paths of partons as they traverse the expanding medium. The nuclear modification factor R_{AA} could also be studied as a function of p_T at central and non-central collisions at mid and forward rapidity [106] (see Chapter 4).

We may also perform correlation measurements, i.e., to study the production of high p_T hadrons correlated with other high p_T particles that are produced at the initial vertex. One possibility is to use a hadron as the trigger particle, but the energy of the away-side parton is not confined even though we choose a specific p_T for the triggered hadron. Another promising suggested trigger is a high p_T photon [107, 108]. At leading order, the photons are predominantly produced from hard collisions in the early stage. If we trigger such a photon at mid-rapidity, the energy of away-side associated jet will be determined. However, it should be noted that high p_T photons can be produced from other processes in high energy nuclear collisions, such as those involving the jet-plasma interactions during their propagation in the medium and fragmentation of surviving jets after their passing through the medium. We will see in Chapter 6 [109] that it is important to take into account these additional processes for a comprehensive study of photon-hadron correlations.

2

Photon production from charge-asymmetric hot and dense matter

This chapter follows our recent work [81, 82], where a new channel of direct photon production from a quark-gluon plasma is explored in the framework of high temperature QCD. This process appears in the next-to-leading-order in the presence of a charge asymmetry in the excited QCD matter, and may be effectively described as the bremsstrahlung of a real photon from a thermal gluon. It is found that the photon production rate from this new channel is suppressed compared to the QCD annihilation and Compton scattering at low baryon density, but could become important in baryon-rich matter.

2.1 Introduction

As have been mentioned earlier, photons (real and virtual) occupy a privileged status in theoretical studies of hot and dense strongly interacting systems as they suffer essentially no final state interaction after their initial production [110]. Thus, their emission rates have the potential to provide direct insight into the nature of the medium created at RHIC.

In this chapter, we will explore the electromagnetic signatures from a series of pure glue processes, which arise when the hot and dense medium is itself electrically charged. This is achieved by the introduction of a non-vanishing charge chemical potential or a net asymmetry between the quark and anti-quark populations. The possibility of such rates was first pointed out in Ref. [111], and the dilepton rates from such processes in different scenarios was explored in Ref. [112]. Here, we will focus on the spectra of real photons from such processes.

There have been a large number of calculations of photon production from an electrically charged QGP [75, 93, 94, 95, 113, 114]. However, all these calculations have neglected the baryon chemical potential μ_B in the plasma. As is known, the central region at the CERN SPS and even at RHIC is not just heated vacuum [115, 116, 117], but actually displays an asymmetry between baryon and anti-baryon populations, thus μ_B in the QGP does not vanish. In Ref. [118, 119, 120, 121], the photon production rate was calculated for finite baryon chemical potential, but they only include processes which are non-vanishing at $\mu_B = 0$. Here, we extend those efforts and present the first attempt to calculate hard photon production rates from processes which arise solely at finite chemical potential.

2.2 The photon-gluon-gluon vertex

In Quantum Electrodynamics (QED), diagrams that contain a fermion loop with an odd number of photon vertices (see Fig. 2.1) vanish at zero temperature, and at finite temperature and zero charge density, due to the cancellation by an equal and opposite contribution originating from the same diagram with fermion lines running in the opposite direction (Furry's theorem [122, 123]).

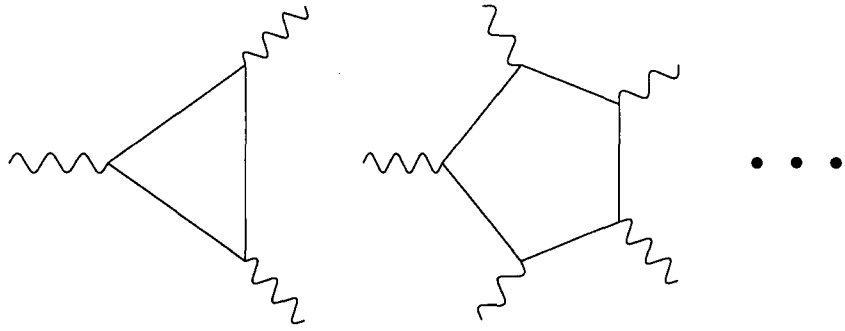

Figure 2.1: Diagrams with a fermion loop and odd number of photon vertices in QED.

The above statement may be understood as we evaluate Green's functions with an odd number of gauge field operators. At zero temperature in QED, we are focusing on quantities such as $\langle 0|A_{\mu_1}A_{\mu_2}...A_{\mu_{2n+1}}|0\rangle$. Under the action of the charge conjugation

operator C, the photon vector gauge field transforms as $CA_\mu C^{-1} = -A_\mu$, while the vacuum is invariant under charge conjugation, $C|0\rangle = |0\rangle$. Thus, we obtain

$$\begin{aligned}\langle 0|A_{\mu_1}A_{\mu_2}...A_{\mu_{2n+1}}|0\rangle &= \langle 0|C^{-1}CA_{\mu_1}C^{-1}CA_{\mu_2}...A_{\mu_{2n+1}}C^{-1}C|0\rangle \\ =\langle 0|A_{\mu_1}A_{\mu_2}...A_{\mu_{2n+1}}|0\rangle(-1)^{2n+1} &= -\langle 0|A_{\mu_1}A_{\mu_2}...A_{\mu_{2n+1}}|0\rangle = 0. \end{aligned} \tag{2.1}$$

The expectation value of an odd number of gauge fields is zero. At a finite temperature T, the corresponding quantity to consider is

$$\mathrm{Tr}[\rho(\mu,\beta)A_{\mu_1}A_{\mu_2}...A_{\mu_{2n+1}}] = \sum_{n=-\infty}^{\infty}\langle n|A_{\mu_1}A_{\mu_2}...A_{\mu_{2n+1}}|n\rangle e^{-\beta(E_n-\mu Q_n)}, \tag{2.2}$$

where $\beta = 1/T$, μ is a chemical potential, and n is the number of thermal particles and anti-particles in the medium. Note $C|n\rangle = e^{i\phi}|-n\rangle$, where $|-n\rangle$ is a state in the ensemble with the same number of antiparticles as there are particles in $|n\rangle$ and vice-versa. At zero chemical potential, $\mu = 0$, inserting the operator $C^{-1}C$ as before, one obtains,

$$\langle n|A_{\mu_1}A_{\mu_2}...A_{\mu_{2n+1}}|n\rangle e^{-\beta E_n} = -\langle -n|A_{\mu_1}A_{\mu_2}...A_{\mu_{2n+1}}|-n\rangle e^{-\beta E_n}. \tag{2.3}$$

As the sum over all states in the ensemble contain the mirror term $\langle -n|A_{\mu_1}A_{\mu_2}...A_{\mu_{2n+1}}|-n\rangle e^{-\beta E_n}$, with the same thermal weight, it is zero,

$$\sum_n \langle n|A_{\mu_1}A_{\mu_2}...A_{\mu_{2n+1}}|n\rangle e^{-\beta E_n} = 0. \tag{2.4}$$

Thus, Furry's theorem still holds. However, for a charged QCD medium, $\mu \neq 0$, there are unequal number of particles and antiparticles. Under the action of charge conjugation,

$$\langle n|A_{\mu_1}A_{\mu_2}...A_{\mu_{2n+1}}|n\rangle e^{-\beta(E_n-\mu Q_n)} = -\langle -n|A_{\mu_1}A_{\mu_2}...A_{\mu_{2n+1}}|-n\rangle e^{-\beta(E_n-\mu Q_n)} \tag{2.5}$$

Now since the net charge of the state $|-n\rangle$ is weighted differently by the chemical potential, the mirror term becomes $\langle -n|A_{\mu_1}A_{\mu_2}...A_{\mu_{2n+1}}|-n\rangle e^{-\beta(E_n+\mu Q_n)}$, with a different thermal weight. As a result, the thermal expectation of an odd number of gauge field operators is non-vanishing,

$$\sum_n \langle n|A_{\mu_1}A_{\mu_2}...A_{\mu_{2n+1}}|n\rangle e^{-\beta(E_n-\mu Q_n)} \neq 0. \tag{2.6}$$

Thus Furry's theorem is now broken, leading to finite Green's functions, which allows the appearance of new processes in a perturbative expansion. One may say that the charge conjugation invariance is manifestly broken by the charged medium itself.

In the above discussion of Furry's theorem, we have focused on the diagrams in pure QED. The extension of the above statement to QCD is straightforward, i.e., processes with two gluons and an odd number of photon vertices (see Fig. 2.2). As been pointed out in Ref. [112] that the processes of Fig. 2.2 are also affected by the constraints imposed by Yang's theorem which states that a spin one particle may not decay or be formed by two identical massless vectors [124, 112]. However, the processes outlined in the following are computed within a thermalized medium, where the symmetry which underlies Yang's theorem is broken due to the presence of longitudinal gluon excitations.

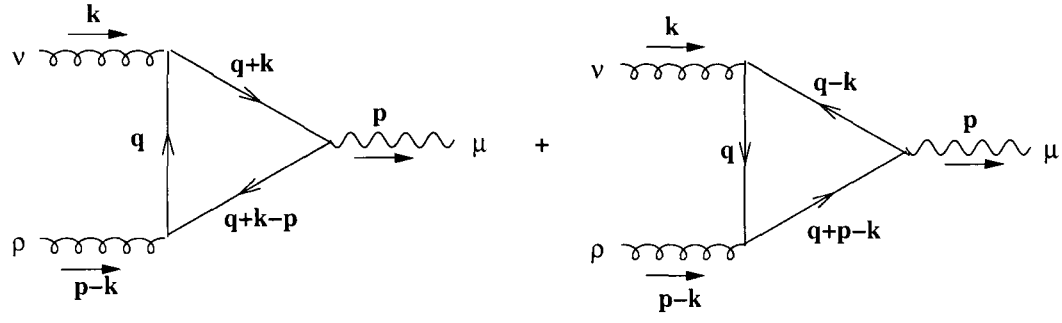

Figure 2.2: The one-loop Feynman diagrams of gluon-gluon-photon vertex as the sum of the two diagrams with quark numbers running in opposite directions in the quark triangle loops.

It should be noted that the incorporation of thermal gluon masses and self-energies in perturbation theory has to be done carefully, owing to issues arising from color gauge invariance. In this work, we carry out our calculation in the framework of gauge invariant resummed theory of Hard-Thermal-Loops [125], where one assumes the temperature $T \to \infty$ and as a result the coupling constant $g_s(T) \to 0$. Effective propagators and vertices involving soft $\sim g_s T$ momenta are obtained by integrating out the hard $\sim T$ modes. This allows for a well defined perturbative expansion of the photon production amplitude.

The Feynman diagrams corresponding to the leading contributions (in coupling) to the new channel of photon production are those of Fig. 2.2, with two gluons and a photon attached to a quark loop [111]. Such processes do not exist at zero temperature, or even at finite temperature and vanishing chemical potential. At non-zero density, this leads to two new sources for photon production: the fusion of gluons to form a photon ($gg \rightarrow \gamma$) and the decay of a massive gluon into a photon and a softer gluon ($g \rightarrow g\gamma$).

The full, physical, matrix element is obtained by summing contributions from both diagrams which have fermion number running in opposite directions,

$$T^{\mu\nu\rho}(p,k,p-k) = T_1^{\mu\nu\rho}(p,k,p-k) + T_2^{\mu\rho\nu}(p,p-k,k). \tag{2.7}$$

The amplitudes corresponding to these two diagrams may be expressed in the imaginary time formalism as:

$$\begin{aligned} T_1^{\mu\nu\rho}(p,k,p-k) &= T\sum_{q_0}\int \frac{d^3q}{(2\pi)^3} eg^2 \frac{\delta_{ab}}{2} \mathrm{Tr}[\gamma^\mu\gamma^\alpha\gamma^\nu\gamma^\beta\gamma^\rho\gamma^\gamma] \frac{(q+k)_\alpha q_\beta (q+k-p)_\gamma}{(q+k)^2 q^2 (q+k-p)^2} \\ T_2^{\mu\rho\nu}(p,p-k,k) &= T\sum_{q_0}\int \frac{d^3q}{(2\pi)^3} eg^2 \frac{\delta_{ab}}{2} \mathrm{Tr}[\gamma^\mu\gamma^\gamma\gamma^\rho\gamma^\beta\gamma^\nu\gamma^\alpha] \frac{(q-k)_\alpha q_\beta (q-k+p)_\gamma}{(q-k)^2 q^2 (q-k+p)^2}. \end{aligned} \tag{2.8}$$

The masses of quarks have been omitted as the momenta of the quarks is considered hard $\sim T$ in the HTL expansion. In the imaginary time formalism, the zeroth components of four momentum are discrete Matsubara frequencies,

$$q_0 = i\omega_n + \mu = i(2n+1)\pi T + \mu \ , \ k_0 = i\omega_k = i2m\pi T \ , \ p_0 = i\omega_p = i2l\pi T, \tag{2.9}$$

where integers n, m and l in the above expression range from $-\infty$ to ∞, and μ is the quark chemical potential. It may be easily demonstrated that [111], using the properties of the γ matrices,

$$\mathrm{Tr}[\gamma^\mu\gamma^\gamma\gamma^\rho\gamma^\beta\gamma^\nu\gamma^\alpha] = \mathrm{Tr}[\gamma^\alpha\gamma^\nu\gamma^\beta\gamma^\rho\gamma^\gamma\gamma^\mu] = \mathrm{Tr}[\gamma^\mu\gamma^\alpha\gamma^\nu\gamma^\beta\gamma^\rho\gamma^\gamma] \tag{2.10}$$

and changing integral variable $q \rightarrow -q$ in $T_2^{\mu\nu\rho}(p,p-k,k)$, we obtain

$$T_2^{\mu\rho\nu} = T\sum_{q_0}\int \frac{d^3q}{(2\pi)^3} eg^2 \frac{\delta_{ab}}{2} \mathrm{Tr}[\gamma^\mu\gamma^\alpha\gamma^\nu\gamma^\beta\gamma^\rho\gamma^\gamma] \frac{-(q+k)_\alpha q_\beta (q+k-p)_\gamma}{(q+k)^2 q^2 (q+k-p)^2}, \tag{2.11}$$

but with $q_0 = i\omega_n - \mu = (2n+1)\pi T - \mu$. It is obvious that these two amplitudes $T_1^{\mu\nu\rho}$ and $T_2^{\mu\nu\rho}$ cancel each other at zero chemical potential $\mu = 0$, consistent with the QCD generalization of Furry's theorem [122, 111, 112, 123].

The sum over the Matsubara frequencies may be conveniently performed using the non-covariant propagator method [111, 126, 127]. Here, one defines a time-three-momentum propagator $\tilde{\Delta}(\tau, E)$ in the mixed representation as (see Appendix B and D for details),

$$\tilde{\Delta}_\pm(\tau, E) = T\sum_n e^{-i\omega_n\tau}\tilde{\Delta}(i\omega_n \pm \mu, E) \tag{2.12}$$

The inverse transformation being

$$\tilde{\Delta}(i\omega_n \pm \mu, E) = \int_0^\beta d\tau e^{i\omega_n\tau}\tilde{\Delta}_\pm(\tau, E). \tag{2.13}$$

In the above equations, $E = |\vec{p}|$ represents the real energy of the particle from its three momentum, not the conjugate of the imaginary time τ. The explicit expression of the Matsubara propagator reads,

$$\begin{aligned}\tilde{\Delta}(i\omega_n \pm \mu, E) &= \frac{1}{(i\omega_n \pm \mu)^2 - E^2} \\ &= \sum_s \tilde{\Delta}_s(i\omega_n \pm \mu, E) = \sum_{s=\pm1} -\frac{s}{2E}\frac{1}{i\omega_n \pm \mu - sE}.\end{aligned} \tag{2.14}$$

The explicit expression of the imaginary time quark propagator in the mixed representation is given by

$$\tilde{\Delta}_\pm(\tau, E) = \sum_{s=\pm1}\tilde{\Delta}_{s,\pm}(\tau, E) = \sum_{s=\pm1} -\frac{s}{2E}\left[1 - \tilde{f}_\pm(sE)\right]e^{-\tau(sE\mp\mu)}, \tag{2.15}$$

where $\tilde{f}_\pm(E) = 1/(\exp[(E \mp \mu)/T] + 1)$ are Fermi-Dirac distribution functions. The amplitude may be expressed in terms of Matsubara propagator

$$\begin{aligned}T^{\mu\nu\rho} = T\sum_n \int \frac{d^3q}{(2\pi)^3}\frac{eg^2\delta_{ab}}{2}\mathrm{Tr}[\gamma^\mu\gamma^\alpha\gamma^\nu\gamma^\beta\gamma^\rho\gamma^\gamma](q+k)_\alpha q_\beta(q+k-p)_\gamma \\ \times\Big[\tilde{\Delta}(i\omega_n + i\omega_k + \mu, E_1)\tilde{\Delta}(i\omega_n + \mu, E_2)\tilde{\Delta}(i\omega_n + i\omega_k - i\omega_p + \mu, E_3) \\ -\tilde{\Delta}(i\omega_n + i\omega_k - \mu, E_1)\tilde{\Delta}(i\omega_n - \mu, E_2)\tilde{\Delta}(i\omega_n + i\omega_k - i\omega_p - \mu, E_3)\Big],\end{aligned} \tag{2.16}$$

where $E_1 = E_{q+k} = |\vec{q}+\vec{k}|$, $E_2 = E_q = |\vec{q}|$, and $E_3 = E_{q+k-p} = |\vec{q}+\vec{k}-\vec{p}|$. Now we are in the position to evaluate the following sum of the frequency ω_n,

$$\begin{aligned}
&T\sum_n \tilde{\Delta}(i\omega_n + i\omega_k \pm \mu, E_1)\tilde{\Delta}(i\omega_n \pm \mu, E_2)\tilde{\Delta}(i\omega_n + i\omega_k - i\omega_p \pm \mu, E_3) \\
=&T\sum_{ns_1s_2s_3} \tilde{\Delta}_{s_1}(i\omega_n + i\omega_k \pm \mu, E_1)\tilde{\Delta}_{s_2}(i\omega_n \pm \mu, E_2)\tilde{\Delta}_{s_3}(i\omega_n + i\omega_k - i\omega_p \pm \mu, E_3) \\
=&T\sum_{ns_1s_2s_3} \frac{1}{i\omega_p - s_1E_1 + s_3E_3}\left[\frac{s_3}{2E_3}\tilde{\Delta}_{s_2}\tilde{\Delta}_{s_1} - \frac{s_1}{2E_1}\tilde{\Delta}_{s_2}\tilde{\Delta}_{s_3}\right].
\end{aligned} \tag{2.17}$$

It is straightforward to show (see appendix D for derivation)

$$T\sum_{ns_2s_1} \tilde{\Delta}_{s_2}(i\omega_n \pm \mu, E_2)\tilde{\Delta}_{s_1}(i\omega_n + i\omega_k \pm \mu, E_1) = \sum_{s_1s_2} \frac{s_1s_2}{4E_1E_2}\frac{\tilde{f}_\pm(s_1E_1) - \tilde{f}_\pm(s_2E_2)}{i\omega_k - s_1E_1 + s_2E_2}. \tag{2.18}$$

Therefore, we obtain the expression for the sum of the frequency ω_n for the product of three propagators,

$$\begin{aligned}
&T\sum_n \tilde{\Delta}(i\omega_n + i\omega_k \pm \mu, E_1)\tilde{\Delta}(i\omega_n \pm \mu, E_2)\tilde{\Delta}(i\omega_n + i\omega_k - i\omega_p \pm \mu, E_3) \\
=&\sum_{s_1s_2s_3} \frac{s_1s_2s_3}{8E_1E_2E_3}\frac{1}{i\omega_p - s_1E_1 + s_3E_3} \\
&\times\left(\frac{\tilde{f}_\pm(s_1E_1) - \tilde{f}_\pm(s_2E_2)}{i\omega_k - s_1E_1 + s_2E_2} - \frac{\tilde{f}_\pm(s_3E_3) - \tilde{f}_\pm(s_2E_2)}{i\omega_k - i\omega_p - s_3E_3 + s_2E_2}\right).
\end{aligned} \tag{2.19}$$

Adding two diagrams together, we obtain

$$\begin{aligned}
&T\sum_n \Big[\tilde{\Delta}(i\omega + i\omega_{kn} + \mu, E_1)\tilde{\Delta}(i\omega_n + \mu, E_2)\tilde{\Delta}(i\omega_n + i\omega_k - i\omega_p + \mu, E_3) \\
&\qquad -\tilde{\Delta}(i\omega_n + i\omega_k - \mu, E_1)\tilde{\Delta}(i\omega_n - \mu, E_2)\tilde{\Delta}(i\omega_n + i\omega_k - i\omega_p - \mu, E_3)\Big] \\
=&\sum_{s_1s_2s_3} \frac{s_1s_2s_3}{8E_1E_2E_3}\frac{1}{i\omega_p - s_1E_1 + s_3E_3} \\
&\times\left(\frac{\Delta\tilde{f}(s_1E_2) - \Delta\tilde{f}(s_2E_2)}{i\omega_k - s_1E_1 + s_2E_2} - \frac{\Delta\tilde{f}(s_3E_3) - \Delta\tilde{f}(s_2E_2)}{i\omega_k - i\omega_p - s_3E_3 + s_2E_2}\right),
\end{aligned} \tag{2.20}$$

where we have used the shorthand, $\Delta\tilde{f}(sE) = \tilde{f}_+(sE) - \tilde{f}_-(sE)$. Now with the use of the identity $\tilde{f}_\pm(-E) = 1 - \tilde{f}_\mp(E)$, it is straightforward to obtain

$$\Delta\tilde{f}(sE) = \tilde{f}_+(sE) - \tilde{f}_-(sE) = \tilde{f}_+(E) - \tilde{f}_-(E) = \Delta\tilde{f}(E), \tag{2.21}$$

for both $s = 1$ and $s = -1$. Furthermore, from the following identities,

$$\frac{\partial\tilde{\Delta}_{\pm}(\tau, E_q)}{\partial\tau} = T\sum_n(-i\omega_n)e^{-i\omega_n\tau}\tilde{\Delta}(i\omega_n \pm \mu, E_q)$$
$$\frac{\partial\tilde{\Delta}_{\pm}(\tau, E_q)}{\partial\tau} = \sum_s\left[-(sE_q \mp \mu)\right](-\frac{s}{2E_q})\left[1 - \tilde{f}_{\pm}(sE_q)\right]e^{-\tau(sE_q-\mu)}, \qquad (2.22)$$

we may put quark momenta $(q+k)_\alpha$, q_β and $(q+p-p)_\gamma$ inside the sums over s_1, s_2 and s_3 by substituting them with $(q+k)_{s_1\alpha}$, $q_{s_2\beta}$ and $(q+k-p)_{s_3\gamma}$, respectively, where $q_s = (sE_q, \vec{q})$. After performing the summation of the Matsubara frequency ω_n in the quark propagators, we obtain

$$T^{\mu\nu\rho} = \int\frac{d^3q}{(2\pi)^3}\frac{eg^2\delta_{ab}}{2}\mathrm{Tr}[\gamma^\mu\gamma^\alpha\gamma^\nu\gamma^\beta\gamma^\rho\gamma^\gamma]$$
$$\times\sum_{s_1s_2s_3}\frac{s_1s_2s_3}{8E_{q+k}E_qE_{q+k-p}}\frac{(q+k)_{s_1\alpha}q_{s_2\beta}(q+k-p)_{s_3\gamma}}{i\omega_p - s_1E_{q+k} + s_3E_{q+k-p}}$$
$$\times\left(\frac{\Delta\tilde{f}(E_{q+k}) - \Delta\tilde{f}(E_q)}{i\omega_k - s_1E_{q+k} + s_2E_q} - \frac{\Delta\tilde{f}(E_{q+k-p}) - \Delta\tilde{f}(E_q)}{i\omega_k - i\omega_p - s_3E_{q+k-p} + s_2E_q}\right). \qquad (2.23)$$

Our next task is to evaluate the sum over s_1, s_2 and s_3 to obtain the photon production amplitude. This is carried out in the HTL approximation for the quark loop. In this limit, the photon and gluon momenta are considered soft $p, k \sim g_sT$, and the quark momenta are hard $q \sim T$, where T is the temperature and g_s is the effective coupling constant in the medium. The quark lines which carry a component of the external gluon energies are Taylor expanded as follows,

$$E_{q+k} \approx E_q + \vec{k}\cdot\hat{q} + \frac{\vec{k}^2 - (\vec{k}\cdot\hat{q})^2}{2E_q}\ ,\ \frac{(q+k)_{s\alpha}}{E_{q+k}} \approx \hat{q}_{s\alpha} + \frac{k}{2E_q}\hat{\mathcal{K}}_\alpha, \qquad (2.24)$$

where $\hat{q}_s = (s, \hat{q})$ and $\hat{\mathcal{K}} = 2(0, \hat{k} - (\hat{k}\cdot\hat{q})\hat{q})$. Similarly, for any function $f(E_{q+k})$, we have the following expansion, for $k \ll q$,

$$f(E_{q+k}) = f(E_q) + \vec{k}\cdot\hat{q}\frac{df(E_q)}{dE_q} + \frac{\vec{k}^2 - (\vec{k}\cdot\hat{q})^2}{2E_q}\frac{df(E_q)}{dE_q} + \frac{(\vec{k}\cdot\hat{q})^2}{2}\frac{d^2f(E_q)}{dE_q^2}. \qquad (2.25)$$

The above approximation allows for a factorization of the quark angular integral. In the limit of high temperature, we may perform the integral over the magnitude of the quark momentum $\vec{q}$ analytically,

$$\int_0^\infty q^2dq\frac{d\Delta\tilde{f}}{dE_q} = -\frac{1}{3}\log[4096]\mu T,\ \int_0^\infty q^2dq\frac{1}{E_q}\frac{d\Delta\tilde{f}}{dE_q} = -\mu,\ \int_0^\infty q^2dq\frac{d^2\Delta\tilde{f}}{dE_q^2} = 2\mu. \qquad (2.26)$$

After substituting the above expressions, we find that the leading order terms proportional to $d\Delta\widetilde{f}(E_q)/dE_q$ are cancelled automatically. Putting all together leads to the following expression for the amplitude,

$$
\begin{aligned}
T^{\mu\nu\rho} = \int \frac{d\Omega_q}{(2\pi)^3}\frac{eg^2\delta_{ab}}{2}\frac{\mu}{8}Tr[\gamma^\mu\gamma^\alpha\gamma^\nu\gamma^\beta\gamma^\rho\gamma^\gamma] \\
\times\Bigg\{ -\frac{\hat{q}_{+\alpha}\hat{q}_{+\beta}\hat{q}_{+\gamma}}{p\cdot\hat{q}_+}\left(\frac{\vec{k}^2-(\vec{k}\cdot\hat{q})^2}{k\cdot\hat{q}_+}+\frac{\vec{k}'^2-(\vec{k}'\cdot\hat{q})^2}{k'\cdot\hat{q}_+}\right) \\
-\frac{k\hat{\mathcal{K}}_\alpha\hat{q}_{+\beta}\hat{q}_{+\gamma}-k'\hat{q}_{+\alpha}\hat{q}_{+\beta}\hat{\mathcal{K}}'_\gamma}{p\cdot\hat{q}_+}\left(\frac{\vec{k}\cdot\hat{q}}{k\cdot\hat{q}_+}-\frac{\vec{k}'\cdot\hat{q}}{k'\cdot\hat{q}_+}\right) \\
-\frac{\hat{q}_{+\alpha}\hat{q}_{+\beta}\hat{q}_{+\gamma}}{p\cdot\hat{q}_+}\frac{[\vec{k}^2-(\vec{k}\cdot\hat{q})^2]-[\vec{k}'^2-(\vec{k}'\cdot\hat{q})^2]}{p\cdot\hat{q}_+}\left(\frac{\vec{k}\cdot\hat{q}}{k\cdot\hat{q}_+}-\frac{\vec{k}'\cdot\hat{q}}{k'\cdot\hat{q}_+}\right) \\
-\frac{\hat{q}_{+\alpha}\hat{q}_{+\beta}\hat{q}_{+\gamma}}{p\cdot\hat{q}_+}\left(\frac{\vec{k}\cdot\hat{q}}{k\cdot\hat{q}_+}\frac{\vec{k}^2-(\vec{k}\cdot\hat{q})^2}{k\cdot\hat{q}_+}+\frac{\vec{k}'\cdot\hat{q}}{k'\cdot\hat{q}_+}\frac{\vec{k}'^2-(\vec{k}'\cdot\hat{q})^2}{k'\cdot\hat{q}_+}\right) \\
+\frac{2\hat{q}_{+\alpha}\hat{q}_{+\beta}\hat{q}_{+\gamma}}{p\cdot\hat{q}_+}\left(\frac{(\vec{k}\cdot\hat{q})^2}{k\cdot\hat{q}_+}+\frac{(\vec{k}'\cdot\hat{q})^2}{k'\cdot\hat{q}_+}\right) \\
-\hat{q}_{-\alpha}\hat{q}_{+\beta}\hat{q}_{+\gamma}\frac{\vec{k}'\cdot\hat{q}}{k'\cdot q_+}-\hat{q}_{+\alpha}\hat{q}_{-\beta}\hat{q}_{+\gamma}\frac{\vec{p}\cdot\hat{q}}{p\cdot\hat{q}_+}-\hat{q}_{+\alpha}\hat{q}_{+\beta}\hat{q}_{-\gamma}\frac{\vec{k}\cdot\hat{q}}{k\cdot\hat{q}_+}\Bigg\}, \qquad (2.27)
\end{aligned}
$$

where $k' = p - k$ and $d\Omega_q = d\cos d\theta_q d\phi_q$ is the differential solid angle of the quark momentum $\vec{q}$. The first line of the above equation, demonstrates explicitly that the amplitude is directly proportional to the chemical potential μ. As a result, the contribution to the photon production rate from this channel will grow quadratically with increasing chemical potential if the temperature of the medium is held constant. It is noted that in the above equation, the gluon energy $k_0 = i\omega_k$ is still an imaginary frequency and its sum will be performed later in the calculation of the imaginary part of the photon self-energy.

The remaining nontrivial angular integral over $d\Omega_q$ is performed numerically. The possibility of radiation or absorption of a space-like gluon by an on-shell quark induces an enhancement in a small part of phase space ($k\cdot\hat{q}_+ \sim 0$) in each of the two diagrams separately. In this regime of phase space, we may perform the integration over $\cos\theta_{kq}$

analytically if we employ the following expansions,

$$\cos\theta_{kq} \approx \frac{k_0}{k} + \frac{k}{2q}\sqrt{1-\frac{k_0^2}{k^2}}u, \quad \hat{q}_s \approx \hat{\tilde{q}}_s + \frac{k}{2q}u\hat{\mathcal{Q}}, \tag{2.28}$$

where $\hat{\tilde{q}}$ and $\mathcal{Q}$ are given by

$$\begin{aligned}\hat{\tilde{q}}_s &= \left(s, \sqrt{1-k_0^2/\vec{k}^2}\cos\phi, \sqrt{1-k_0^2/\vec{k}^2}\sin\phi, k_0/k\right)\\ \hat{\mathcal{Q}} &= \left(0, -k_0/k\sqrt{1-k_0^2/\vec{k}^2}\cos\phi, -k_0/k\sqrt{1-k_0^2/\vec{k}^2}\sin\phi, 1-k_0^2/\vec{k}^2\right).\end{aligned} \tag{2.29}$$

In the above expansion, we have chosen the z-axis as the direction of the photon momentum $\vec{k}$. Performing the integral over new variable u in this part of phase space, we find that such contributions are diminished by the destructive interference between the two diagrams. Including all contributions leads to the survival of only the imaginary part of the amplitude in this sector. The resulting expression is,

$$\begin{aligned}T^{\mu\nu\rho} = \int \frac{d\phi}{(2\pi)^3}\frac{eg^2\delta_{ab}}{2}\mathrm{Tr}[\gamma^\mu\gamma^\alpha\gamma^\nu\gamma^\beta\gamma^\rho\gamma^\gamma]\left(-\frac{\mu\omega}{8k}\right)i\pi\\ \times\left\{-\frac{1}{p\cdot\hat{\tilde{q}}}\left(k\hat{\mathcal{K}}_\alpha\hat{\tilde{q}}_{+\beta}\hat{\tilde{q}}_{+\gamma} - k'\hat{\tilde{q}}_{+\alpha}\hat{\tilde{q}}_{+\beta}\hat{\mathcal{K}'}_\gamma\right)\right.\\ -\frac{[\vec{k}^2-(\vec{k}\cdot\hat{\tilde{q}})^2]-[\vec{k}'^2-(\vec{k}'\cdot\hat{\tilde{q}})^2]}{(p\cdot\hat{\tilde{q}}_+)^2}\hat{\tilde{q}}_{+\alpha}\hat{\tilde{q}}_{+\beta}\hat{\tilde{q}}_{+\gamma}\\ \left.+\frac{k}{p\cdot\hat{\tilde{q}}}\left(\hat{\mathcal{Q}}_\alpha\hat{\tilde{q}}_{+\beta}\hat{\tilde{q}}_{+\gamma}+\hat{\tilde{q}}_{+\alpha}\hat{\mathcal{Q}}_\beta\hat{\tilde{q}}_{+\gamma}+\hat{\tilde{q}}_{+\alpha}\hat{\tilde{q}}_{+\beta}\hat{\mathcal{Q}}_\gamma\right)-\hat{\tilde{q}}_{+\alpha}\hat{\tilde{q}}_{+\beta}\hat{\tilde{q}}_{-\gamma}\right\},\end{aligned} \tag{2.30}$$

Note that while the result has been derived in a thermalized environment, it may be easily generalized to moderate departures from equilibrium, which will remain the subject of a future effort. In the following sections, the above amplitude will be applied to compute the photon production rate from the fusion of gluons to form a photon or the decay of a gluon into a photon and a gluon of lower energy in the simplest model of a QGP, a plasma of quasi-particle quarks and gluons in complete thermal and chemical equilibrium.

2.3 The photon production rate

In the case of a medium in complete thermal and chemical equilibrium, the thermal photon emission rate $R = d^4N/d^4x$ is related to the discontinuity or the imaginary

part of the retarded photon self-energy $\Pi^R_{\mu\nu}$ at finite temperature T through the relation [73, 128, 129],

$$E\frac{dR}{d^3p} = -\frac{1}{(2\pi)^3}\mathrm{Im}\Pi^{R,\mu}_{\mu}\frac{1}{e^{\frac{E}{T}}-1}, \tag{2.31}$$

where E and p are the energy and momentum of the photons. This formula is valid to all orders of strong interactions, but only to e^2 in the electromagnetic interactions, as the photons, once produced, will tend to escape from the matter without further interaction. In what follows, the focus will lie on the imaginary part of the photon self-energy of Fig. 2.3.

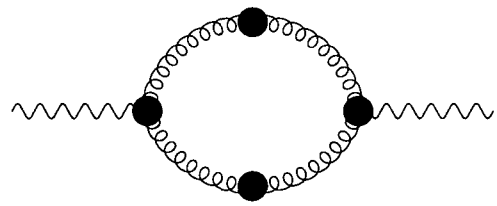

Figure 2.3: The Feynman diagram of the photon self-energy evaluated in this chapter, where the dark blobs represent effective vertices or propagators in the HTL approximation.

The photon self-energy from the Feynman diagram in Fig. 2.3 may be expressed formally as,

$$\Pi^{\mu\mu'}(p) = T\sum_{k_0}\int\frac{d^3k}{(2\pi)^3}T^{\mu\nu\rho}(p,k,p-k)S_{\nu\nu'}(k)T^{\prime\mu'\nu'\rho'}(-p,-k,-p+k)S_{\rho\rho'}(p-k), \tag{2.32}$$

where $T^{\mu\nu\rho}(p,k,p-k)$ is the effective photon-gluon-gluon vertex evaluated in the last section, and $S_{\mu\nu}(k)$ is the effective gluon propagator, after summing up all the HTL contributions to the self-energy of the gluon. In the Coulomb gauge, the effective propagator is given by [129]

$$S_{\mu\nu}(k) = \Delta_T(k_0,k)P^{\mu\nu}_T + \Delta_L(k_0,k)u_\mu u_\nu, \tag{2.33}$$

In the above equation, $P^T_{00}(k) = 0$, $P^T_{ij}(k) = \delta_{ij} - k_ik_j/\vec{k}^2$ is the transverse projection tensor, and $u^\mu = (1,0,0,0)$ specifies the rest frame of the medium. $\Delta_L(k_0,k)$ and $\Delta_T(k_0,k)$ are longitudinal and transverse gluon propagators,

$$\Delta_T(k_0,k) = \frac{1}{F_T - k^2}, \quad \Delta_L(k_0,k) = \frac{1}{F_L - k^2}\frac{k^2}{\vec{k}^2}, \tag{2.34}$$

where the explicit expressions for $F_L(k_0, k)$ and $F_T(k_0, k)$ are,

$$F_L = 2m_g^2(1-x^2)(1-xQ_0(x)) \ , \quad F_T = m_g^2 - \frac{F_L}{2}. \tag{2.35}$$

In the above equations, $Q_0(x) = \frac{1}{2}\ln\frac{x+1}{x-1}$ is the Legendre function with $x = \omega/q$, and m_g is the thermal gluon mass,

$$m_g^2 = \frac{1}{6}C_A g^2 T^2 + \frac{1}{12}N_F g^2\left(T^2 + \frac{3\mu^2}{\pi^2}\right), \tag{2.36}$$

where $C_A = 3$ is the $SU(3)$ group factor, and N_f is the number of quark flavors.

In the complex k_0 plane, the longitudinal and transverse propagators exhibit a discontinuity or cut from $-k$ to k; in addition, they have poles at $k_0 = \pm\omega_{T,L}(k)$, which give the two dispersion relations for the longitudinal and transverse modes of the gluons in the medium. The expressions for $\omega_T(k)$ and $\omega_L(k)$ are determined by the following equations [129, 126],

$$\begin{aligned} x_T^2 - 1 - \frac{m_g^2}{k^2}\left[x_T^2 + \frac{x_T(1-x_T^2)}{2}\ln\frac{x_T+1}{x_T-1}\right] &= 0 \\ 1 + \frac{2m_g^2}{k^2}\left[1 - \frac{x_L}{2}\ln\frac{x_L+1}{x_L-1}\right] &= 0 \end{aligned} \tag{2.37}$$

where $x_T = \omega_T/k$ and $x_L = \omega_L/k$. These two equations can be solved numerically. In Fig. 2.4, two dispersion relations $\omega_T(k)$ and $\omega_L(k)$ are plotted. In the plot, the upper branch is the dispersion relation for transverse excitation modes, and the lower branch is for the longitudinal one. The solid line represents the light cone.

In order to calculate the thermal photon differential production rate, we evaluate the imaginary part or the discontinuity of the photon self-energy, which involves evaluating its various cuts. In the interest of a physical interpretation of the various cuts, the polarization tensor $P^T_{\mu\nu}(k)$ may be expanded as a product of polarization vectors as $P^T_{\mu\nu}(k) = \epsilon_{+\mu}(k)\epsilon^*_{+\nu}(k) + \epsilon_{-\mu}(k)\epsilon^*_{-\nu}(k)$, where the z-axis is chosen as the direction of the photon momentum $\vec{k}$. Then the effective propagator may be formally written as

$$S_{\mu\nu}(k) = \sum_{i=+,-,0} \Delta_i(k)\epsilon_{i\mu}(k)\epsilon_{i\nu}(k), \tag{2.38}$$

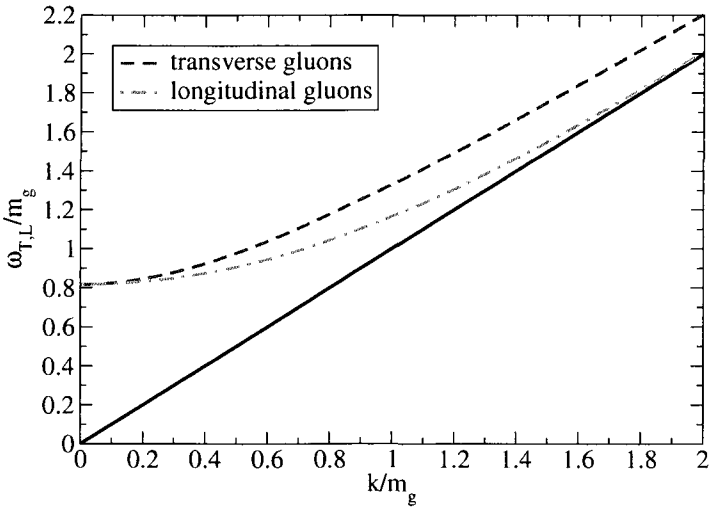

Figure 2.4: The dispersion relations $\omega_{T,L}(k)$ for transverse gluons and longitudinal gluons in a quark-gluon plasma, where m_g is the thermal gluon mass.

where we set $\epsilon_0^\mu = u^\mu = (1,0,0,0)$ and $\Delta_\pm = \Delta_T$, $\Delta_0 = \Delta_L$. The entire expression for the rate, may be expressed in a factorized form $f(k_0)g(p_0 - k_0)$, where k_0 is the Matsubara frequency of the gluon and p_0 is the frequency of the external photon. The remaining sum over k_0 and the discontinuity across the real p_0 is achieved by means of the identity, [111, 130] (see Appendix D for derivation),

$$\mathrm{Disc}T\sum_{k_0} f(k_0)g(p_0-k_0) = 2\pi i\int d\omega\int d\omega'\rho_1(\omega)\rho_1(\omega')\delta(\omega+\omega'-E)(1+f(\omega)+f(\omega')),$$

where $f(\omega)$ and $f(\omega')$ are the thermal distribution functions of gluons, and $\rho_1(\omega)$ and $\rho_2(\omega')$ are the spectral functions of $f(k_0)$ and $g(p_0 - k_0)$. The spectral function $\rho(z)$ for $f(z)$ is defined as $\rho(z) = \mathrm{Disc}f(z)/(2\pi i)$. Employing the above formula, the discontinuity in the photon self-energy may be expressed in a kinetic form,

$$E\frac{dR}{d^3p} = \sum_{l=\pm}\sum_{i,j=\pm,0}\frac{1}{2(2\pi)^2}\frac{1}{e^{\frac{E}{T}}-1}\int\frac{d^3k}{(2\pi)^3} \times\int d\omega\int d\omega'\rho_i(\omega)\rho_j(\omega')\delta(\omega+\omega'-E)(1+f(\omega)+f(\omega'))|M_{lij}|^2, \quad (2.39)$$

where the matrix element $M_{lij} = \epsilon_{l\mu}(p)\epsilon_{i\nu}(k)\epsilon_{j\rho}(p-k)T^{\mu\nu\rho}(p,k,p-k)$, and $\rho_i(\omega)$ and $\rho_j(\omega')$ are the spectral functions of the gluon propagators Δ_i and Δ_j.

$$\rho_{T,L}(k_0,k) = Z_{T,L}(k)[\delta(k_0-\omega_{T,L}(k))-\delta(k_0+\omega_{T,L}(k))] + \beta_{T,L}(k_0,k)\theta(k^2-k_0^2), \quad (2.40)$$

where the explicit expressions of $Z_{L,T}$ and $\beta_{L,T}$ are given by [129]

$$Z_L(k) = \frac{\omega_L(\omega_L^2 - k^2)}{k^2(k^2 + 2m_g^2 - \omega_L^2)}, \; Z_T(k) = \frac{\omega_T(\omega_T^2 - k^2)}{2m_g^2\omega_T^2 - (\omega^2 - k^2)^2}, \tag{2.41}$$

and

$$\begin{aligned}\beta_L(k_0,k) &= \frac{m_g^2 x}{(k^2 + 2m_g^2(1 - \frac{x}{2}\ln|\frac{x+1}{x-1}|)^2 + \pi^2 m_g^4 x^2} \\ \beta_T(k_0,k) &= \frac{\frac{1}{2}m_g^2 x(1-x^2)}{k^2(x^2-1) - m_g^2(x^2 + \frac{x}{2}(1-x^2)\ln|\frac{x+1}{x-1}|)^2 + \frac{1}{4}\pi^2 m_g^4 x^2(1-x^2)^2}.\end{aligned} \tag{2.42}$$

The two spectral functions contain contributions from the poles $\omega_{T,L}$ with residue $Z_{T,L}$ as well as from the branch cuts $\beta_{T,L}$. The product of two ρ functions give three types of contribution: pole-pole, pole-cut, and cut-cut. The pole-pole terms represent the process involving two quasi-particles with dispersion relations displayed in Fig. 2.4. The terms from the cuts represents the processes involving space-like gluons from the medium, *i.e.*, gluons which are intermediate states of a scattering process. In this first effort, the focus will lie on the hard photon production rate, *i.e.*, photons with momenta $p \sim T$. This requires that at least one of the gluons in Fig. 2.3 to be hard. While in the usual HTL prescription, such particles receive suppressed contributions from hard loops, a component of the HTL self-energy which produces a thermal gluon mass is retained. The cut-cut contribution with two space-like gluons is dominant only in the region where both gluon momenta are soft and is ignored in this effort.

2.4 Results

In this section, we will present the numerical results for the hard photon production rate from our new channel in a plasma with finite baryon density. Here we only consider two massless flavors of quarks with equal chemical potentials $\mu_u = \mu_d = \mu_B/3$ and the strange sector has been ignored in this calculation. The strong coupling constant is set to be $\alpha_s = 0.4$ in such a plasma.

In Fig. 2.5, the photon production from our new channel ($gg\gamma$ vertex) is compared with the contribution from the leading order QCD annihilation process ($q\bar{q} \to g\gamma$) and Compton scattering ($qg \to qg$). The photon differential rate from annihilation

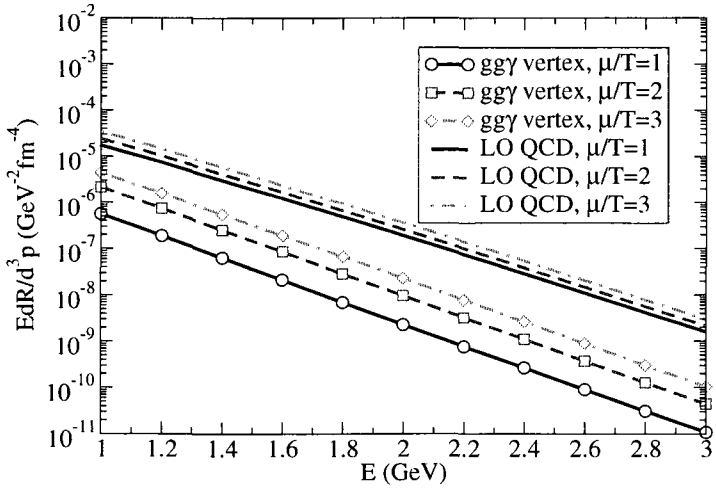

Figure 2.5: The differential rate of photons from $gg\gamma$ vertex in a hot and dense medium with temperature $T = 200$MeV compared with the contribution from QCD annihilation and Compton processes.

and Compton processes at finite temperature and chemical potential is parameterized as in Ref.[75, 120, 121] by

$$E\frac{dR}{d^3p} = \frac{5}{9}\frac{\alpha_e\alpha_s}{2\pi^2}\left(T^2+\frac{\mu^2}{\pi^2}\right)e^{-\frac{E}{T}}\ln\left(\frac{2.912ET}{g^2(T^2+\mu^2/\pi^2)}+G\right), \tag{2.43}$$

where the dimensionless quality G is fitted to be $G = \ln(1+\mu^2/\pi^2T^2)$ for $\mu/T \leq 1$ and $G = \ln(1+0.139\mu^2/T^2)$ for $\mu/T \geq 1$.

From Fig. 2.5, one may immediately find that the contribution from the new channels ($gg\gamma$ vertex) to the photon production is much smaller than the QCD annihilation and Compton processes at low chemical potential. However, with increasing chemical potential at a fixed temperature, the photon production rate from the $gg\gamma$ vertex tends to increase at a larger rate. This may be understood from the fact that the matrix element corresponding to the $gg\gamma$ vertex in Fig. 2.2 is proportional to the chemical potential as we see from Eq. (2.27). Thus, we will expect that in baryon-rich matter such as that produced in low energy collisions of heavy ions or in the core of neutron stars, the new channel from $gg\gamma$ vertex will become significant in comparison to the leading order QCD rates. Interestingly, the new FAIR accelerator at GSI will have the mandate to explore the realm of high baryon densities.

In the above estimates, the chemical potential and temperature are held fixed separately. It has been shown in Ref. [118, 120, 121] that the photon production rate from leading order QCD processes have a strong dependence on increasing chemical potential μ of the medium if the energy density of the medium is fixed. If the energy density were held constant, the temperature T and μ are related to each other by the equation of state. Here we use the equation of state derived from the phenomenological MIT bag model [30, 118, 120, 121] (see Chapter 1). In this case, the energy density is given as,

$$\epsilon = \left(\frac{37\pi^2}{30} - \frac{11\pi\alpha_s}{3}\right)T^4 + 3\left(1 - \frac{2\alpha_s}{\pi}\right)T^2\mu^2 + \frac{3}{2\pi^2}\left(1 - \frac{2\alpha_s}{\pi}\right)\mu^4 + B, \quad (2.44)$$

where the bag constant B is fixed to be 200 MeV^4. If T is made dependent of μ in this way, then both rates will decrease strongly with increasing chemical potential because of the decreasing of the temperature T of the medium. At RHIC, one expects a maximum energy density of about $\epsilon = 5$ GeV/fm^3, and the average energy density will be smaller than this value. We pick a conservative estimate of $\epsilon = 1.8$ GeV/fm^3, which corresponding to $T = 200$ MeV at zero chemical potential.

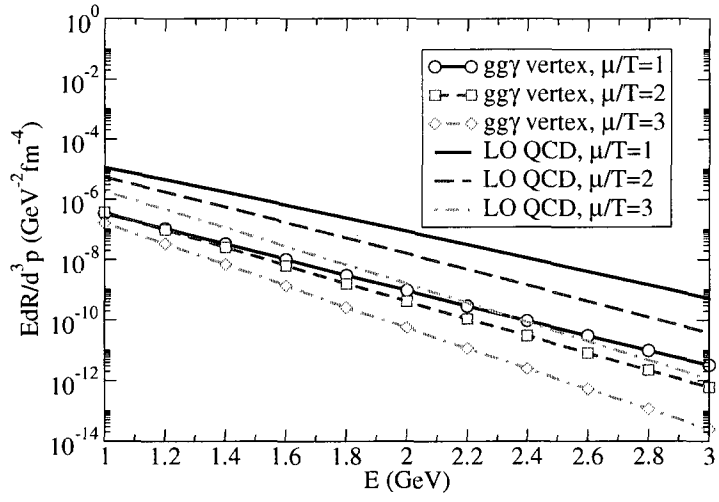

Figure 2.6: The differential rate of photons from $gg\gamma$ vertex in a hot and dense medium with energy density fixed, $\epsilon = 1.8$GeV/fm^3, compared with the contribution from QCD annihilation and Compton processes.

In Fig. 2.6, the result of the leading order rate and that from the new channels

($gg\gamma$ vertex) is presented, where we increase the chemical potential μ from $\mu/T = 1$ to $\mu/T = 3$. As may be seen from the plot, the photon production rate from our new channel ($gg\gamma$ vertex) decreases with increasing chemical potential with fixed energy density, showing a similar dependence to the QCD leading order processes. It would appear that with energy density fixed, the photon production from our new channel has a much stronger dependence on the temperature than on the chemical potential and has not exceeded the photon production rate from QCD annihilation and Compton processes in the range of energies explored. It should be noted that the above statement may not be true for soft photons where cut-cut contributions need to be incorporated.

2.5 Conclusions

In the present chapter, we have presented the hard photon signature emanating from the gluon fusion channel. We employed an effective field theory of QCD at high temperature (HTL) and focus the photon spectrum from a medium at equilibrium. It is found that the hard photon production rate from this channel tends to be suppressed compared to the leading order rate from QCD annihilation and Compton process for realistic values of temperature and chemical potential, but will gain significance in baryon-rich matter. Since photon production from such channels is dependent on the gluon density of the medium, it offers a new window to probe the gluon sector of the highly excited strongly interacting matter.

Our results may be extended to non-equilibrium cases, such as in the early stages of relativistic heavy ion collisions. In such a scenario, the gluon populations are much larger than those of quarks, and the photon production from this new mechanism could outshine that from conventional channels. Another application of such rates is to photon production in neutron stars where the chemical potential far exceeds the temperature and many of the conventional channels are Pauli blocked. It would be highly interesting to estimate the photon production rate from two gluons in such diverse scenarios, and this is left for future efforts.

3

Photon and gluon bremsstrahlung in the AMY formalism

In this chapter, we briefly review the Arnold-Moore-Yaffe formalism (AMY) [93, 94, 95] for photon and gluon bremsstrahlung in a quark-gluon plasma. We first discuss the complete leading-order result of thermal photon emission rates from a quark-gluon plasma, including $2 \longrightarrow 2$ processes as well as bremsstrahlung and inelastic pair annihilation processes with Landau-Pomeranchuk-Migdal (LPM) effect [87]. Then the induced photon emission from bremsstrahlung with LPM effect is generalized to induced gluon bremsstrahlung process. Later, we follow Ref. [131] and present some simple applications to the calculation of radiative part of jet energy loss in the quark-gluon plasma. In the last section, the applicability of the AMY formalism is discussed [131, 132].

In AMY, it is simply assumed that the temperature T of the quark-gluon plasma is so high that one may treat QCD running coupling constant $g_s(T)$ as a parametrically small quantity. This allows us to compute the leading order photon and gluon emission rates using perturbation theory. As the temperature T is the only momentum scale in the quark-gluon plasma, we usually call those particles with momenta of order T hard particles, those with momenta of order g_sT soft particles, and those with momenta of order g_s^2T ultra-soft particles.

It should be emphasized that we treat the quark-gluon plasma as a relativistic dynamical medium, with moving scattering centers. The screened color electric and magnetic field generated by the medium is treated as a classical random background field, and photons and gluons are emitted when an energetic parton is propagating through such a color gauge field. It has been shown in the model that by simple

physical considerations of localization of particles in both space and momentum, the LPM effect in bremsstrahlung can be interpreted as an infinite sum of self-energy diagrams, called ladder diagrams. As it is just a geometric series, the resulting sum is then converted into a linear integral equation, from which the photon and gluon emission rates are computed.

3.1 Complete LO result for photon emission from QGP

It is of great importance for theory to establish the production rates of photons from the quark-gluon plasma. According to QCD theory, the simplest diagrams contributing to the leading order photon emission rate are $2 \to 2$ processes, such as annihilation process $q\bar{q} \to g\gamma$ and Compton scattering process $q(\bar{q})g \to q(\bar{q})\gamma$, as shown in Fig. 3.1.

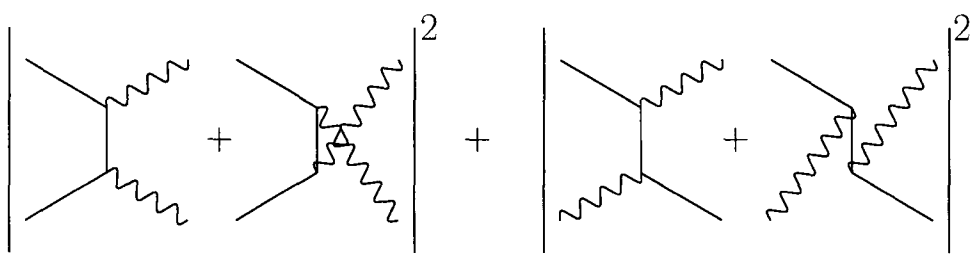

Figure 3.1: QCD annihilation process and Compton scattering – $2 \to 2$ processes that contribute to the leading order photon production rate.

Perturbative QCD calculations of photon emission rate from annihilation and Compton scattering processes encountered the infrared singularity when the exchanged momenta in internal quark lines are zero. It was shown in Ref. [75] that this divergence can be circumvented by using the hard thermal loop (HTL) approximation [125], where the correlation functions are expanded in terms of effective dressed propagators and vertices instead of bare ones. One may introduce an arbitrary momentum scale to separate the photon emission rate into soft contribution (with quark momentum of order $g_s T$) and hard contribution (with quark momentum of order T). The soft contribution is computed with appropriately dressed propagators in one-loop photon

self-energy as shown in Fig. 3.2, and the hard contribution can be computed using perturbative methods in kinetic theory. When the two parts of the contribution are finally put together, the result is independent of the arbitrary separation scale as it should be.

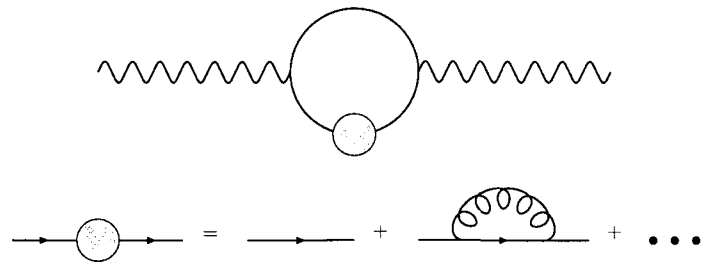

Figure 3.2: The one-loop hard photon self-energy with one of the quark propagators being dressed.

If we define the photon emission rate per unit volume $R_\gamma = dN_\gamma/d^3xdt$, the final result of photon emission rate from $2 \to 2$ processes is given by [75, 93, 94, 95],

$$\frac{(2\pi)^3 dR_\gamma^{2\to 2}}{d^3k} = \sum_f \left(\frac{e_f}{e}\right)^2 \frac{8\pi\alpha_e\alpha_s T^2}{k} f_F(k) \left(\frac{1}{2}\ln\frac{kT}{m_q^2} + C_{2\to 2}(k/T)\right), \tag{3.1}$$

where $f_F(k) = 1/[\exp(k/T) + 1]$ is Fermi-Dirac thermal distribution function and m_q is the thermal gluon mass, $m_q^2 = g_s^2 T^2/6$. In the limit of $k \gg T$, $C_{22}(k/T)$ is a constant given by

$$C_{2\to 2}(k/T) = -\frac{1}{4} - \frac{\gamma_E}{2} + \frac{2}{3}\ln 2 + \frac{\zeta'(2)}{2\zeta(2)} \approx -0.3614902. \tag{3.2}$$

As for any value of k, it has been shown in Ref. [93, 94, 95] that the following simple parametrization may reproduce the numerical values of $C_{2\to 2}(x)$ quite accurately,

$$C_{2\to 2}(x) \approx -0.3615 + \frac{0.041}{x} + 1.01e^{-1.35x}. \tag{3.3}$$

One might expect that $2 \to 2$ processes are the complete lowest order result for the photon production in the quark-gluon plasma at leading order $\mathcal{O}(\alpha_e\alpha_s)$. But it was pointed out in Ref. [93, 133, 94] that some $2 \to 3$ processes, namely photon bremsstrahlung process ($q\bar{q} \to q\bar{q}\gamma$, $qg \to qg\gamma$) and inelastic pair annihilation process ($qq\bar{q} \to q\gamma$, $gq\bar{q} \to g\gamma$) as shown in Fig. 3.3, generate the same order contribution

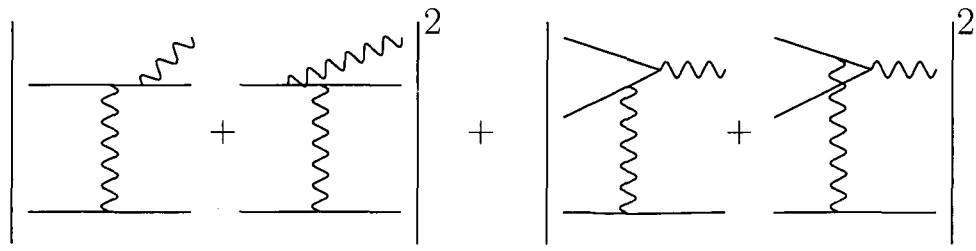

Figure 3.3: $2 \to 3$ particle processes (bremsstrahlung and inelastic pair annihilation) that also contribute to the leading order photon production rate.

as $2 \to 2$ processes to the emission of photons from the quark-gluon plasma. As for $2 \to 3$ processes, if the exchange gluon momentum q is hard $\sim T$, then the rates are $\mathcal{O}(\alpha_e \alpha_s^2)$, negligible compared to $2 \to 2$ processes, whose rate are $\mathcal{O}(\alpha_e \alpha_s)$. But if the exchange gluon momentum is soft $\sim g_s T$, an enhancement from the soft gluon propagator $1/(g_s T)^2$ will cancel the extra power of g_s^2 from the extra vertices, making the contribution to the photon emission rate from these $2 \to 3$ processes the same order as $2 \to 2$ processes.

However, in order to obtain the correct leading order photon emission rate from the quark-gluon plasma, it is not sufficient to incorporate only those additional $2 \to 3$ processes as shown in Fig. 3.3. First, the mean free path (time) of hard jets between soft scatterings by thermal partons in the surrounding medium is given by

$$\lambda = \frac{1}{n\sigma} \sim \frac{1}{T^3(g_s^2/T^2)} \sim \frac{1}{g_s^2 T}. \tag{3.4}$$

Second, as the exchanged gluon momentum is soft, from energy and momentum conservation, the corresponding internal quark line are nearly on-shell, which implies that the photon and the quark are highly collinear. As the scattering angle is small, it will take some time for the photon and the quark to be apart in space. This is the formation time of the collinear photon emission. In fact, the energies of internal quark lines are off-shell by an amount of

$$\delta E \sim \frac{k_\perp^2}{k} \sim \frac{(g_s T)^2}{T} \sim g_s^2 T, \tag{3.5}$$

from which we may obtain the time duration of this process,

$$t_{\text{form}} \sim \frac{1}{\delta E} \sim \frac{k}{k_\perp^2} \sim \frac{T}{(g_s T)^2} \sim \frac{1}{g_s^2 T}. \tag{3.6}$$

We may see that the photon emission time is the same order as the mean free time between soft scatterings by the surrounding partons from the medium. This implies that the quark has the potential to suffer more than one soft scattering with thermal medium particles before emitting the hard collinear photon. As a consequence, the multiple scattering processes cannot be treated independently; the interference of all those scatterings, such as $3 \to 4$ processes, $4 \to 5$ processes, or more, have to be taken into account consistently in order to obtain a complete calculation of leading order photon emission rates. This is known as Landau-Pomeranchuk-Migdal (LPM) effect [87].

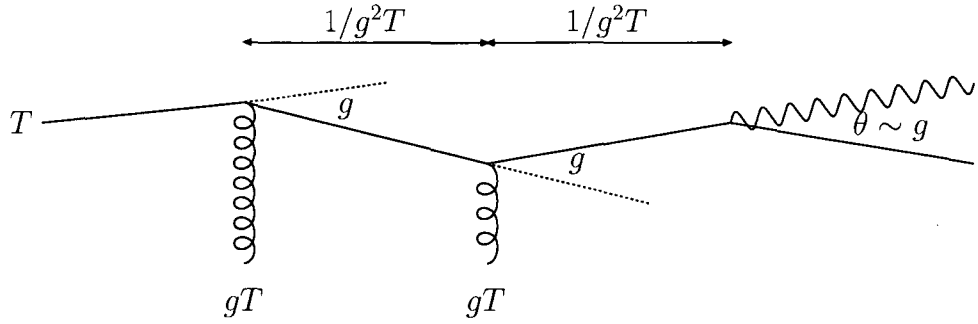

Figure 3.4: The typical orders of magnitude of various momentum, length and angular scales associated with a photon bremsstrahlung.

In Fig. 3.4, we show the typical orders of magnitude for various momentum, length and angular scales when a hard photon (with momentum $k \sim T$) is emitted by a hard partonic jet (with momentum $p \sim T$) propagating through the dynamical medium. The hard parton suffers more than one soft scatterings (with momentum transfer $q \sim g_s T$) before emitting the photon. The angle deflection in each collision is $\theta \sim q/p \sim g_s$. It is noted that scattering off ultra-soft gauge bosons (with momentum $q \sim g_s^2 T$) is not important, as the momentum exchanged is too small to affect the kinematics of the photon emission process.

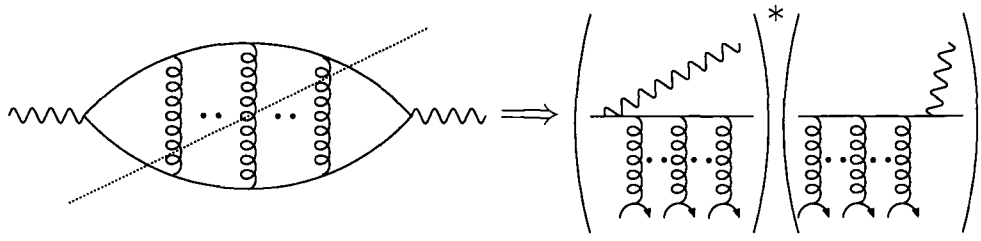

Figure 3.5: Cutting the ladder diagram may be interpreted as the interference between two diagrams with photon emission before and after the soft scatterings.

From Eq. (2.31), the photon production rate is related to the imaginary part of the photon self-energy, called ladder diagram. This corresponds to considering its cuts. It has been shown in Ref. [93, 94, 95] that a correct treatment of collinear bremsstrahlung and inelastic pair annihilation processes requires a summation of all ladder diagrams of the type shown in Fig. 3.5, each with a different number of gluon rungs (see Fig. 3.6). As indicated in Fig. 3.5, cutting the ladder diagram leads directly to bremsstrahlung and inelastic annihilation processes with LPM effects. Considering bremsstrahlung for example, this corresponds to the interference between two diagrams with photon emission before and after the soft scatterings. As all the exchanged gluons are soft (with momentum of order g_sT), the hard thermal loop (HTL) corrections [125] must be employed to the soft gluon propagators. As the resulting sum is just a geometric series, AMY [93, 94, 95] have written the total self-energy in terms of a linear integral equation, as illustrated in Fig. 3.6.

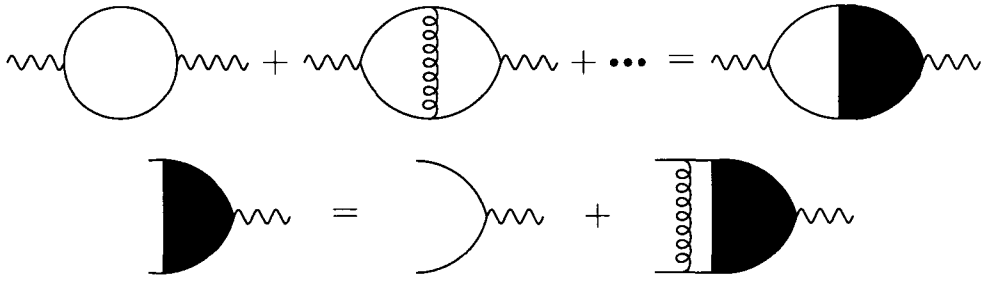

Figure 3.6: The sum of the geometric series of photon self-energy may be written in terms of the solution to a linear integral equation.

After performing the numerical computation of the integral equation, the leading order photon emission rate from bremsstrahlung and inelastic annihilation processes with LPM effect may be written as [93, 94, 95]

$$\frac{(2\pi)^3 dR_\gamma^{\rm LPM}}{d^3k} = \sum_f \left(\frac{e_f}{e}\right)^2 \frac{8\pi\alpha_e\alpha_s T^2}{k} f_F(k) C_{\rm LPM}(k/T), \tag{3.7}$$

where the numerical values of $C_{\rm LPM}(x)$ may be reproduced quite accurately by the following parametrization [93, 94, 95],

$$C_{\rm LPM}(x) \approx \sqrt{1+\frac{N_f}{6}}\left[\frac{0.548\ln(12.28+1/x)}{x^{3/2}} + \frac{0.133x}{\sqrt{1+x/16.27}}\right]. \tag{3.8}$$

For details of how to derive the above formula, please refer to Ref. [93, 94, 95]. Finally, putting all necessary ingredients together, we obtain the complete leading order result for photon emission rates from the quark-gluon plasma at $\mathcal{O}(\alpha_e\alpha_s)$ [93, 94, 95],

$$\frac{(2\pi)^3 dR_\gamma}{d^3k} = \sum_f \left(\frac{e_f}{e}\right)^2 \frac{8\pi\alpha_e\alpha_s T^2}{k} f_F(k)\left[\frac{1}{2}\ln\frac{kT}{m_q^2} + C_{2\to2}(k/T) + C_{\rm LPM}(k/T)\right] \tag{3.9}$$

where $C_{2\to2}(x)$ and $C_{\rm LPM}(x)$ are approximated by Eq. (3.3) and Eq. (3.8), respectively.

3.2 Gluon emission by bremsstrahlung from QGP

The above analysis of LPM effect for photon emission can be analogously extended to the evaluation of gluon emission by bremsstrahlung process in the quark-gluon plasma. The key complication here is that gluons also carry color charges. Thus, the emitted gluon will interact with the soft color background field, as shown in Fig. 3.7.

In spite of this difference, much of the argument for photon emission still holds for gluon emission, i.e., the emitted gluon and the incoming quark are nearly collinear. As we are considering hard gluon emission, we may treat the emitted gluon as another incoming particle propagating through the soft color background field. As a result, it is still possible to convert the resummation of infinite ladder diagrams into a similar integral equation. Analogous to photon emission, we may obtain the induced gluon emission rate $dR_g^{\rm LPM}(k)/d^3k$ (see Ref. [93, 94, 95] for details).

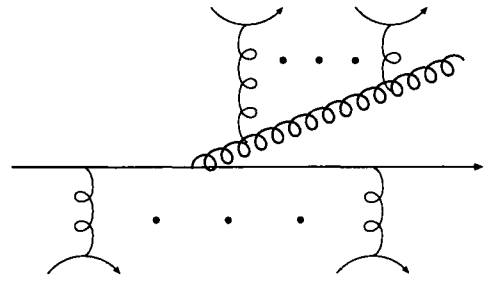

Figure 3.7: A typical gluon bremsstrahlung diagram that needs to be resummed in the AMY formalism.

In order to obtain the time evolution of the jet distribution, we need to extract the transition rate $d\Gamma^j_{ab}(p,k)/dkdt$ for the partonic process $j \to a+b$. For example, the gluon emission rate from the process $q \to qg$ may be written in terms of transition rate as,

$$\frac{(2\pi)^3 dR_g(k)}{d^3k} = \frac{(2\pi)^3 dN_g(k)}{d^3k d^3x dt} = \int \frac{d^3p}{(2\pi)^3} \frac{(2\pi)^3 dN_q(p)}{d^3p d^3x} \frac{(2\pi)^3 d\Gamma^q_{qg}(p,k)}{d^3k dt}$$
$$= \int dp \frac{p^2}{k^2} d_q f_q(p) \frac{d\Gamma^q_{qg}(p,k)}{dkdt}, \tag{3.10}$$

where $f_q(p) = (2\pi)^3/d_q \cdot dN_q(p)/d^3pd^3x = f_F(p)$ is the phase space distribution of the quark in the medium (Fermi-Dirac thermal distribution function) and $d_q = 2 \cdot 3 = 6$ is its spin-color degeneracy. Finally, the complete result for the gluon bremsstrahlung rate is [131, 132]

$$\frac{d\Gamma(p,k)}{dkdt} = \frac{C_s g_s^2}{16\pi p^7} \frac{1}{1 \pm e^{-k/T}} \frac{1}{1 \pm e^{-(p-k)/T}}$$
$$\times \left\{ \begin{array}{ll} \frac{1+(1-x)^2}{x^3(1-x)^2} & q \to qg \\ N_{\rm f} \frac{x^2+(1-x)^2}{x^2(1-x)^2} & g \to q\bar{q} \\ \frac{1+x^4+(1-x)^4}{x^3(1-x)^3} & g \to gg \end{array} \right\} \times \int \frac{d^2\vec{h}}{(2\pi)^2} 2\vec{h} \cdot \mathrm{Re}\, \vec{F}(\vec{h},p,k)\,. \tag{3.11}$$

Here $x \equiv k/p$ is the momentum fraction of the gluon (or the quark, for the case $g \to q\bar{q}$). The factors $1/[1 \pm \exp(k/T)]$ are Bose enhancement or Pauli blocking factors for the final states, with $-$ for bosons and $+$ for fermions. $\vec{h} \equiv \vec{p} \times \vec{k}$ determines how non-collinear the final state is; it is treated as parametrically $O(g_s T^2)$ and therefore small compared to $\vec{p} \cdot \vec{k}$. Therefore it can be taken as a two-dimensional vector

in transverse momentum space. $\vec{F}(\vec{h},p,k)$ is the solution of the following integral equation [131, 132]:

$$2\vec{h}=i\delta E(\vec{h},p,k)\vec{F}(\vec{h})+g_s^2\int\frac{d^2\vec{q}_\perp}{(2\pi)^2}C(\vec{q}_\perp)\{(C_s-C_{\rm A}/2)[\vec{F}(\vec{h})-\vec{F}(\vec{h}-k\,\vec{q}_\perp)] \\ +(C_{\rm A}/2)[\vec{F}(\vec{h})-\vec{F}(\vec{h}+p\,\vec{q}_\perp)]+(C_{\rm A}/2)[\vec{F}(\vec{h})-\vec{F}(\vec{h}-(p-k)\,\vec{q}_\perp)]\}\,. \quad (3.12)$$

Here $\delta E(\vec{h},p,k)$ is the energy difference between the final and the initial states:

$$\delta E(\vec{h},p,k)=\frac{\vec{h}^2}{2pk(p-k)}+\frac{m_k^2}{2k}+\frac{m_{p-k}^2}{2(p-k)}-\frac{m_p^2}{2p}\,, \quad (3.13)$$

and m^2 are the medium induced thermal masses. Also, $C(\vec{q}_\perp)$ is the differential rate to exchange transverse (to the parton) momentum $\vec{q}_\perp$. In a hot thermal medium, its value at leading order in $\alpha_{\rm s}$ is [134]

$$C(\vec{q}_\perp)=\frac{m_D^2}{\vec{q}_\perp^2(\vec{q}_\perp^2+m_D^2)}\,,\quad m_D^2=\frac{g_s^2T^2}{6}(2N_{\rm c}+N_{\rm f})\,. \quad (3.14)$$

For the case of $g\to q\bar{q}$, $(C_s-C_{\rm A}/2)$ should appear as the prefactor on the term containing $\vec{F}(\vec{h}-p\,\vec{q}_\perp)$ rather than $\vec{F}(\vec{h}-k\,\vec{q}_\perp)$.

3.3 Application of AMY to radiative jet energy loss

It has been shown in Fig. 3.7 that when a hard partonic jet traverses through a quark gluon plasma, it will interact with the colored medium by exchanging soft momentum $\sim g_sT$ with the constituent particles. Those soft multiple scatterings will induce the radiation of a gluon by bremsstrahlung, leading to the energy loss of the propagating hard parton. This energy loss mechanism is commonly referred to as radiative jet energy loss. In this section, we present some simple applications of the AMY formalism to the radiative part of jet energy loss in a hot and dense medium.

The expressions of transition rates in Eq. (3.11) are used to evaluate the time evolution of the hard quark plus anti-quark distribution $P_q(p,t)=dN_q(p,t)/dp$ and the hard gluon distribution $P_g(p,t)=dN_g(p,t)/dp$, as they traverse the soft color medium. The joint evolution equations for $P_q(p,t)$ and $P_g(p,t)$ are given by [131, 132]:

$$\frac{dP_q(p)}{dt}=\int_k P_q(p+k)\frac{d\Gamma_{qg}^q(p+k,k)}{dkdt}-P_q(p)\frac{d\Gamma_{qg}^q(p,k)}{dkdt}+2P_g(p+k)\frac{d\Gamma_{q\bar{q}}^g(p+k,k)}{dkdt}\,,$$

$$\frac{dP_g(p)}{dt} = \int_k P_q(p+k)\frac{d\Gamma^q_{qg}(p+k,p)}{dkdt} + P_g(p+k)\frac{d\Gamma^g_{gg}(p+k,k)}{dkdt} - P_g(p)\left(\frac{d\Gamma^g_{q\bar{q}}(p,k)}{dkdt} + \frac{d\Gamma^g_{gg}(p,k)}{dkdt}\Theta(2k-p)\right), \tag{3.15}$$

where the k integrals run from $-\infty$ to ∞. The integration range with $k < 0$ represents absorption of thermal gluons from the QGP; the range with $k > p$ represents annihilation against an anti-quark from the QGP, of energy $(k-p)$. In writing Eq. (3.15), we used $d\Gamma^g_{gg}(p,k) = d\Gamma^g_{gg}(p,p-k)$ and similarly for $g \to qq$; the Θ function in the loss term for $g \to gg$ prevents double counting of final states.

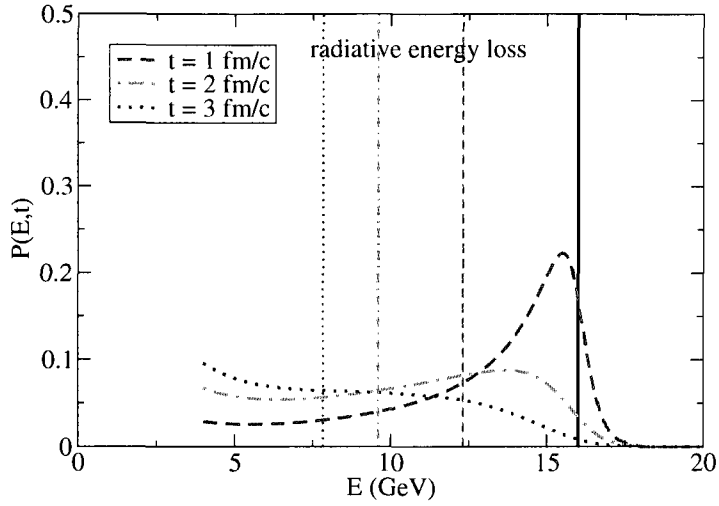

Figure 3.8: The evolution of a quark jet with initial energy $E_i = 16$ GeV propagating through a medium of temperature $T = 400$ MeV, where the vertical lines represent the values of mean energies related to the corresponding distributions.

As the first simple application to jet energy loss, we follow Ref. [131] and study the time evolution of a single hard particle traversing a quark-gluon plasma. In Fig. 3.8, the time evolution of the quark momentum distribution is plotted as a function of the quark energy for several different times. In the plot, The quark has the initial energy $E_i = 16$ GeV, and the medium has a constant temperature $T = 400$ MeV. Here the strong coupling constant α_s is set to be a constant $\alpha_s = 1/3$. With the above setting, the result of Fig. 1 in Ref. [131] is reproduced. The vertical lines in the plot represent the values of mean energies of the quarks, as evaluated by the first

moment of the corresponding quark momentum spectra. We may see that the final quark distributions are not centered at the mean energies, and become broader as the energy loss grows.

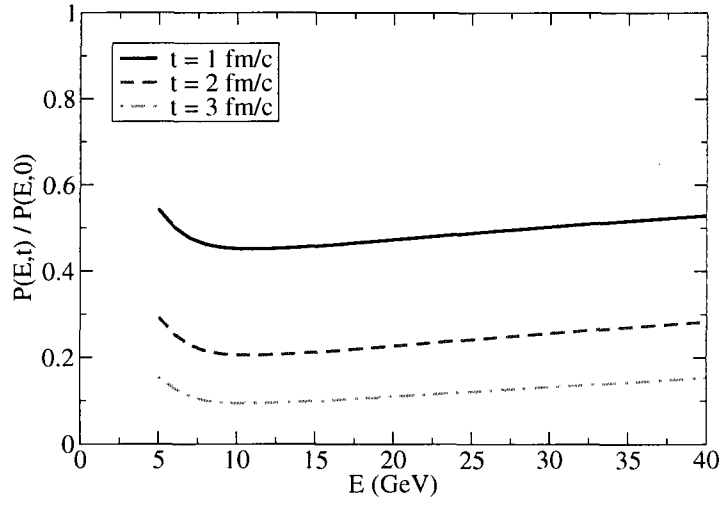

Figure 3.9: The ratios of the final and initial momentum spectra for quarks plus anti-quarks, after propagating through a medium of temperature $T = 400$ MeV.

To have a more realistic evolution of jet momentum spectra in the thermal medium, we evolve the jets with the following power-law parametrization for initial p_T spectra of quarks and anti-quarks, taken from [114]

$$\left.\frac{dN}{d^2p_T dy}\right|_{y=0} = K\frac{a}{(1+p_T/b)^c}, \tag{3.16}$$

where $a = 500$, $b = 1.6$ and $c = 7.9$ for quarks, and $a = 130$, $b = 1.9$ and $c = 8.9$ for anti-quarks. K is a constant to account for the next-leading-order corrections to the leading order result as inferred from perturbative QCD calculation.

The time evolution of quarks plus anti-quarks with above pow-law distributions is shown in Fig. 3.9, where the ratio of the final momentum spectrum to the initial momentum spectrum is plotted as a function of quark energy for several different times. The suppression of the jet momentum distribution is clearly observed as they traverse through the thermal medium. As for a plasma with temperature $T = 400$ MeV, we already observe approximately $4 - 5$ times suppression for quark jets when the size

of the medium is 2 fm/c. This size might be too small compared to the medium achieved at RHIC, but 400 MeV is probably the highest temperature being created at RHIC. In order to have a more accurate calculation of jet quenching at RHIC, a realistic hydrodynamical model is required to describe the space-time evolution of the created medium. This will be addressed in later chapters.

3.4 Discussions

In this section, we present some discussion of the applicability of the AMY formalism following Ref. [131, 132]. There have been several other theoretical models to describe the radiative energy loss by induced gluon bremsstrahlung, i.e., Baier-Dokshitzer-Mueller-Peigne-Schiff (BDMPS) [88], Gyulassy-Levai-Vitev (GLV) [89], Kovner-Wiedemann (KW) [90], Zakharov [91] and Majumder-Wang-Wang (Higher Twist) [92]. AMY formalism differs from other approaches in several different ways [132]. First, as was mentioned at the beginning of this chapter, the model treats QGP as a relativistic dynamical medium; the constituent particles of the medium are dynamic. The calculation of gluon emission rate is completely thermal; it is performed in the framework of finite temperature field theory, and temperature enters through the thermal phase space of the initial and final particles. Second, the model incorporates both energy loss processes and energy gain processes, such as the absorption of thermal partons and quark-anti-quark pair annihilation and creation. Third, the model explicitly solves for both the transition rates and the coupled rate equations for hard quarks plus anti-quarks and gluons.

In this work, the transition rates in the momentum space are calculated in the thermodynamic limit, which implies that the high energy parton experiences a uniform medium in the time scale of the gluon emission. However, the medium created in relativistic heavy ion collisions has a finite size, which will impose some limits on our formalism. This limitation is related to the coherence length of induced gluon radiation.

There are three typical length scales associated with the gluon bremsstrahlung

in relativistic heavy ion collisions: the mean free path λ for soft scatterings, the coherence length $l_{\rm coh}$ for induced radiation and the size L of the medium created in the collisions. The coherence length $l_{\rm coh}$ plays an important role in the consideration of the coherence pattern of induced gluon emission.

Now we consider a gluon with energy ω emitted by a hard partonic jet after suffering $N_{\rm coh}$ coherent soft scatterings. If we assume that the multiple soft scattering can be described by a random walk, with a momentum kick $k_\perp \sim \mu \sim g_s T$ from a single soft scattering, then the total transverse momentum squared $\mu^2_{\rm coh}$ accumulated by the hard jet after $N_{\rm coh}$ coherent scatterings is given by

$$\mu^2_{\rm coh} = N_{\rm coh}\mu^2. \tag{3.17}$$

Moreover, The distance travelled by the hard jet is given by

$$l_{\rm coh} = N_{\rm coh}\lambda \tag{3.18}$$

This is also the formation time (length) of the hard collinear gluon radiation,

$$l_{\rm coh} = t_{\rm form} = \frac{\omega}{\mu^2_{\rm coh}}. \tag{3.19}$$

Therefore, one may obtain the expression of the coherence length as [135],

$$l_{\rm coh} = \sqrt{\frac{\lambda\omega}{\mu^2}}. \tag{3.20}$$

When $l_{\rm coh} \ll \lambda$, the multiple scatterings are incoherent, and we may treat them as independent scatterings. This is the Bethe-Heitler regime, where the energy loss per unit length is proportional to the incoming energy [135],

$$\omega\frac{d\Gamma}{d\omega dz} = \frac{\alpha_s}{\pi}N_c\frac{1}{\lambda}. \tag{3.21}$$

When $\lambda \ll l_{\rm coh} \ll L$, the multiple scatterings are coherent. This is the LPM regime, where the energy loss per unit length is proportional to the square-root of the incoming energy [135],

$$\omega\frac{d\Gamma}{d\omega dz} = \frac{\alpha_s}{\pi}N_c\frac{1}{l_{\rm coh}} = \frac{\alpha_s}{\pi}N_c\sqrt{\frac{\mu^2}{\lambda\omega}}. \tag{3.22}$$

When the coherence length exceeds the length of the medium $l_{\rm coh} \gg L$, effectively there is only a single scattering. In this case, we are back to Beth-Heilter limit [132],

$$\omega \frac{d\Gamma}{d\omega dz} = \frac{\alpha_s}{\pi} N_c \frac{1}{L}. \tag{3.23}$$

Equivalently, we may introduce two energy scales: the LPM scale $E_{\rm LPM}$ and factorization scale $E_{\rm fact}$ defined as,

$$E_{\rm LPM} = \lambda \mu^2, \quad E_{\rm fact} = E_{\rm LPM} \left(\frac{L}{\lambda}\right)^2 = \frac{\mu^2 L^2}{\lambda}. \tag{3.24}$$

When the emitted energy ω is in the range $\omega < E_{\rm LPM}$, one is in incoherent Beith-Heilter regime. When the emitted energy ω is in the range $E_{\rm LPM} < \omega < \min[E_i, E_{\rm fact}]$, one is in coherent LPM regime. As the emitted energy ω exceed the factorization energy scale, $\omega > E_{\rm fact}$, effectively there is only a single scattering.

In our formalism, it is assumed that the high energy parton experiences a uniform medium on the time scale of the gluon emission, $l_{\rm coh} < L$. This requires that the energy of incoming parton is limited to be smaller than the factorization energy scale, $E_i < E_{\rm fact}$. As for Au+Au collisions at RHIC energies, setting $L \sim 5$ fm, $\mu \sim 0.5$ GeV and $\lambda \sim 1$ fm, we obtain the applicability of AMY formalism: $E_i < 30$ GeV. This is essentially within the momentum acceptance of the four RHIC detectors. As for Pb+Pb collisions at the LHC, setting $L \sim 5$ fm, $\mu \sim 1$ GeV and $\lambda \sim 0.5$ fm, we obtain $E_i < 250$ GeV.

4

Radiative jet energy loss in a 3D hydrodynamical medium

This chapter follows our recent work [106, 136], where the formalism [93, 94, 95] described in Chapter 3 is employed to study the radiative jet energy loss by induced gluon emission in relativistic heavy ion collisions. First, we present our calculation of the nuclear modification factor R_{AA} for π^0 production at high transverse momenta p_T in Au+Au collisions at $\sqrt{s_{NN}} = 200$ GeV at RHIC [106] by applying relativistic ideal three-dimensional hydrodynamics [137] to describe the thermalized medium produced in those collisions. We provide a systematic analysis of the azimuthal asymmetry of π^0 suppression at high p_T in central and non-central collisions, at mid and forward rapidity. Then, a calculation of the charged hadron R_{AA} is presented as a function of p_T for central Pb+Pb collisions at $\sqrt{s_{NN}} = 5.5$ TeV at mid-rapidity at the LHC [136], where ideal two-dimensional hydrodynamical model [138] is employed to describe the soft thermalized medium.

4.1 Introduction

In Chapter 3, we have presented the basic ingredients of our formalism, and some simple applications to the radiative part of jet energy loss in a quark-gluon plasma. In this chapter, we will perform a more sophisticated calculation of jet quenching at RHIC by employing relativistic three-dimensional hydrodynamical to model the space-time evolution of the thermalized medium produced in those collisions.

As has been mentioned earlier, significant jet quenching has been discovered at high p_T in central Au+Au collisions at RHIC. Experimentally, jet quenching can be quantified by measurements of various quantities, such as the nuclear modification

factor R_{AA} in central collisions as well as non-central collisions [139]. Additional tomographic observables are high p_T triggered correlation measurements, see e.g. [140, 141, 142, 143]. In this and next chapter, we will focus on the nuclear suppression of single particle spectra, and two particle correlations will be addressed in Chapter 6, where we present our study on the energy loss of photon-tagged jets at RHIC.

There have been considerable theoretical effort developed to improve our understanding of jet-quenching in the nuclear medium [144, 145, 146]. However, early calculations often relied on an elementary description of the soft medium, which varies with time unconstrained by the bulk observables. Recently, a 3D hydrodynamical evolution calculation [137] of the expanding medium in central and non-central collisions was employed in detailed studies of jet energy loss as predicted in the BDMPS formalism [147, 148] and in the higher twist formalism [149]. In this effort, we apply the tools described in Chapter 3 to the energy loss of the hard partons induced by gluon bremsstrahlung in the thermal partonic medium in central and non-central collision as inferred from 3D relativistic hydrodynamics [137]. The incorporation of the collisional energy loss will be done in Chapter 5. Note that in our approach, we only considers the energy loss in the thermalized partonic phase, and the energy loss in the confined hadronic sector is excluded in the present study, as essentially no jet-quenching has been observed in d+Au collisions [85]. Here we present a calculation of R_{AA} as a function of transverse momentum (and the azimuth) in central and non-central collisions and also study the rapidity dependence of this quantity.

4.2 Relativistic 3D hydrodynamical medium

In this section, we briefly review the relativistic ideal three-dimensional hydrodynamical model [137], which will be applied to describe the space-time evolution of the hot QCD matter being created in Au+Au collisions at RHIC.

The behavior related to the bulk properties of the high energy density phase in heavy-ion collisions at RHIC is well described by Relativistic Fluid Dynamics (RFD, see e.g. [44, 45, 46]). It should be noted that this description is not applicable in the

late dilute stages of the collisions as the mean free path of hadrons is large than the typical length scales of the system. Here in the calculation of the ultra-relativistic regime of heavy collisions at RHIC, we utilize the coordinates (τ, x, y, η) with the longitudinal proper time $\tau = \sqrt{t^2 - z^2}$ and space-time rapidity $\eta = \frac{1}{2}\ln[(t+z)/(t-z)]$.

We have already seen, in Chapter 1, the evolution of the system is controlled by the relativistic hydrodynamical equations,

$$\partial_\mu T^{\mu\nu}(x) = 0,\ \partial_\mu j_B^\mu(x) = 0. \tag{4.1}$$

For an ideal fluid, the energy momentum tensor $T^{\mu\nu}(x)$ and the baryon density current $j_B^\mu(x)$ can be expressed as

$$T^{\mu\nu}(x) = (\epsilon(x) + P(x))u^\mu(x)u^\nu(x) - P(x)g^{\mu\nu},\ j_B^\mu(x) = n_B(x)u^\mu(x). \tag{4.2}$$

To solve the above partial differential equations, an equation of state (EoS), $\epsilon = \epsilon(P)$, has to be specified. Here we use a simple equation of state with first order phase transition between QGP phase and hadron phase. Above the critical temperature ($T_c = 160$ MeV at $\mu = 0$), the medium is described by a bag model will massless u, d, s quarks and gluons [150, 151]. Below the critical temperature T_c, a hadron gas equation of state with corrections from excluded volumes [152] is employed.

The initial conditions have to be provided to solve the relativistic hydrodynamical equations. The information of the initial conditions can be extracted by comparing to the experimental data. Here, we assume early thermalization with subsequent hydrodynamical expansion at $\tau_i = 0.6$ fm/c. The initial energy density and baryon number density are parameterized by

$$\begin{aligned} \epsilon(x, y, \eta) &= \epsilon_{\max} W(x, y; b) H(\eta), \\ n_B(x, y, \eta) &= n_{B\max} W(x, y; b) H(\eta), \end{aligned} \tag{4.3}$$

where b and $\epsilon_{\max}$ ($n_{B\max}$) are the impact parameter and the maximum value of energy density (baryon number density), respectively. The transverse distribution $W(x, y; b)$ is parametrized by a combination of binary collision model and wounded nucleon

model [153],

$$W(x,y;b) = \omega \frac{d^2N_{\rm coll}}{d^2\vec{r}_\perp} + (1-\omega)\frac{d^2N_{\rm part}}{d^2\vec{r}_\perp}, \tag{4.4}$$

where ω is the weight factor for binary scaling. The binary scaling is characteristic of "hard" particle production processes, while the wounded nucleon scaling is characteristic of "soft" particle production processes. The longitudinal distribution $H(\eta)$ is parametrized by

$$H(\eta) = \exp\left[-(|\eta| - \eta_0)^2/(2\sigma_\eta^2)\cdot\theta(|\eta|-\eta_0)\right], \tag{4.5}$$

where η_0 and σ_η determine the plateau size and spreading of the longitudinal distribution. The initial conditions have been chosen such that a successful description of the soft physics at RHIC (elliptic flow, pseudo-rapidity distributions and low-p_T single particle spectra) is achieved. Below, we list the values of the parameters at $\tau_i = 0.6$fm/c used in the our calculation:

$$\epsilon_{\rm max} = 55\ {\rm GeV/fm^3},\ n_{B{\rm max}} = 0.15\ {\rm fm^{-3}},\ \omega = 0.6,\ \eta_0 = 0.5,\ \sigma_\eta = 1.5. \tag{4.6}$$

Once the EoS and the initial conditions at τ_i have been specified, the hydrodynamical evolution of the system is determined uniquely. This allows us to calculate the properties of the soft matter at RHIC, especially collective flow and particle spectra. The particle momentum spectra at freeze-out may be obtained by employing Cooper-Frye formula [53],

$$E\frac{dN}{d^3p} = \int_{\Sigma_f}\frac{g}{(2\pi)^3}d\sigma_\mu p^\mu f(x,p) = \int_{\Sigma_f}\frac{g}{(2\pi)^3}d\sigma_\mu p^\mu \frac{1}{\exp[(p_\nu u^\nu - \mu_f)/T_f]\pm 1}, \tag{4.7}$$

where $d\sigma_\mu$ is the normal vector to the freezeout hyper-surface Σ_f, p^μ is the particle momentum, f is the single particle phase space distribution function, and μ_f is chemical potential at freeze-out. Here, the freezeout process is assumed to happen when a temperature in a volume element of fluid is equal to a freezeout temperature $T_f = 110$ MeV. Also the freezout temperature T_f may be treated as a free parameter and determined by comparing to the experimental data on single particle spectra.

It should be mentioned that the 3D hydrodynamical model used in this thesis does not take into account the subsequent interactions among hadrons after freeze-out. Those interactions may be described by microscopic transport models, such as Ultra-relativistic Quantum Molecular Dynamics (UrQMD) [57, 58]. As for this case, the ensemble of hadrons produced at freezeout is used as the initial input for UrQMD calculation. For further details of the implementation of UrQMD calculation and its possible implications, we refer the reader to [137].

4.3 Jet evolution in the soft medium

In this section, we present the techniques employed to calculate the initial jet production in the early stage of the collisions, the subsequent propagation through the hot and dense medium, and final hadronization in the vacuum. As we focus on the hadrons in the high p_T region, fragmentation will be the dominant mechanisms for the production of hadrons. Other mechanisms such as the recombination of partons become of increasing significance for the production of softer hadrons (below $p_T \sim 7$ GeV/c) [154].

The momentum distribution of initial hard jets is computed from pQCD in the factorization formalism [113],

$$\frac{d\sigma^j_{AB}}{d^2p^j_T dy} = \sum_{abd} \int dx_a G_{a/A}(x_a, Q) G_{b/B}(x_b, Q) \frac{1}{\pi} \frac{2x_a x_b}{2x_a - x^j_T e^y} K \frac{d\sigma_{a+b\to j+d}}{dt}. \quad (4.8)$$

In the above equation, $G_{a/A}(x_a, Q)$ is the distribution function of parton a with momentum fraction x_a in the nucleus A at factorization scale Q, taken from CTEQ5 [155] including nuclear shadowing effects from EKS98 [156] [1]. The index j represents one of the partonic species ($j = q, \bar{q}, g$), and $x^j_T = 2p^j_T/\sqrt{s_{NN}}$, where $\sqrt{s_{NN}}$ is the center-of-mass energy for nucleon-nucleon collisions. The distribution $d\sigma/dt$ is the leading order QCD differential cross section, and the K-factor accounts for next-to-leading order (NLO) effects and is taken to be constant in our calculation as it is

[1] Unless otherwise stated, in the following discussions the use of CTEQ5 + EKS98 for nuclear parton distribution functions will be applied.

almost p_T independent [138, 157, 158]. The initial Cronin effect is neglected in our calculation since the nuclear modification factor of neutral pions from d+Au collisions is consistent with 1, within systematic errors [159].

The hadron production is obtained by introducing the hadron fragmentation function $D_{h/j}(z_j, Q_F)$, which gives the multiplicity of the hadron h with the momentum fraction $z_j = p_T/p_T^j$ produced from a jet j at a scale Q_F. For p+p collisions, as no medium is produced (thus no energy loss for the jets), the final hadron spectra are obtained by fragmenting the initial hard jet spectra,

$$\frac{d\sigma_{pp}^h}{d^2p_T dy} = \sum_j \int \frac{dz_j}{z_j^2} D_{h/j}(z_j, Q_F) \frac{d\sigma_{pp}^j}{d^2p_T^j dy}, \tag{4.9}$$

In our calculation, the fragmentation function is taken from the KKP parametrization [160]. The factorization scale $Q = p_T^j$ and fragmentation scale $Q_F = p_T$ are set as in [138] where the K-factor is found to be 2.8. These values nicely reproduce the experimentally measured π^0 yield at mid and forward rapidity in p+p collisions at $\sqrt{s_{NN}} = 200$ GeV, as shown in Fig. 4.1 and Fig. 4.2, where experimental data are taken from PHENIX [161] and STAR [162], respectively. It can be clearly seen that replacing the CTEQ5 parton distribution functions by MRST01 [163] yields essentially the same result for the inclusive π^0 production in p+p collisions. We point out that the presence of a nuclear medium in relativistic heavy ion collisions might in principle alter these scales but we postpone a detailed study of this possibility to future research.

As for the hadron production in Au+Au collisions at RHIC, we must include the energy loss of hard jets during their propagation through the thermalized medium produced in those collisions before fragmentation in vacuum. This is performed by taking into account the induced gluon emission during jets travelling. The jet energy loss depends on the path taken by the jet and the medium profile along that path, which in turn depends on the location of the production vertex $\vec{r}_\perp$ of the jet and its propagation angle ϕ with respect to the reaction plane. Therefore, we must convolve the jets over all origins $\vec{r}_\perp$ and directions ϕ.

The probability density distribution of initial jets $\mathcal{P}_{AB}(b, \vec{r}\perp)$ at the transverse

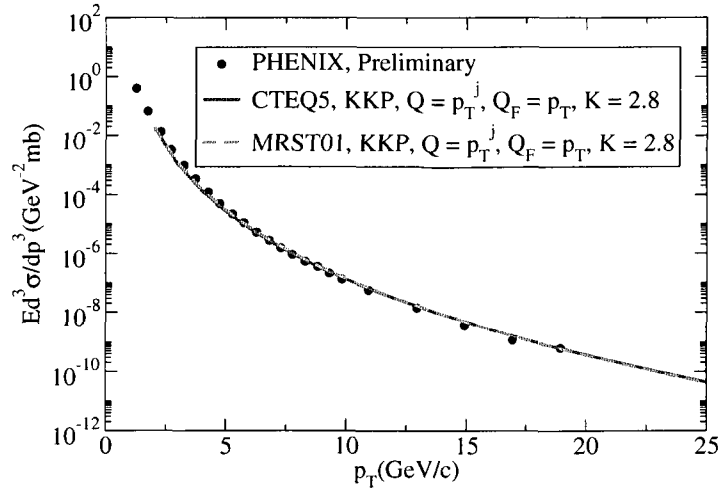

Figure 4.1: The inclusive cross section for π^0 production versus π^0 transverse momentum at mid-rapidity in pp collisions at $\sqrt{s_{NN}} = 200$ GeV, compared with PHENIX data.

position $\vec{r}_\perp$ in A+B collisions with impact parameter $\vec{b}$ is given by

$$\mathcal{P}_{AB}(b, \vec{r}_\perp) = \frac{T_A(\vec{r}_\perp + \vec{b}/2) T_B(\vec{r}_\perp - \vec{b}/2)}{T_{AB}(b)}. \tag{4.10}$$

Here we use a Woods-Saxon form, $\rho(\vec{r}_\perp, z) = \rho_0/[1 + \exp(\frac{r-R}{d})]$, for the nuclear density function to evaluate the nuclear thickness function $T_A(\vec{r}_\perp) = \int dz \rho_A(\vec{r}_\perp, z)$ and the overlap function of two nuclei $T_{AB}(b) = \int d^2 r_\perp T_A(\vec{r}_\perp) T_B(\vec{r}_\perp + \vec{b})$. The values of the parameters $R = 6.38$ fm and $d = 0.535$ fm are taken from [63].

We have already seen, in Chapter 3, the evolution of jet momentum distribution $P_j(p,t) = dN_j(p,t)/dp$ (essentially the probability of finding a jet with energy p at time t) in the medium is obtained by solving a set of coupled rate equations for quarks, anti-quarks and gluons, which have the following generic form,

$$\frac{dP_j(p,t)}{dt} = \sum_{ab} \int dk \left[P_a(p+k,t) \frac{d\Gamma^a_{jb}(p+k,k)}{dkdt} - P_j(p,t) \frac{d\Gamma^j_{ab}(p,k)}{dkdt} \right], \tag{4.11}$$

where $d\Gamma^j_{ab}(p,k)/dkdt$ is the transition rate for the partonic process $j \to a + b$. We point out that the calculation includes not only the emission but also the absorption of thermal partons as the k integral in Eq. (4.11) ranges from $-\infty$ to ∞.

The strength of the transition rate in pQCD is controlled by the strong coupling constant α_s, temperature T and the flow parameter $\vec{\beta}$ (the velocity of the thermal

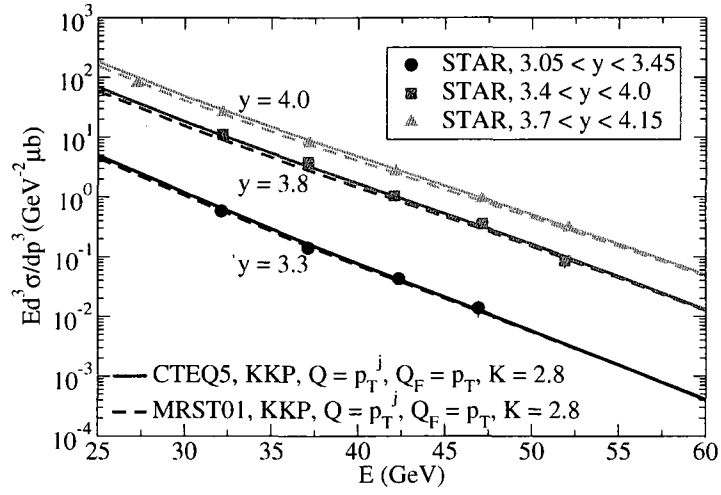

Figure 4.2: The inclusive cross section for π^0 production versus π^0 energy at forward rapidity in pp collisions at $\sqrt{s_{NN}} = 200$ GeV, compared with STAR data.

medium) relative to the jet's path. In a 3D expanding medium, the transition rate is first evaluated in the local frame of the thermal medium, then boosted into the laboratory frame,

$$\left.\frac{d\Gamma(p,k)}{dkdt}\right|_{\text{lab}} = (1-\vec{v}_j\cdot\vec{\beta})\left.\frac{d\Gamma(p_0,k_0)}{dk_0dt_0}\right|_{\text{local}}, \tag{4.12}$$

where $k_0 = k(1-\vec{v}_j\cdot\vec{\beta})/\sqrt{1-\beta^2}$ and $t_0 = t\sqrt{1-\beta^2}$ are momentum and the proper time in the local frame, and $\vec{v}_j$ is the velocity of the jet. As jets propagate in the medium, the temperature and the flow parameter depend on the time and the positions of jets, and the 3D hydrodynamical calculation [137] is utilized to determine the temperature and flow profiles. The energy-loss mechanism is applied at $\tau_0 = 0.6$ fm/c, when the medium reaches thermal equilibrium, and turned off when the medium reaches the hadronic phase.

The final hadron spectrum at high p_T in A+B collisions is obtained by the fragmentation of jets in the vacuum after their passing through the 3D expanding medium,

$$\frac{d\sigma^h_{AB}(b)}{d^2p_Tdy} = \frac{1}{2\pi}\int d^2\vec{r}_\perp \mathcal{P}_{AB}(b,\vec{r}_\perp)\sum_j\int\frac{dz_j}{z_j^2}D_{h/j}(z_j,Q_F)\left.\frac{d\sigma^j_{AB}(b,\vec{r}_\perp,\phi)}{d^2p_T^jdy}\right|_{\text{fin}}, \tag{4.13}$$

where $d\sigma^j_{AB}/d^2p_T^jdy|_{\text{fin}}$ is the final momentum distribution of the jet initially created at transverse position $\vec{r}_\perp$ and propagating at azimuthal angle ϕ. The yield of final

hadron production is given by,

$$\frac{dN^h_{AB}(b)}{d^2p_T dy} = \frac{N_{\rm coll}(b)}{\sigma_{NN}} \frac{d\sigma^h_{AB}(b)}{d^2p_T dy}. \tag{4.14}$$

The nuclear modification factor R_{AA} is defined as the ratio of the hadron yield in A+A collisions to that in p+p interactions scaled by the number of binary collisions

$$R_{AA}(b, \vec{p}_T, y) = \frac{\sigma_{NN}}{N_{\rm coll}(b)} \frac{dN^h_{AB}(b)/d^2p_T dy}{d\sigma^h_{pp}/d^2p_T dy} = \frac{d\sigma^h_{AA}(b)/d^2p_T dy}{d\sigma^h_{pp}/d^2p_T dy}. \tag{4.15}$$

4.4 Results

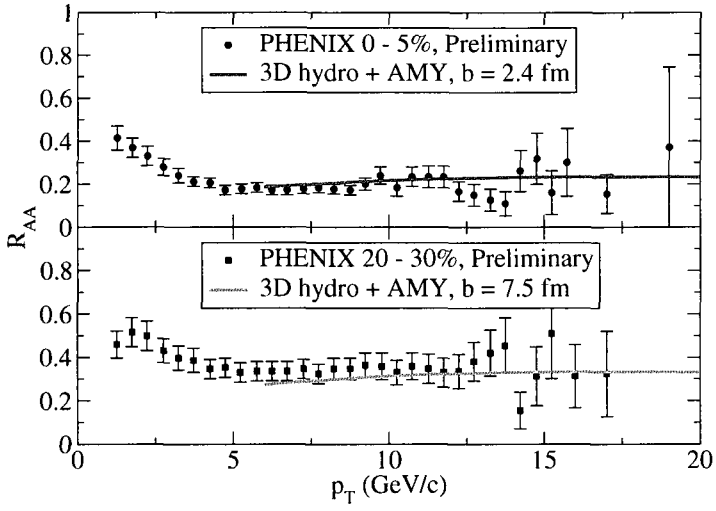

Figure 4.3: The neutral pion R_{AA} at midrapidity in most central (upper) and midperipheral (lower) Au+Au collisions at RHIC compared with PHENIX data.

In this section, we present the numerical results of our radiative jet energy loss study. Here we only show results for the nuclear modification factor R_{AA} for neutral pions, as results for charged hadrons (including contributions from charged pions, kaons and protons) are qualitatively similar. In Fig. 4.3, we present the calculation of the nuclear modification factor R_{AA} for neutral pions measured at midrapidity for two different impact parameters $b = 2.4$ fm and $b = 7.5$ fm, compared with (preliminary) PHENIX data for most central $(0 - 5\%)$ and midcentral $(20 - 30\%)$ collisions [139].

The strong coupling constant α_s is the only quantity which is not uniquely determined in the model once the medium evolution is fixed by the initial conditions and subsequent 3D hydrodynamical expansion. The value of α_s is a direct measure of the interaction strength and adjusted in such a way that the experimental data in the most central collisions is described. The same value, $\alpha_s = 0.33$, is used in peripheral collisions. Treating α_s as a constant from early thermalization on down to the phase transition temperature is a simplification and corresponds to the assumption that the deconfined phase of the medium formed in Au+Au collisions at $\sqrt{s_{NN}} = 200$ GeV at RHIC can be characterized by one average effective coupling. We have verified that choosing different constant values of α_s does not influence the shape of R_{AA} as a function of p_T significantly while only the overall normalization is affected.

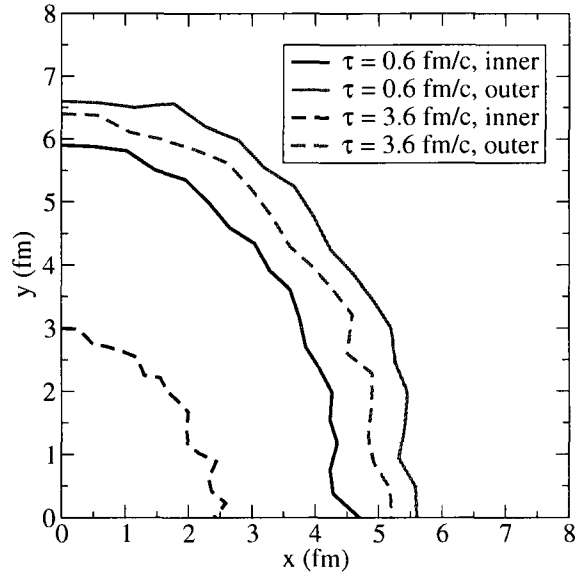

Figure 4.4: The inner and outer boundaries for $T = T_c$ in the transverse plane at two different proper times, $b = 7.5$ fm.

In Fig. 4.3, R_{AA} at midrapidity is averaged over the azimuth ϕ. However, R_{AA} in central collisions *alone* is not suited to distinguish in detail between different theoretical conjectures about jet energy loss [164]. More tomographic capabilities can be achieved if one studies R_{AA} at midrapidity in *non-central* collisions not only as a function of p_T averaged over ϕ but also as a function of the azimuth ϕ [139].

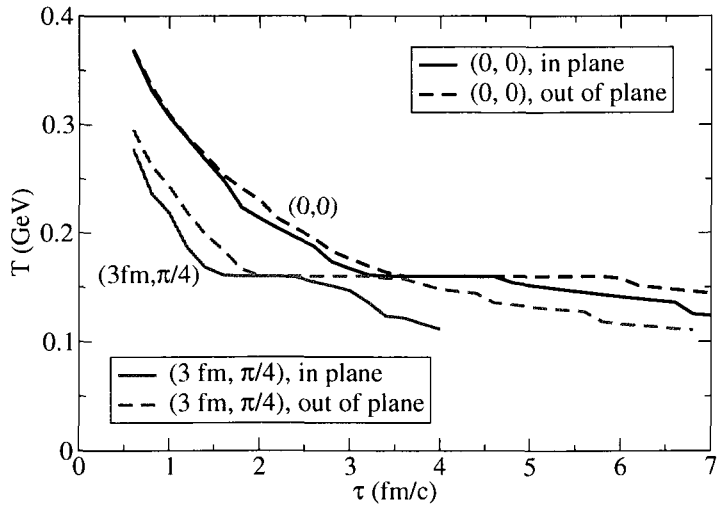

Figure 4.5: The time evolution of the temperature seen by a jet initially created at (r_0, ϕ_0) moving in plane and out of plane through the medium, $b = 7.5$ fm.

In non-central collisions, the initial geometric asymmetry for the reaction zone leaves its imprint on the subsequent 3D hydrodynamical evolution. As a result, initial jets experience different energy loss due to the different local properties of the nuclear medium with which they interact. The important input from the evolution is the temperature in the rest frame of the local fluid that the jet experiences (and to a lesser extent the flow profile of the medium, as discussed later).

To illustrate the geometrical asymmetry of the medium, we show in Fig. 4.4 isotherms for $T = T_c$ in the transverse plane for an impact parameter of $b = 7.5$ fm at two different proper times of the evolution. They represent the inner and outer boundaries of the mixed phase during the evolution. The geometric asymmetry of the temperature profile can be clearly seen from the plot. Both boundaries move towards the center and the inner boundary moves faster than the outer boundary. It is useful to define the emission in plane ($\phi = 0$) versus out of plane ($\phi = \pi/2$).

Fig. 4.5 shows the temperature observed by a jet traversing this medium. The jet is assumed to be created at position (r_0, ϕ_0) by a hard scattering at early times in the heavy-ion collision. As it propagates through the medium, the surrounding environment will change from the QGP phase to the mixed phase, then to the hadronic

phase and will eventually freeze-out. We plot the temperature evolution experienced by jets that are created in a symmetric position ($\phi_0 = \pi/4$) relative to in-plane and out-of-plane and illustrate the geometrical asymmetry of the medium experienced by the jet. We compare jets starting at the origin and those at $r_0 = 3$ fm.

As is clearly evident, jets that propagate out of plane pass the mixed phase and the hadronic phase at a later proper time than those traversing in plane and will interact with the deconfined and mixed phase of the medium longer. As a result, the energy loss experienced by the jets propagating out of plane will therefore be larger than in plane if they start from the same point and carry the same energy.

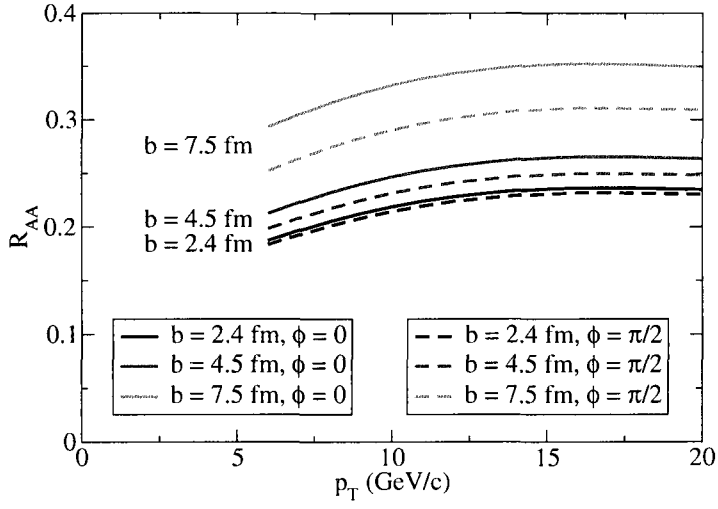

Figure 4.6: The neutral pion R_{AA} at midrapidity for emissions in plane and out of plane as a function of p_T for different impact parameters.

This behavior is reflected in Fig. 4.6, where R_{AA} is shown as a function of p_T for emissions in plane and out of plane for different impact parameters. While there is a very small difference for R_{AA} between the two planes in central collisions, a much larger difference for midcentral collisions ($\sim 13\%$ for $b = 7.5$ fm) is predicted, as can been seen from the ratio of R_{AA} out of plane to that in plane shown in Fig. 4.7.

As a further tomographic quantity, one can also study R_{AA} for non-central collisions as a function of the azimuthal angle ϕ for different p_T. In Fig. 4.8, we show the ratio of differential $R_{AA}(\phi)$ to the ϕ-averaged R_{AA} as a function of ϕ for three different

p_T. From the plot, we observe a monotonous decrease of R_{AA} for emissions from in plane to out of plane. This reflects (an average of) the asymmetric temperature (and flow) profiles experienced by the jets while they traverse the medium.

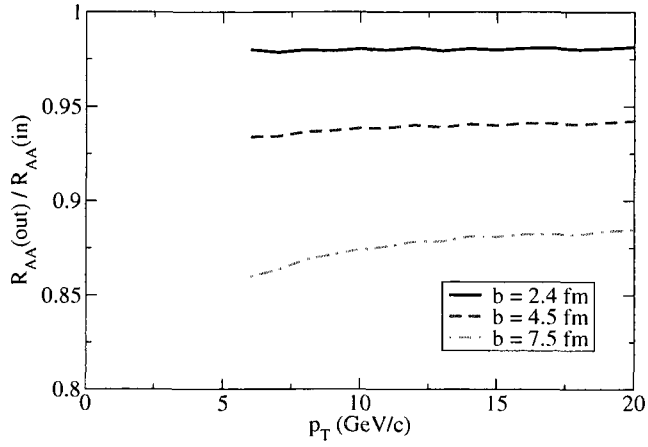

Figure 4.7: The ratio of the neutral pion R_{AA} at midrapidity for emissions in plane and out of plane as a function of p_T for different impact parameters.

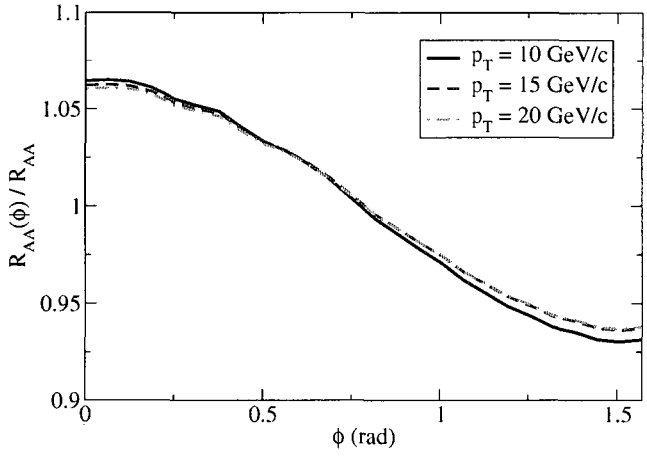

Figure 4.8: The neutral pion R_{AA} at midrapidity as a function of the azimuthal angle ϕ of the pion for different p_T, $b = 7.5$ fm.

The azimuthal anisotropy is often studied in terms of Fourier expansion of the particle spectrum $dN/d^2p_T dy$ as

$$\frac{dN}{p_T dp_T d\phi dy} = \frac{dN}{2\pi p_T dp_T dy}\left[1 + \sum_n 2v_n(p_T, y)\cos(n\phi)\right], \tag{4.16}$$

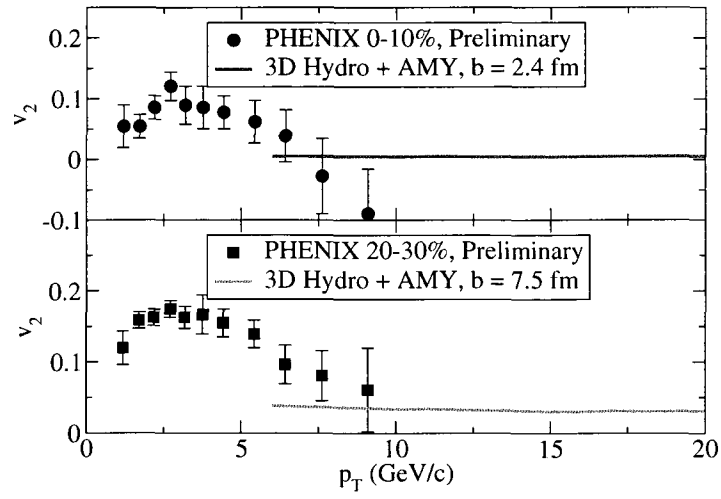

Figure 4.9: The neutral pion v_2 at midrapidity in most central (upper) and midperipheral (lower) Au+Au collisions at RHIC compared with PHENIX data.

where the coefficient v_n is given by

$$v_n(p_T, y) = \frac{\int_0^{2\pi} d\phi \cos(n\phi) dN/d^2p_T dy}{\int_0^{2\pi} d\phi dN/d^2p_T dy}. \tag{4.17}$$

It is evident that all odd coefficients vanish because of symmetry, leaving the coefficient v_2 to be the most important one.

In Fig. 4.9, the anisotropy parameter v_2 of π^0 production in Au+Au collisions at RHIC energies is shown as a function of p_T. Our calculation is compatible with available experimental data at high p_T. Our results imply that v_2 at high p_T is almost identically zero for most central collisions, as the medium is essentially symmetric with respect to the azimuthal angle. As for for mid-peripheral collisions ($b = 7.5$ fm), v_2 is positive (around 0.03) and has little dependence on hadron p_T. It should be noted that our calculation includes only fragmentation for the final hadron production, thus our result is only reliable at higher p_T regime. For the production of softer hadrons (below $p_T \sim 7$ GeV/c), other mechanisms, such as the recombination of partons, become of increasing significance [154].

In a 3D expanding medium, there is also considerable collective flow being built up during the evolution. This can affect the energy loss of jets and may to some degree influence the asymmetry in the final pion spectrum [165]. To quantify this effect, we

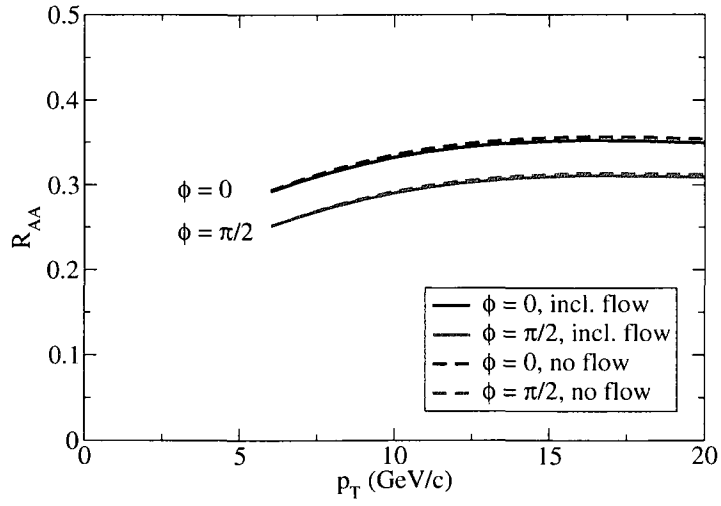

Figure 4.10: Comparing the neutral pion R_{AA} at midrapidity with and without flow for emissions in plane and out of plane as a function of p_T, $b = 7.5$ fm.

use the same 3D hydro temperature profile, but disregard the transverse flow. We compare the case with flow to one where the flow velocity is disregarded, namely $\vec{\beta} = 0$ is enforced by hand in Eq. (4.12) (only for illustration purposes). This treatment can give an estimate on how collective flow (not the temperature of the medium) influences the jet energy loss in the evolution. As is shown in Fig. 4.10, flow effects only slightly increase the quenching power of the medium in the calculation. It is emphasized that for a realistic hydrodynamical calculation, the overall temperature of the medium would not drop as fast if collective flow was switched off and the medium itself would expand more slowly in this case.

We may perform more differential analysis of jet quenching in a three dimensional dynamical evolving medium, i.e. the dependence of the nuclear suppression of jets on their initial production vertices $\vec{r}_\perp = (x, y)$ in the transverse plane. For example, one may cut the transverse plane into many small slices along x axis and study R_{AA} of the hadrons produced from the quenched jets originating in each of those slices. This corresponds to calculating the following quantity,

$$R_{AA}(x) = \frac{\int dy \mathcal{P}_{AA}(x,y) R_{AA}(x,y)}{\int dy \mathcal{P}_{AA}(x,y)}, \tag{4.18}$$

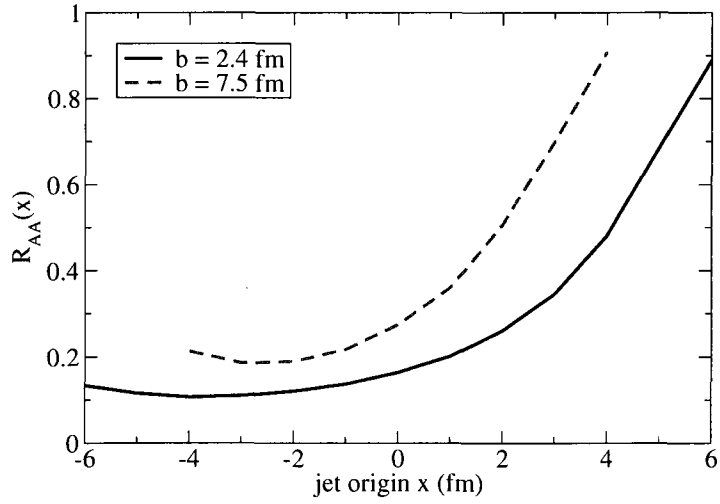

Figure 4.11: In-plane R_{AA} for neutral pions as a function of jet origin x in Au+Au collisions at RHIC. The momenta of pions are take to be 8 GeV/c $< p_T <$ 10 GeV/c.

where x is the mid-point of each slice (or we may perform the integration over x around the mid-point in both numerator and denominator). In Fig. 4.11, we show R_{AA} of neutral pions with transverse momenta 8 GeV/c $< p_T <$ 10 GeV/c originating from quenched jets moving in the positive x direction as a function of jet production vertices along the x-axis. It can be clearly seen in the plot that the quenching of jets has a strong dependence on the medium size traversed by jets before fragmentation. Furthermore, a small rise of R_{AA} is observed when jets are produced in the furthest slice. This is because the medium traversed by those jets has the smaller energy densities and temperatures compared to those jets produced in more central positions.

Another highly interesting question is where those quenched jets that produce the hadrons with a certain momentum p_T come from. This is equivallent to the question how big is the probability for the jets to survive and fragment into hadrons after traversing a certain depth of thermal medium. Mathematically, one may define a normalized probability density function $P(x, y)$ as follows,

$$P(x,y) = \frac{\mathcal{P}_{AA}(x,y)R_{AA}(x,y)}{\int dxdy\mathcal{P}_{AA}(x,y)R_{AA}(x,y)}, \tag{4.19}$$

where the position-dependent nuclear suppression factor $R_{AA}(x, y)$ is weighted with

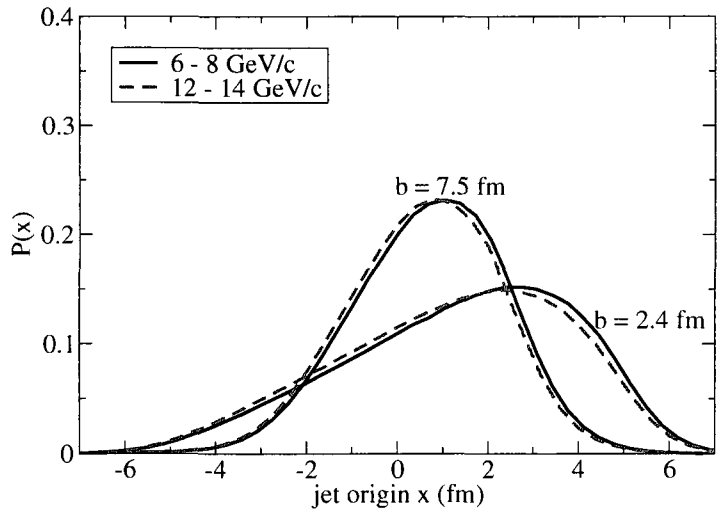

Figure 4.12: The probability distribution of initial jets in transverse plane to produce a hadron in plane with a transverse momentum p_T in Au+Au collisions at RHIC. The distribution has been projected onto x axis by integrating out the distribution in y direction.

the jet probability density function $P_{AA}(x, y)$. In fact, this is the conditional probability of finding a jet at the position (x, y) given that a hadron with a certain momentum p_T is observed. In Fig. 4.12, we show the probability function $P(x, y)$ projected onto x axis (y-integrated probability $P(x) = \int dy P(x, y)$). Again we look for neutral pions originating from quenched jets moving in the positive x direction. From the plot, we observe that in most central collisions ($b = 2.4$ fm), hadrons are more likely produced from those jets around $x = 3$ fm region, not in the center. This is due to the fact that the medium traversed by jets produced around the center has the largest energy density. As we move to more peripheral collisions, the energy loss by those jets become smaller. Consequently, the most probable region for jets to produce hadrons become closer to the center of the medium (around $x = 1$ fm for $b = 7.5$ fm).

4.5 Nuclear suppression of jets at forward rapidity

We point out that a further interesting quantity is R_{AA} as a function of p_T at forward rapidity. The formalism as outlined in the above sections can be straightforwardly extended to treat this case. Here we restrict ourselves to only moderate deviations

from midrapidity (maximum forward rapidity $y = 2$). One reason is that the nuclear parton distribution functions can be less exactly determined in the relevant region [156, 166]. On the other hand, the assumption of a thermalized medium essential for a hydrodynamical treatment is no longer fulfilled far away from midrapidity.

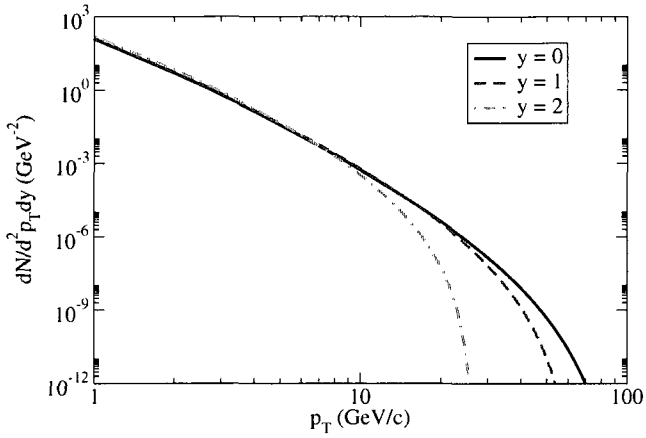

Figure 4.13: The jet (quark plus anti-quark) transverse momentum distribution at different rapidities, $b = 2.4$ fm.

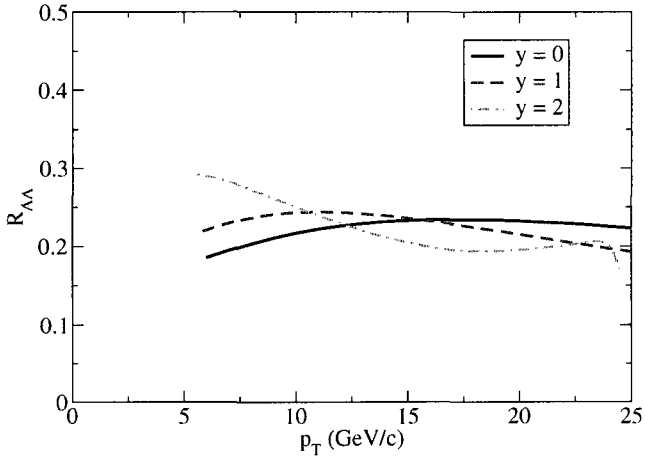

Figure 4.14: The neutral pion R_{AA} at different rapidities, $b = 2.4$ fm.

In Fig. 4.13, we show the initial jet distribution of quarks plus anti-quarks for different rapidities. Note that at finite rapidity, the energy of a highly-relativistic jet with a transverse momentum p_T is given by $E = p_T \cosh y$. Therefore, the kinematical

cut off at $E = \sqrt{s_{NN}}/2 = 100$ GeV is reached at lower p_T for finite y.

In Fig. 4.14 we show R_{AA} as a function of p_T for central collisions ($0 - 5\%$, $b = 2.4$ fm) at mid and forward rapidity. It is interesting to notice that R_{AA} behaves quite differently as a function of p_T at $y = 2$ than at $y = 0$. This is not only due to the different temperature profiles of the hydrodynamical medium at forward rapidity but also strongly influenced by the different initial jet distributions, see Fig. 4.13.

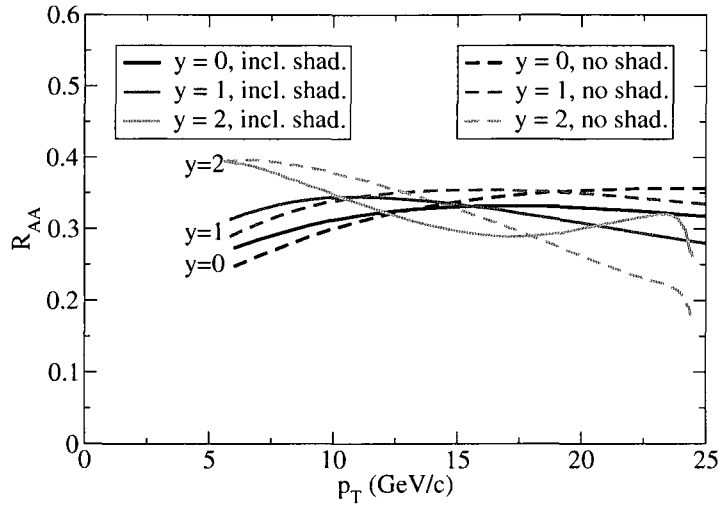

Figure 4.15: Comparing neutral pion R_{AA} with and without nuclear shadowing effect at different rapidities, $b = 7.5$ fm.

To provide additional insight, we studied the same quantity averaged over ϕ for midcentral collisions with an impact parameter of $b = 7.5$ fm with and without nuclear shadowing effects taken into account in the parton distribution functions utilized in Eq. (4.8). Results are shown in Fig. 4.15. It is interesting to notice that R_{AA} is not monotonously increasing as a function of p_T. The midrapidity R_{AA} is decreasing above ~ 18 GeV/c (with nuclear shadowing), the turning point for $y = 1$ is at ~ 9 GeV/c (with nuclear shadowing). The values of R_{AA} at $y = 2$ decreases monotonically above ~ 6 GeV/c in the case without nuclear shadowing and exhibits two turning points if shadowing is taken into account. We have also found that assuming a simple power law approximation for $dN/d^2p_T dy$ distributions for all values of p_T would lead to increased R_{AA} at higher p_T (comparison not shown). This demonstrates that the

overall decrease of R_{AA} at higher p_T is mainly due to the initial jet distribution according to Eq. (4.8) at high transverse momentum which decreases faster than an overall power law, see Fig. 4.13.

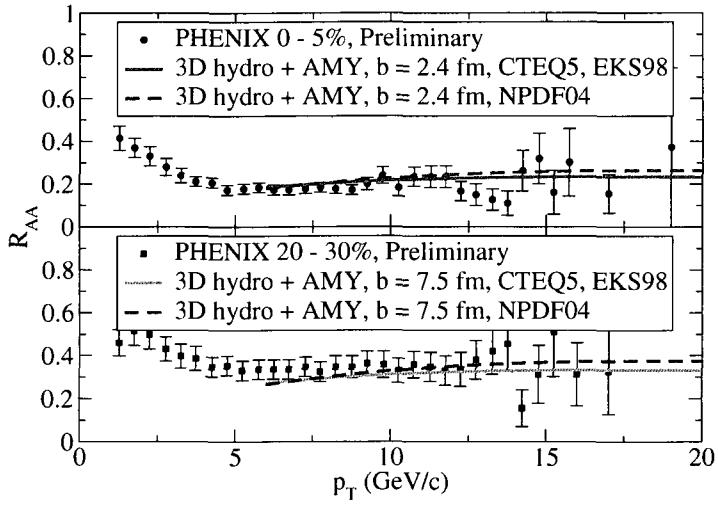

Figure 4.16: The neutral pion R_{AA} at midrapidity in most central (upper) and midperipheral (lower) Au+Au collisions at RHIC compared with PHENIX data. Different prescriptions of nuclear parton distribution functions are used for comparison.

The non-monotonous behavior of R_{AA} at forward rapidity at higher p_T can be traced back to the parton distribution function. As has been pointed out earlier, see e.g. [166], the determination of nuclear parton distribution functions (nuclear PDFs) from experimental data is ambiguous. These uncertainties can also influence the calculation of the nuclear modification factor at mid and forward rapidity at RHIC. To illustrate this, here we compare results obtained with the nuclear parton distribution functions as determined by NPDF04 [166] with those that were employed so far, namely EKS98. We remind that the nucleon parton distributions which NPDF04 and EKS98 rely on, namely MRST01 and CTEQ5, respectively, lead to almost the same prediction of the inclusive cross section for π^0 production in $p + p$ collisions (compare Fig. 4.1 and Fig. 4.2).

In Fig. 4.16, we show the neutral pion R_{AA} at midrapidity in central and midperipheral Au+Au collisions at RHIC as obtained with the two different nuclear PDFs.

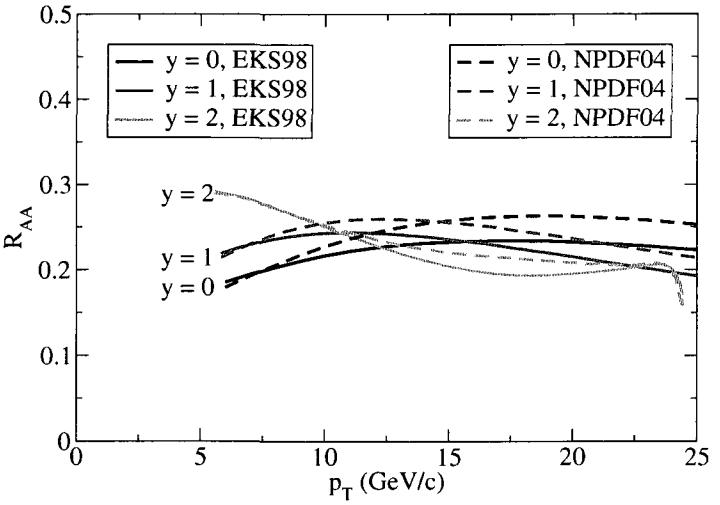

Figure 4.17: Comparing neutral pion R_{AA} at different rapidities using different descriptions of nuclear parton distribution functions, $b = 2.4$ fm.

Differences due to the different nuclear PDFs appear especially at larger transverse momenta of the produced pions. The same holds true for R_{AA} at forward rapidity, see Fig. 4.17 for a comparison in central collisions.

It is possible to trace these differences in R_{AA} back to differences in the initial jet distributions resulting mainly from the different shadowing descriptions. We show in Fig. 4.18 upper panel the ratio of the initial quark and anti-quark jet distributions as inferred from NPDF04 to EKS98. This translates - after jet-energy loss and fragmentation have been taken into account - into a similar behavior of the ratios of the nuclear suppression factor R_{AA} in the two cases. Differences in the initial distribution (mainly resulting from different nuclear shadowing) will therefore be reflected in R_{AA} at mid and forward rapidity and at different centralities. This clearly demonstrates that that R_{AA} is not only sensitive to the employed jet quenching formalism but also to nuclear shadowing effects. The reason is that – even after energy loss and fragmentation – R_{AA} is sensitive to the initial jet distribution which in turn varies within the uncertainties of the determination of nuclear shadowing. A further reduction of uncertainties in the determination of nuclear shadowing effects will make a more stringent test of jet quenching formalisms by R_{AA} measurements.

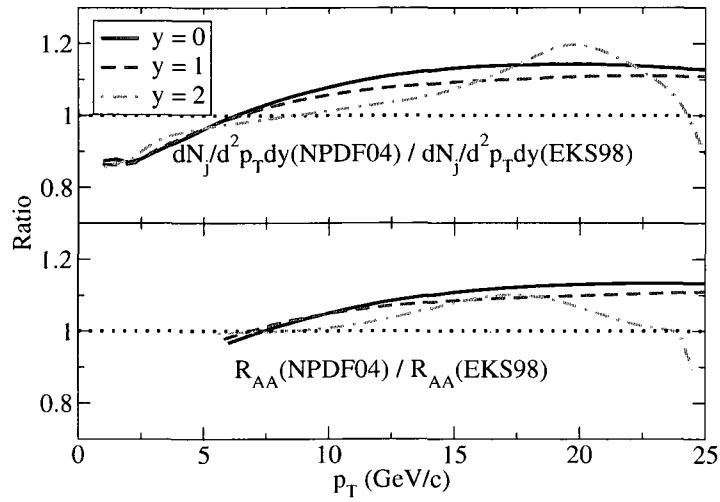

Figure 4.18: The ratio (NPDF04/EKS98) for the initial quark plus anti-quark jet distributions (upper) and nuclear modification factors R_{AA} (lower) using different descriptions of nuclear parton distribution functions, $b = 2.4$ fm.

In the above calculation, the 3D hydrodynamical model has been applied to describe the evolution of the thermalized medium created at RHIC. One may address the question: how the above results would change if one utilizes a 2D hydrodynamical evolution model? Here we investigate this issue by comparing the full 3D hydrodynamical calculation to an effective 2D boost-invariant approach in which the hydrodynamical solution at midrapidity is assumed to describe the medium at forward rapidity. More specifically, the information of the medium at finite rapidity is inferred by applying longitudinal boost invariance,

$$T(\eta,\tau,\vec{r}_\perp) = T(0,\tau,\vec{r}_\perp), \vec{\beta}_\perp(\eta,\tau,\vec{r}_\perp) = \frac{\vec{\beta}_\perp(0,\tau,\vec{r}_\perp)}{\cosh\eta}, \beta_z(\eta,\tau,\vec{r}_\perp) = \tanh\eta, \quad (4.20)$$

where the medium profile at midrapidity is obtained from 3D hydrodynamical calculation. This corresponds effectively to imposing *a posteriori* Bjorken expansion onto the non-Bjorken hydrodynamical evolution. We study the ratio of $R_{\rm AA}$ by imposing a boost invariant expansion, and comparing with the fully 3D non-Bjorken evolution.

Fig. 4.19 shows a calculation at forward rapidities for non-central collisions with a finite impact parameter of $b = 7.5$ fm. This ratio is obviously not measurable, but is interesting from a theoretical point of view. Its relatively strong deviations from

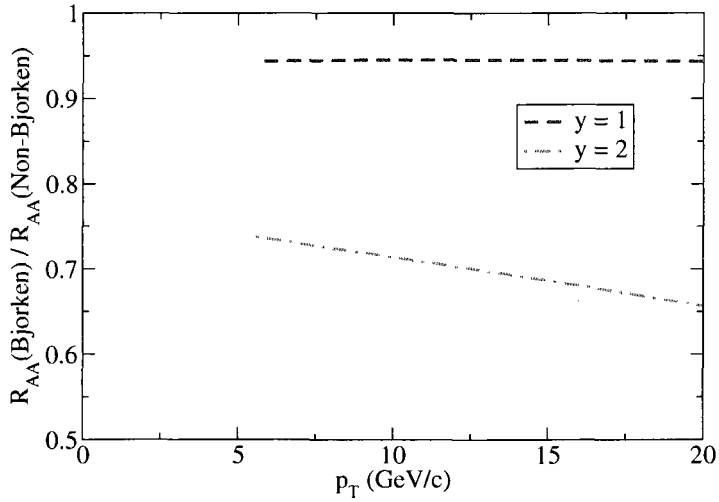

Figure 4.19: The ratio of the neutral pion R_{AA} imposing a boost-invariant expansion to R_{AA} as calculated from the 3D hydrodynamical (non-Bjorken) medium, $b = 7.5$ fm.

1 at $y = 2$ stem mainly from the different transverse temperature profiles at forward rapidity in the non-Bjorken evolution whereas these differences at $y = 1$ are not significant. The fact that the ratio is rather flat in p_T (it varies only in the range of 0.7 ± 0.05 for $y = 2$) indicates that the reduction of the quenching power of the medium in the non-Bjorken case compared to the boost-invariant one is similar for partons over the full range of initial jet energies probed in the collision. Therefore a measurement of the absolute normalization of R_{AA} at midrapidity and forward rapidities might be useful in quantifying the deviations arising from the simplifications made in boost invariant expansion models.

In 3D hydrodynamical calculation, the longitudinal distribution of the initial medium profile is parametrized by the function $H(\eta)$ in Eq. (4.5). With this input, the final temperature and flow profiles are obtained by solving the hydrodynamical evolution equations in both transverse and longitudinal directions simultaneously. One might be interested in the influence of the longitudinal evolution on the medium expansion in the transverse directions. To address this issue, we may still assume the boost invariance for flow profiles, but the temperature profile of the medium at finite

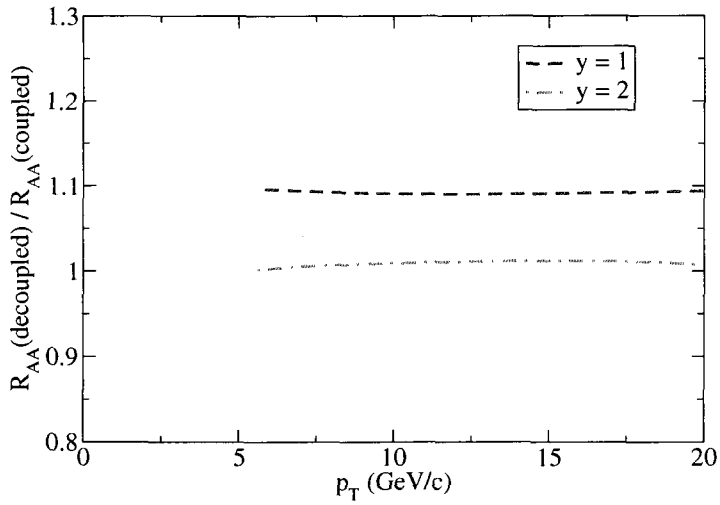

Figure 4.20: The ratio of the neutral pion R_{AA} by decoupling longitudinal direction from transverse direction to R_{AA} as calculated from the 3D hydrodynamical (coupled) medium, $b = 7.5$ fm.

rapidity is reduced by the factor $H(\eta)$ compared to that at mid rapidity,

$$T(\eta,\tau,\vec{r}_\perp) = T(0,\tau,\vec{r}_\perp)H(\eta), \vec{\beta}_\perp(\eta,\tau,\vec{r}_\perp) = \frac{\vec{\beta}_\perp(0,\tau,\vec{r}_\perp)}{\cosh\eta}, \beta_z(\eta,\tau,\vec{r}_\perp) = \tanh\eta. \quad (4.21)$$

As long as the longitudinal evolution decouple from the transverse expansion, we may use the above equation to infer the medium profiles at finite rapidity from the information at mid rapidity. Thus, by comparing R_{AA} at finite rapidity using the real 3D hydrodynamical calculation (the longitudinal and transverse directions are coupled) to that using the above estimation, we might be able to know whether it is important to include the longitudinal expansion for jet quenching study at forward rapidity. Such comparison is shown in Fig. 4.20, where we show the ratio of R_{AA} from the decoupled case to the coupled case. We may observe that while the longitudinal direction seems decoupled from transverse expansion at very forward rapidity, they couple to each other much stronger in the smaller rapidity regime. As a result, the densities and temperatures of the medium at moderate rapidity are raised by the medium at mid rapidity if we solve the coupled equations in the longitudinal and transverse directions simultaneously, leading to higher suppression of jets.

4.6 Jet quenching at the LHC (in 2D hydro)

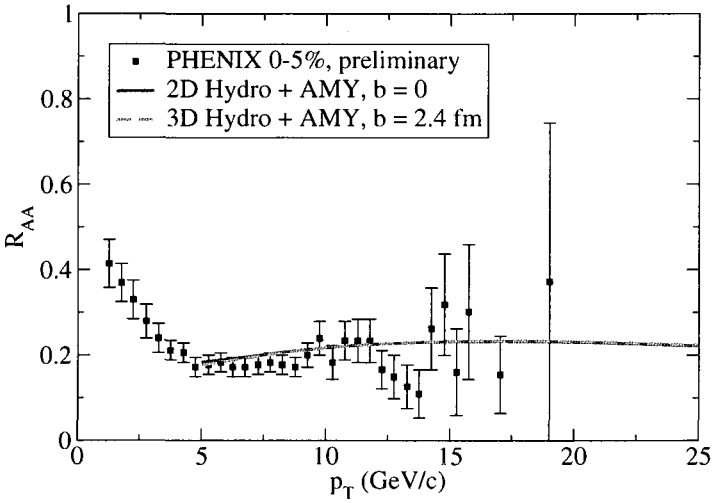

Figure 4.21: The neutral pion R_{AA} at midrapidity in most central Au+Au collisions at RHIC compared with PHENIX data. Two different hydrodynamical models (2D and 3D) are used for the description of the thermalized medium created at RHIC.

In this section, we calculate the nuclear modification factor R_{AA} for charged hadron production as a function of p_T in Pb+Pb collisions at $\sqrt{s_{NN}} = 5.5$ TeV in central collisions at mid-rapidity at the LHC. The energy loss of the partonic jets is calculated by applying the same formalism described in previous sections to calculate gluon bremsstrahlung. Here we use a boost-invariant ideal hydrodynamic model with initial conditions calculated from perturbative QCD + saturation [138, 167].

The strong coupling constant α_s is a direct measure of the interaction strength between the jet and the thermalized soft medium and is the only quantity not uniquely determined in the model, once the temperature and flow evolution is fixed by the initial conditions and subsequent hydrodynamical expansion. We verified that by assuming a constant $\alpha_s = 0.33$, R_{AA} for π^0 production as a function of p_T as obtained in the same boost-invariant ideal hydrodynamical model adjusted to Au+Au collisions at $\sqrt{s_{NN}} = 0.2$ TeV at RHIC [138] is in agreement with preliminary data from PHENIX in central collisions at RHIC. The result is very close to the one obtained in 3D hydrodynamics presented in previous sections, as shown in Fig. 4.21.

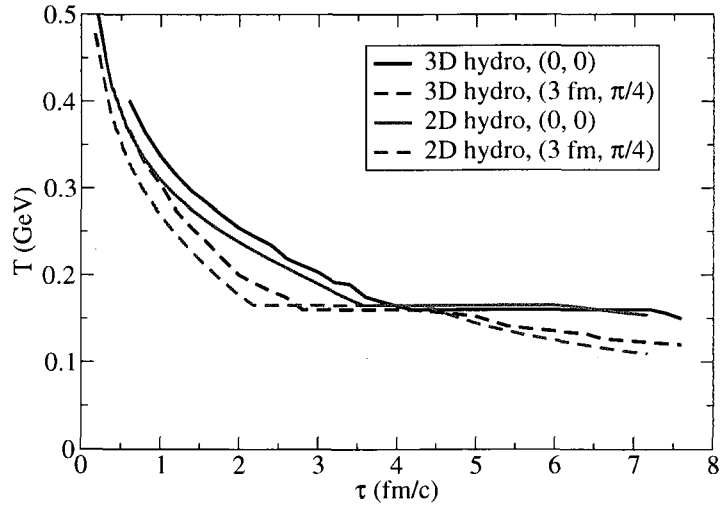

Figure 4.22: The time evolution of the temperature seen by a jet initially created at (r_0, ϕ_0) moving in plane through the nuclear medium created in most central Au+Au collisions at RHIC ($b = 0$ for 2D and $b = 2.4$ fm for 3D).

Although the calculations of R_{AA} in two different hydrodynamical models agree with each other, the medium profiles inferred from two models are quite different. Especially, the initial conditions are quite different between two hydrodynamical models, i.e., the initial equilibrium time $\tau_i = 0.6$ fm/c in 3D hydrodynamical model [137], whereas $\tau_i = 0.17$ fm/c in 2D hydrodynamical model [138]. This difference is understood from different assumptions employed to infer the initial conditions. In Fig. 4.22, we compare the temperature profiles from 2D and 3D hydrodynamical calculations for Au+Au collisions at RHIC.

It is conjectured that α_s should not be changed very much at the LHC since the initial temperature is about twice larger than the one at RHIC whereas α_s is only logarithmically dependent on temperature. In Fig. 4.23 we present a prediction for charged hadron R_{AA} as a function of p_T at mid-rapidity for central collisions at the LHC. We present results for $\alpha_s = 0.33$ and 0.25. We consider that these two values of α_s define a sensible band of physical parameters. Note that here we only include the radiative energy loss from induced gluon radiation. The above prediction for the LHC will be changed if we include the collisional energy loss (see Chapter 5).

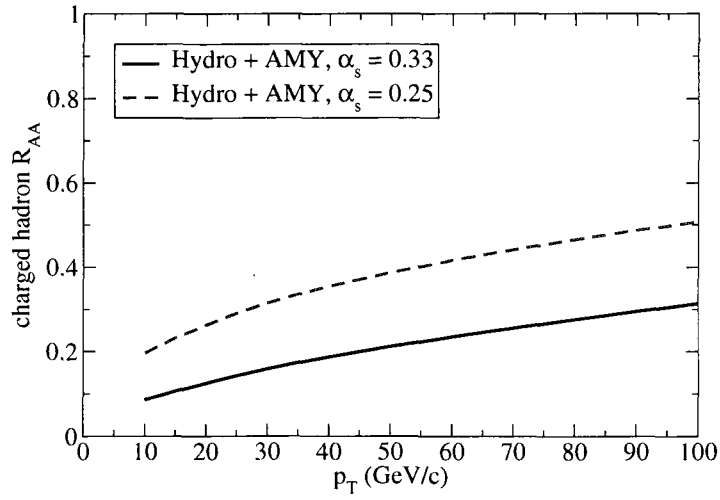

Figure 4.23: The p_T dependence of the nuclear modification factor R_{AA} for charged hadrons in central Pb+Pb collisions at mid-rapidity at the LHC.

4.7 Conclusions

In this chapter, we have studied the jet energy loss by employing a 3D hydrodynamical evolution model [137] to describe the bulk properties of matter created in heavy-ion collisions at RHIC.

We first calculated the nuclear suppression factor R_{AA} as a function of p_T for neutral pions in central and non-central collisions. Our model calculations are in good agreement with the current available experimental measurements. Then we provided the calculations of R_{AA} as a function of p_T and the azimuth ϕ in non-central collisions. These give us more capabilities to understand the interaction between hard jets and the hot and dense medium at RHIC once further data become available. We furthermore studied R_{AA} as a function of p_T in central and non-central collisional at forward rapidity. It is found that a measurement of these dependences might not only be able to reveal more information about the nuclear medium, but also provide a possibility to observe nuclear shadowing effects in the initial parton distribution function indirectly given appropriate experimental resolution.

In conclusion, our study provides a stringent test of our theoretical understanding of jet energy over a variety of initial jets and medium profiles, and thus lays the

groundwork for a tomography of the nuclear medium. It is noted that additional tomographic information can be obtained by measuring high p_T triggered correlations. This will be addressed in Chapter 6.

5

Radiative and collisional jet energy loss in the quark-gluon plasma

This chapter follows our recent work [104, 105], where we calculate and compare radiative and collisional energy loss of hard partons traversing a quark-gluon plasma. We include both radiative energy loss by induced gluon radiation and additional energy loss by elastic collisions. It is found that the solution of Fokker-Planck equations of the probability density distributions of partons until fragmentation is decisive for a correct calculation of the nuclear modification factor R_{AA} for hadron production in heavy ion collisions. While the averaged energy loss induced by elastic collisions is smaller compared to the radiative one, the time evolution of parton distribution function differ significantly in both cases. We find that the magnitude of R_{AA} is sensitive to the inclusion of both collisional and radiative energy loss contributions.

5.1 Introduction

In Chapter 4, we presented a calculation of R_{AA} in central and non-central collisions by calculating the jet energy loss induced by gluon bremsstrahlung. In this chapter, we consistently incorporate collisional and radiative energy loss in the same formalism and to employ this formalism in a realistic description of energy loss of hard p_T leading partons in the soft nuclear medium as described by (3+1)-dimensional hydrodynamics in $\sqrt{s_{NN}} = 200$ GeV Au+Au collisions at RHIC.

Several points are to be emphasized here. First, although there have been extensive literatures addressing the radiative or collisional energy of hard jets in a thermal medium, this is the first study which incorporates both radiative and collisional energy loss in the same formalism. Second, in many previous jet-quenching calculations, the

average energy loss is applied to the primary partons. However, bremsstrahlung and collisional energy loss are not well described by an average energy loss alone. In fact, the evolution of the probability density distributions of partons until fragmentation is the decisive quantity for such studies [131]. In our model, we directly evolve the spectrum of partons as they undergo bremsstrahlung and collisional energy loss. Third, a lot of approaches take the LPM coherence effect as a parametrically large suppression. This is only true when the parent parton and the emitted gluon are highly energetic. For small radiated gluon energies, the LPM suppression can be significantly less. In fact, those bremsstrahlung events with small energy radiation are of significant importance in jet quenching due to the steeply falling initial parent parton spectrum [131]. Fourth, until recently most jet quenching calculations used simple medium models only loosely constrained by the value of bulk observables. Here we use the (3+1)-dimensional hydrodynamics to describe the thermalized medium produced in Au+Au collisions at RHIC [137].

5.2 Collisional jet energy loss in QGP

We now consider a high energy jet of energy E traversing a thermalized QCD plasma with a temperature T. The jet will lose energy by scattering off thermal particles, i.e., through binary elastic collisions. The interaction rate $\Gamma(E)$ for the binary scatterings between the jet of energy E and the thermal particles is given by

$$\Gamma(E)=\frac{d_k}{2E}\int\frac{d^3k}{(2\pi)^3 2k}\int\frac{d^3p'}{(2\pi)^3 2E'}\int\frac{d^3k'}{(2\pi)^3 2k'}(2\pi)^4\delta^4(P+K-P'-K') \times|\bar{M}|^2 f(k)[1\pm f(k')]. \tag{5.1}$$

In the above equation $P=(E,\vec{p})$ and $K=(k,\vec{k})$ are the four-momenta of the incoming jet and the thermal parton, and $P'=(E',\vec{p}')$ and $K'=(k',\vec{k}')$ are four-momenta of the outgoing jet and thermal parton. Here we are interested in the energy loss of high energy light quarks and gluons and all the particles are set to be massless. The phase space is weighted by a thermal distribution for the incoming thermal parton with d_k its statistical degeneracy, and a Bose-enhancement or Pauli-blocking factor for the outgoing thermal parton.

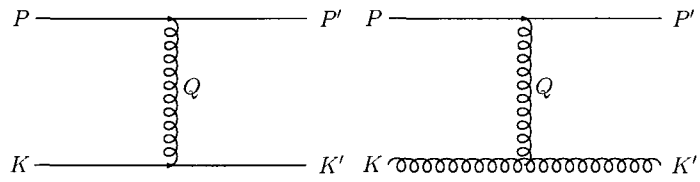

Figure 5.1: The t channel Feynman diagrams for the collisional energy loss of quarks: qq and qg scatterings.

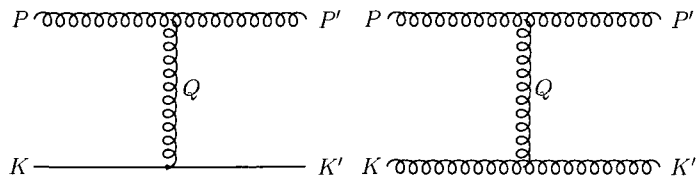

Figure 5.2: The t channel Feynman diagrams for the collisional energy loss of gluons: gq and gg scatterings.

Assuming that the energy of the incoming jet is very high $E \gg T$, the amplitude is dominated by t channel gluon exchange processes, as shown in Fig. 5.1 and Fig. 5.2. The energy loss rate dE/dt is related to the differential interaction rate by the following relation,

$$\frac{dE}{dt} = \int dE'(E - E')\frac{d\Gamma}{dE'}(E, E'). \tag{5.2}$$

One may find

$$\begin{aligned}\frac{dE}{dt} = &\frac{d_k}{2E}\int \frac{d^3k}{(2\pi)^3 2k}\int \frac{d^3p'}{(2\pi)^3 2E'}\int \frac{d^3k'}{(2\pi)^3 2k'}(2\pi)^4\delta^4(P + K - P' - K') \\ &\times (E - E')|\bar{M}|^2 f(k)[1 \pm f(k')]\,,\end{aligned} \tag{5.3}$$

To evaluate the integration from t channel processes, we may use the three-momentum δ function to perform the p' integration. By introducing an integration variable $\omega = p - p' = k' - k$, the energy loss rate can be written as

$$\begin{aligned}\frac{dE}{dt} = &d_k\int \omega\frac{d\omega}{2\pi}\int \frac{d^3k}{(2\pi)^3}\int \frac{d^3k'}{(2\pi)^3}\frac{1}{16pp'kk'}(2\pi)\delta(p - p' - \omega)(2\pi)\delta(k' - k - \omega) \\ &\times |\bar{M}|^2 f(k)[1 \pm f(k')].\end{aligned} \tag{5.4}$$

We may shift $\vec{k}'$ integration to $\vec{q} = \vec{p} - \vec{p}' = \vec{k}' - \vec{k}$ and choose a coordinate such that the z axis is along the direction of $\vec{q}$ while $\vec{p}$ lies in the xz plane. Then the two δ

functions may be written as

$$\delta(p-p'-\omega)=\frac{p'}{pq}\delta\left(\cos\theta_{pq}-\frac{\omega}{q}+\frac{t}{2pq}\right),$$
$$\delta(k'-k-\omega)=\frac{k'}{kq}\delta\left(\cos\theta_{kq}-\frac{\omega}{q}-\frac{t}{2kq}\right). \tag{5.5}$$

By taking the limit $p\rightarrow\infty$, one may find

$$\frac{dE}{dt}=\frac{d_k}{(2\pi)^3}\frac{1}{16p^2}\int_0^p dq\int_{-q}^{q}\omega d\omega\int_{\frac{q-w}{2}}^{\infty}dk\int_0^{2\pi}\frac{d\phi_{kq|pq}}{2\pi}|\bar{M}|^2 f(k)[1\pm f(k')], \tag{5.6}$$

where $\phi_{pq|kq}$ the is the angle between the $\vec{p}\times\vec{q}$ plane and $\vec{k}\times\vec{q}$ plane. The limits of integrations come from taking into account the restriction from $q<k+k'$, $q<p+p'$ and $-q<\omega<q$. As is well known, Eq. (5.6) has an infrared logarithmic divergence which has to be screened by plasma effects. Here we introduce an arbitrary momentum scale q_c to divide the integration over q into two parts, hard part $q_c<q<p$ and soft part $0<q<q_c$. The contribution from hard momentum transfer $\sim T$ can be calculated at tree level, but for the soft momentum transfer $\sim gT$, the hard thermal loop corrections (HTL) [125] to the propagator of the exchanged gluon must be employed. The contributions must be matched together consistently to give the correct energy loss rate to the leading order.

We first compute the energy loss from the hard momentum transfer part. Fig. 5.1 and Fig. 5.2 show the t channel scatterings experienced by the quark jets and gluon jets. And the corresponding matrix elements squared are [168, 169]

$$|\bar{M}_t|^2_{qq}=\frac{4}{9}g_s^4\frac{s^2+u^2}{t^2},\quad |\bar{M}_t|^2_{qg}=2g_s^4\left(1-\frac{su}{t^2}\right);$$
$$|\bar{M}_t|^2_{gq}=2g_s^4\left(1-\frac{su}{t^2}\right),|\bar{M}_t|^2_{gg}=\frac{9}{2}g_s^4\left(\frac{17}{8}-\frac{su}{t^2}\right). \tag{5.7}$$

To evaluate the integral in Eq. (5.6), we need the expressions for the Mandelstam variables s, t and u in the matrix element $|\bar{M}|^2$. They are

$$t=\omega^2-q^2,$$
$$s=-\frac{t}{2q^2}\left\{[(p+p')(k+k')+q^2]-\cos\phi_{pq|kq}\sqrt{(4pp'+t)(4kk'+t)}\right\},$$
$$u=-s-t. \tag{5.8}$$

Then we obtain, i.e., for $qq \to qq$ scattering,

$$\int \frac{d\phi_{kq|pq}}{2\pi} |\bar{M}_t|^2_{qq} = g_s^4 \left[\frac{1}{3} - \frac{2(2pp' + 2kk' + \omega^2)}{9q^2} + \frac{(p+p')^2(k+k')^2}{3q^4} \right]. \tag{5.9}$$

Furthermore, we rewrite the Bose or Fermi distribution function in terms of the infinite sum of Boltzmann distribution function,

$$\frac{1}{\exp(k/T) \mp 1} = \sum_{n=1}^{\infty} (\pm 1)^{n-1} \exp(-nk/T). \tag{5.10}$$

By inserting the above expansion, the integral in Eq. (5.6) can be computed analytically. Then we take the limit $p \to \infty$ and neglect the terms that vanish as $q_c \to 0$. By using the following relations

$$\sum_n \frac{1}{n^2} = \zeta(2) = \frac{\pi^2}{6}, \ \sum_n \frac{\ln(n)}{n^2} = -\zeta'(2) \approx 0.937548, \tag{5.11}$$

or

$$\sum_n (-1)^{n-1} \frac{1}{n^2} = \frac{1}{2}\zeta(2), \ \sum_n (-1)^{n-1} \frac{\ln(n)}{n^2} = -\frac{1}{2}[\zeta'(2) + \ln(2)\zeta(2)], \tag{5.12}$$

one may obtain, i.e., for soft momentum transfer, $qq \to qq$ scattering,

$$\left. \frac{dE}{dt} \right|_{qq} = \frac{2}{9} N_f \pi \alpha_s^2 T^2 \left[\ln \frac{ET}{q_c^2} - \gamma_E + \frac{\zeta'(2)}{\zeta(2)} + \ln 2 + \frac{23}{12} \right]. \tag{5.13}$$

Next we compute the energy loss from the soft momentum transfer part. We may write t channel matrix element squared $|\bar{M}_t|^2$, i.e., for $qq \to qq$ scattering as

$$|\bar{M}_t|^2_{qq} = L_{\alpha\alpha'}(P, P') L_{\beta\beta'}(K, K') D^{\alpha\beta}(Q) D^{*\alpha'\beta'}(Q). \tag{5.14}$$

By tracing over the quark line and averaging the spin and color of the initial particle, one finds, for $q \sim gT$,

$$L_{\alpha\alpha'}(P, P') = \frac{1}{6} g_s^2 \mathrm{tr}[T^a T^b] 8 P_\alpha P'_{\alpha'}. \tag{5.15}$$

The matrix element squared is then simplified to be

$$|\bar{M}_t|^2_{qq} = \frac{32}{9} g_s^4 \left| P_\alpha D^{\alpha\beta}(Q) K_\beta \right|^2. \tag{5.16}$$

In the coulomb gauge, the effective thermal propagator takes the form of

$$D^{\alpha\beta}(Q)=\Delta_L(\omega,q)\delta^{\alpha 0}\delta^{\beta 0}+\Delta_T(\omega,q)P_T^{\alpha\beta}, \tag{5.17}$$

where $P_T^{00}=0$, $P_T^{ij}=\delta^{ij}-\hat{q}^i\hat{q}^j$ is the transverse projector and $\Delta_L(\omega,q)$ and $\Delta_T(\omega,q)$ are longitudinal and transverse gluon propagators, whose expressions may be found in [129]

$$\Delta_T(\omega,q)=\frac{1}{F_T-Q^2},\quad \Delta_L(\omega,q)=\frac{1}{F_L-Q^2}\frac{Q^2}{q^2}, \tag{5.18}$$

where the explicit expressions for $F_L(k_0,k)$ and $F_T(k_0,k)$ are,

$$F_L=2m_g^2(1-x^2)(1-xQ_0(x))\ ,\quad F_T=m_g^2-\frac{F_L}{2} \tag{5.19}$$

In the above equations, $Q_0(x)=\frac{1}{2}\ln\frac{x+1}{x-1}$ is the Legendre function with $x=\omega/q$, and m_g is the thermal gluon mass, $m_g^2=\frac{1}{2}(1+N_f/6)g^2T^2$. The final expression of matrix element squared $|\bar{M}_t|^2$ is

$$|\bar{M}_t|^2_{qq}=\frac{32}{9}g_s^4p^2k^2\left|\Delta_L+\Delta_T[(\hat{p}\cdot\hat{q})(\hat{k}\cdot\hat{q})-(\hat{p}\cdot\hat{k})]\right|^2. \tag{5.20}$$

Note that $(\hat{p}\cdot\hat{q})(\hat{k}\cdot\hat{q})-(\hat{p}\cdot\hat{k})=\sin\theta_{pq}\sin\theta_{kq}\cos\phi_{kq|pq}$, and at leading order, $\sin\theta_{pq}\approx\sin\theta_{kq}\approx\sqrt{1-\omega^2/q^2}$, we obtain

$$\int\frac{d\phi_{kq|pq}}{2\pi}|\bar{M}_t|^2_{qq}=\frac{32}{9}g_s^4p^2k^2\left[|\Delta_L|^2+\frac{1}{2}\left(1-\frac{\omega^2}{q^2}\right)^2|\Delta_T|^2\right]. \tag{5.21}$$

The expressions of $|\Delta_L|^2$ and $|\Delta_T|^2$ are

$$\begin{aligned}|\Delta_L|^2&=\frac{1}{[q^2+\pi xm_g^2Q_L(x)]^2+\pi^2x^2m_g^4},\\ |\Delta_T|^2&=\frac{1}{[\omega^2-q^2+\frac{1}{2}\pi x(1-x^2)m_g^2Q_T(x)]^2+\frac{1}{4}\pi^2x^2(1-x^2)^2m_g^4},\end{aligned} \tag{5.22}$$

where the functions $Q_L(x)$ and $Q_T(x)$ are

$$Q_L(x)=\frac{1}{\pi}\left(\frac{2}{x}-\ln\frac{1+x}{1-x}\right),\quad Q_T(x)=\frac{1}{\pi}\left(\frac{2x}{1-x^2}+\ln\frac{1+x}{1-x}\right). \tag{5.23}$$

Note that the integral Eq. (5.3) is symmetric under the exchange of $\vec{k}$ and $\vec{k}'$. Therefore it can be symmetrized by replacing the thermal distribution factor $f(k)[1-f(k')]$

by $(f(k)-f(k'))/2$. By making use of the fact that $q \sim gT$, the thermal distribution factor can be expanded to lowest order in ω,

$$f(k)-f(k')=-\omega f'(k)+\cdots . \tag{5.24}$$

To further simplify the integration, it is convenient to change integration variable ω to $x=\omega/q$. The integration over q can be done analytically by taking the limit $q_c \gg m_g$, revealing a logarithmic dependence on q_c. The integration over x for the logarithmic term can be evaluated analytically. The final result for the energy loss rate from soft part reads

$$\left.\frac{dE}{dt}\right|_{qq}=\frac{2}{9}N_f\pi\alpha_s^2T^2\left[\ln\frac{q_c^2}{m_g^2}+c_s\right]. \tag{5.25}$$

In the above equation, the constant c_s accounts for the following integration:

$$\begin{aligned}C_s=-\int_0^1 dx x^2\Big[&\frac{3}{2}\ln(\pi^2x^2)-\ln 2+\ln(1+Q_L^2(x))+2Q_L(x)\arctan\left(1/Q_L(x)\right)\\&+\frac{1}{2}\ln(1+Q_T^2(x))+Q_T(x)\arctan\left(1/Q_T(x)\right)\Big].\end{aligned} \tag{5.26}$$

The remaining integration over x may be evaluated numerically, giving $c_s=-1.66246$. It is noted that the result for soft part is consistent with the calculation in [170], where the energy loss of a high energy quark is computed by considering the effect of the Lorentz force on the quark by the induced chromo-electric field described by the screened dielectric functions.

The resulting expressions for collisional energy loss rate $dE/dt|_{ab}$ for the scattering of a light hard parton a off a soft thermal parton b are:

$$\begin{aligned}\left.\frac{dE}{dt}\right|_{qq}&=\frac{2}{9}N_f\pi\alpha_s^2T^2\left[\ln\frac{ET}{m_g^2}+c_f+\frac{23}{12}+c_s\right],\\ \left.\frac{dE}{dt}\right|_{qg}&=\frac{4}{3}\pi\alpha_s^2T^2\times\left[\ln\frac{ET}{m_g^2}+c_b+\frac{13}{6}+c_s\right];\\ \left.\frac{dE}{dt}\right|_{gq}&=\frac{1}{2}N_f\pi\alpha_s^2T^2\left[\ln\frac{ET}{m_g^2}+c_f+\frac{13}{6}+c_s\right],\\ \left.\frac{dE}{dt}\right|_{gg}&=3\pi\alpha_s^2T^2\times\left[\ln\frac{ET}{m_g^2}+c_b+\frac{131}{48}+c_s\right].\end{aligned} \tag{5.27}$$

In the above equations, the two constants $c_b = -\gamma_E + \zeta'(2)/\zeta(2) + \ln 2$ and $c_f = -\gamma_E + \zeta'(2)/\zeta(2)$. Note that the collisional energy loss as calculated by [170] differs by constant terms in the brackets in Eq. (5.27) since only the s^2/t^2 terms were kept by setting $t = 0$ and $u = -s$ in the numerators of the matrix elements squared $|\bar{M}_t|^2$ for the hard scattering processes there. Remember that for hard momentum transfer $\sim T$, $t = \omega^2 - q^2$ is not necessarily small. It is also noted that these differences are not of phenomenological importance.

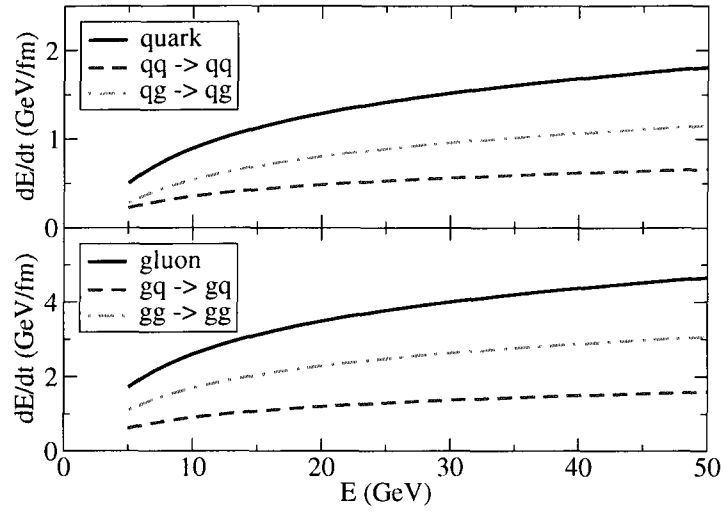

Figure 5.3: The energy loss rate dE/dt for quarks (upper) and gluons (lower) in a medium of temperature $T = 400$ MeV.

In Fig. 5.3, we plot the energy loss rate dE/dt for quarks and gluons when they are transversing a thermal medium ($N_f = 3$) with a constant temperature $T = 400$ MeV. Here, the strong coupling constant of jet-medium interaction is taken to be $\alpha_s = 1/3$. Due to different color charges carried by quarks and gluons, the energy loss experienced by gluon jets is larger than that by the quark jets ($\sim 9/4$). Also, the energy loss rate of jets by scattering off the thermal gluons is larger than that by scattering off the thermal quarks ($\sim 6/N_f$) because of different degeneracies for the incomong thermal particles.

5.3 Incorporation of collisional jet energy loss in AMY

In this section, we will address how we incorporate the collisional energy loss and radiative energy loss consistently in the context of the AMY formalism. We have already seen, in Chapter 3 and Chapter 4, jet momentum distribution $P(E,t) = dN(E,t)/dE$ evolves in the medium according to a set of coupled Fokker-Planck type rate equations with the following generic form,

$$\frac{dP_j(E,t)}{dt} = \sum_{ab} \int d\omega \left[P_a(E+\omega,t) \frac{d\Gamma_{a\to j}(E+\omega,\omega)}{d\omega dt} - P_j(E,t) \frac{d\Gamma_{j\to b}(E,\omega)}{d\omega dt} \right], \quad (5.28)$$

where $d\Gamma(E,\omega)/d\omega dt$ are the transition rate for processes where partons of energy E lose energy ω. The $\omega < 0$ part of the integration incorporates processes which increase a particle's energy. The radiative part of the transition rate has been discussed in Chapter 3. In the following, we will focus on addressing the collisional transition rates.

Compared to radiative loss, collisional losses are more dominated by small energy transfers, therefore it should be an adequate procedure to approximate elastic collisions by a mean energy loss plus a momentum diffusion term as dictated by detailed balance. If elastic collisions turn out to dominate jet quenching we may want to improve this treatment, but if they are subdominant it should be sufficient to quantify their effect. More specifically, for small energy transfer ω, we may expand the gain term in the Fokker-Planck equation to the second order,

$$P(E+\omega)\frac{d\Gamma(E+\omega,\omega)}{d\omega dt} = P(E)\frac{d\Gamma(E,\omega)}{d\omega dt} + \omega \frac{d}{dE}\left[P(E)\frac{d\Gamma(E,\omega)}{d\omega dt}\right] + \frac{1}{2}\omega^2 \frac{d^2}{dE^2}\left[P(E)\frac{d\Gamma(E,\omega)}{d\omega dt}\right] + \cdots. \quad (5.29)$$

Then the Fokker-Planck equation becomes,

$$\frac{dP(E)}{dt} = \frac{d}{dE}[A \times P(E)] + \frac{d^2}{dE^2}[B \times P(E)] + \cdots, \quad (5.30)$$

where the transport coefficients A and B are called drag and diffusion coefficients. They are determined to be

$$A = \int d\omega \omega \frac{d\Gamma(E,\omega)}{d\omega dt} = \frac{dE}{dt}, \quad B = \frac{1}{2}\int d\omega \omega^2 \frac{d\Gamma(E,\omega)}{d\omega dt} = T\frac{dE}{dt}, \quad (5.31)$$

where the second relation is derived by using microscopic detailed balance,

$$\frac{d\Gamma(E,\omega)/d\omega dt}{d\Gamma(E,-\omega)/d\omega dt} = \exp\left(\frac{\omega}{T}\right). \tag{5.32}$$

Thus we obtain for small ω

$$\begin{aligned} A &= \frac{1}{2}\int d\omega\omega \left(\frac{d\Gamma(E,\omega)}{d\omega dt} - \frac{d\Gamma(E,-\omega)}{d\omega dt}\right) \\ &= \frac{1}{2}\int d\omega\omega \left[1-\exp\left(-\frac{\omega}{T}\right)\right]\frac{d\Gamma(E,\omega)}{d\omega dt} \approx \frac{1}{2T}\int d\omega\omega^2 \frac{d\Gamma(E,\omega)}{d\omega dt} = \frac{B}{T}. \end{aligned} \tag{5.33}$$

As we perform the numerical computation of discretized Eq. (5.28), such that $\int d\omega \to \Delta_\omega \sum_{\omega=n\Delta_\omega}$, the transition rates for elastic collisions are approximated by two spikes at $\omega = \pm\Delta_\omega$,

$$\frac{d\Gamma(E,\omega)}{d\omega dt} = [1+f_B(\Delta_\omega)]\frac{1}{\Delta_\omega}\frac{dE}{dt}\delta(\omega-\Delta_\omega) + f_B(\Delta_\omega)\frac{1}{\Delta_\omega}\frac{dE}{dt}\delta(\omega+\Delta_\omega), \tag{5.34}$$

where $f_B(\Delta_\omega) = 1/[\exp(\Delta_\omega/T)-1]$ is the Bose-Einstein thermal distribution function. In the limit of small Δ_ω, it may be easily check that the above transition rates yield the correct energy loss rate and preserves detailed balance. So the above procedure to incorporate the collisional transition rates is equivalent to introducing the drag term and the diffusion term for into the coupled jet evolution equations Eq. (5.28) for the collisional energy loss.

5.4 Results

In this section, we present the calculation and comparison of radiative and collisional energy loss of hard jets traversing a hot and dense medium. To illustrate how collisional and radiative energy loss influence the time evolution of the leading parton distributions, we first consider a single light quark jet of energy $E_i = 16$ GeV traversing through an infinite medium with a constant temperature $T = 400$ MeV. Here, the strong coupling constant of jet-medium interaction is taken to be a constant $\alpha_s = 1/3$.

In Fig. 5.4 we compare the evolution of the jet parton distribution $P(E,t)$ under three different scenarios: (1) with only collisional energy loss, (2) with only radiative energy loss (already calculated in Chapter 3 and Ref. [131]), and (3) with both energy

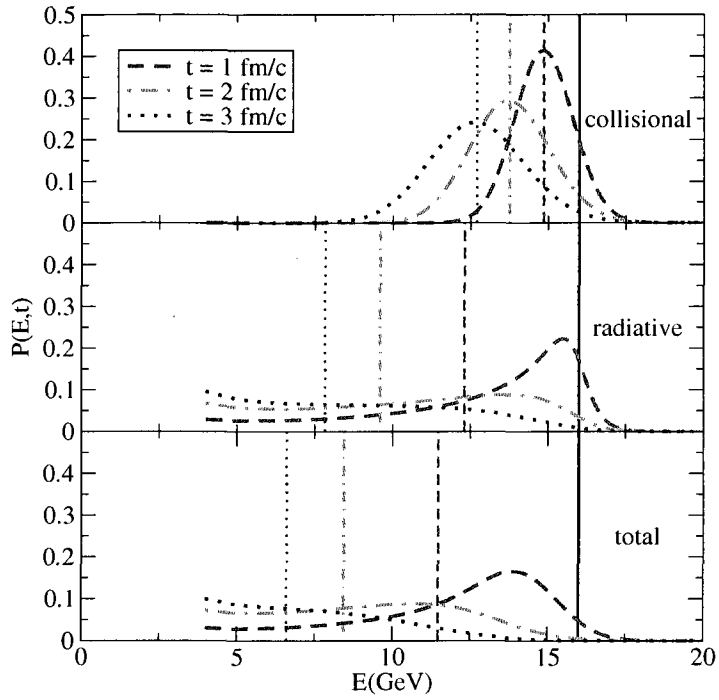

Figure 5.4: The evolution of a quark jet with initial energy $E_i = 16$ GeV propagating through a thermal medium with a constant temperature $T = 400$ MeV, where the vertical lines represent the values of mean energy related to the corresponding distributions.

loss mechanisms. The vertical lines represent the mean energy $\langle E \rangle$, defined as the first moment of the corresponding momentum distribution. The figure indicates as expected that radiation leads to a larger mean energy loss than with elastic collisions only. Adding collisional energy loss to radiative one leads to small change for the mean energy loss of hard jets (compare the vertical lines in the case (2) and the case (3)). While the time evolution of $P(E,t)$ in case (3) resembles qualitatively the case (2) in which only radiative energy loss has been considered, quantitative differences are large, especially at energies closer to E_i.

One may further study the mean energy loss $\langle \Delta E \rangle = E_i - \langle E \rangle$ of single quarks jet with different initial energies. This is illustrated in Fig. 5.5, where we show the fractional mean energy loss of the quark jet as a function of its initial energy E_i after travelling through such a thermal medium for 1 fm/c. We may see that for very high energy quark jets, the energy loss induced by radiation is much larger than that by

elastic collisions (approximately 4 times larger for a light quark with initial energy $E_i = 30$ GeV). The total mean energy loss seems not very sensitive to the inclusion of collisional energy loss for high energy quark jets.

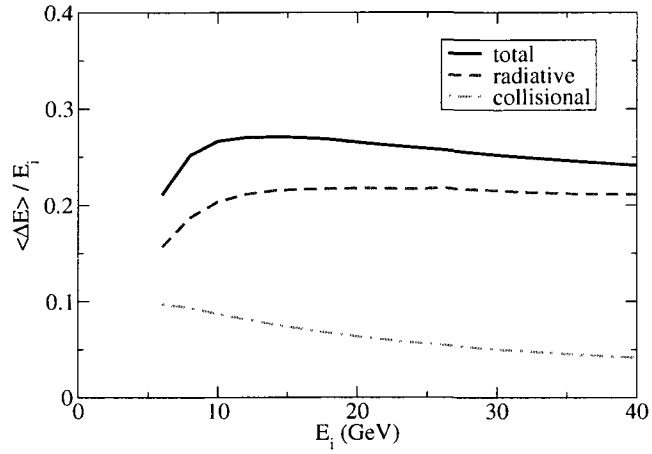

Figure 5.5: The fractional mean energy loss of a quark jet with initial energy E_i after travelling through a thermal medium with a constant temperature $T = 400$ MeV for $t = 1$ fm/c.

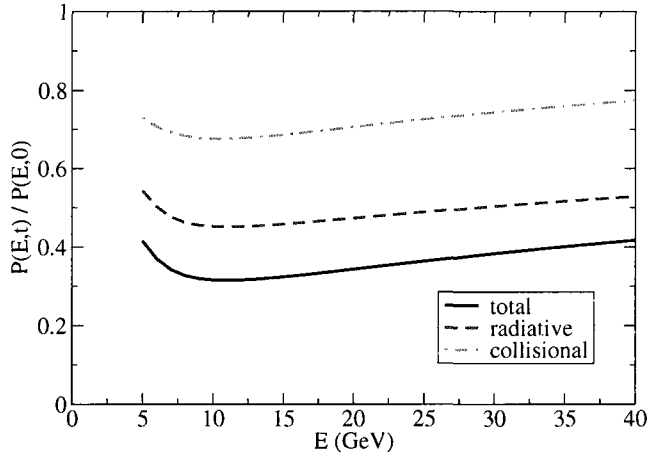

Figure 5.6: The ratio of the final to initial jet spectra $P(E,t)/P(E,0)$ for quark jets after propagating through a thermal medium with a constant temperature $T = 400$ MeV for $t = 1$ fm/c.

We may study the evolution of jet momentum spectra in a thermal medium by evolving the jets with initially a power-law distribution for initial p_T spectra of quarks

and anti-quarks [114],

$$\left.\frac{dN}{d^2p_T dy}\right|_{y=0} = K\frac{a}{(1+p_T/b)^c} \tag{5.35}$$

where $a = 500$, $b = 1.6$ and $c = 7.9$ for quarks, and $a = 130$, $b = 1.9$ and $c = 8.9$ for anti-quarks. K is a constant to account for the next-leading-order corrections to the leading order result as inferred from perturbative QCD calculation.

In Fig. 5.6, we show the ratio of the final spectrum to the initial spectrum as a function of the energy of quark jets after their propagating in such a thermal medium for 1 fm/c. We may observe that for quark jets with such power-law initial spectra, adding collisional energy loss to radiative increases the quenching of jet momentum spectra by approximately 30%.

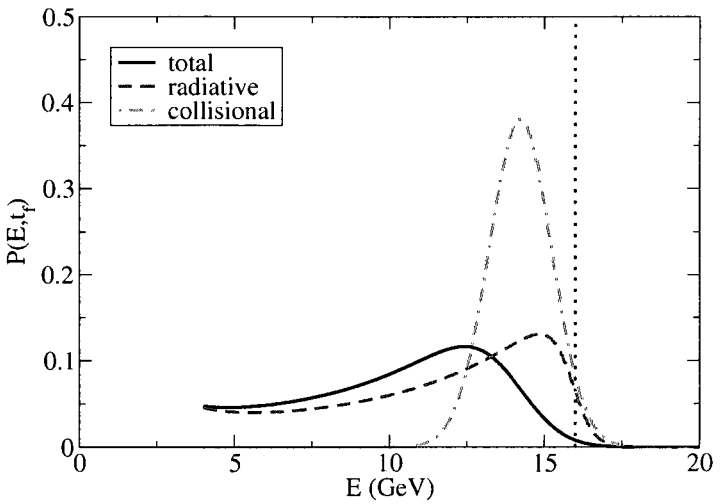

Figure 5.7: The probability distribution function $P(E, t_f)$ of a single particle with initial energy $E_i = 16$ GeV after passing through the nuclear medium created in central collisions ($b = 2.4$ fm) at RHIC. The jet starts from the center of the medium and propagates in plane.

In the following, we perform a more realistic calculation of jet quenching at RHIC by modelling the space-time evolution of the quark-gluon plasma using relativistic fluid dynamics, which has been shown to give a good description of bulk properties at RHIC. Here we employ a fully (3+1)-dimensional hydrodynamical model for the description of Au+Au collisions at RHIC [137]. The product of the initial hard parton densities is determined from the overlap geometry between two nuclei in the

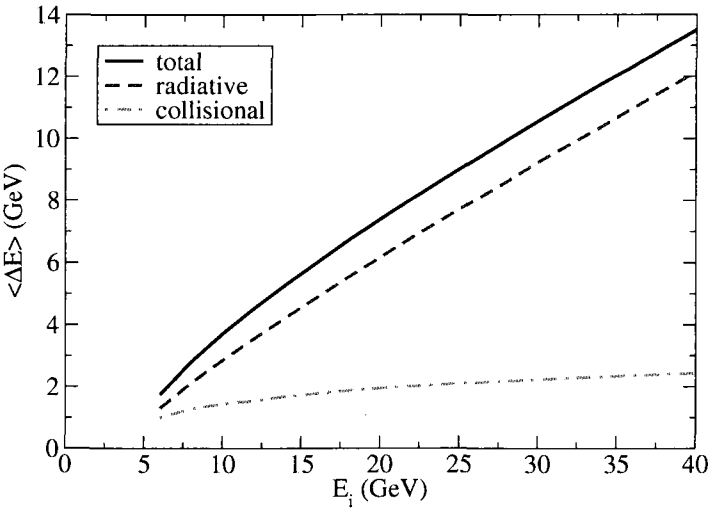

Figure 5.8: The mean energy loss of a quark jet with initial energy E_i passing through the nuclear medium created in most central collisions (b = 2.4 fm) at RHIC. The jet starts from the center of the medium and propagates in plane.

transverse plane of the collision zone. The initial momentum distribution of hard jets is computed from perturbative QCD, using the factorization theorem. The evolution of jet momentum distribution in the thermalized medium is evaluated by solving Fokker-Planck equations with both collisional and radiative energy loss. The final hadron spectrum at high p_T is obtained by the fragmentation of jets in the vacuum after their passing through the (3+1)-dimensional expanding medium. For further details see Chapter 4 where the radiative energy loss has been studied in an analogous manner.

We first study a single light quark jet traversing through a 3D hydrodynamical medium created at RHIC. In Fig. 5.7, we show the final spectra $P(E, t_f)$ of a quark jet with initial energy $E_i = 16$ GeV after its passing through the nuclear medium created in most central Au+Au collisions (b = 2.4 fm) at RHIC. In this figure, the jets are assumed to be created at the center and propagating along the in-plane direction. As usual, we turn on the energy loss at equilibrium time $\tau_i = 0.6$ fm/c and switch off the energy loss when the medium surrounding the jet goes into the hadronic phase. The value of α_s is now taken to be $\alpha_s = 0.27$, which reproduces the most central

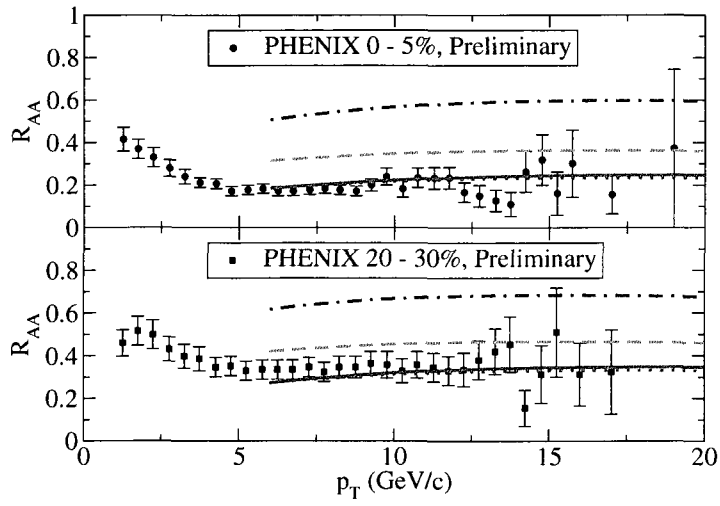

Figure 5.9: Nuclear suppression factor R_{AA} for neutral pions in central and mid-central collisions. Here the dashed curves account for only radiative energy loss, the dash-dotted curves for only collisional energy loss and the solid curves incorporate both radiative and collisional energy loss mechanisms. The dotted curves are the results from Chapter 4 with radiative energy loss only ($\alpha_s = 0.33$).

data for R_{AA} measurements (see Fig. 5.9). In Fig. 5.8, we show the mean energy loss of such quark jets as a function of their initial energies E_i. While in agreement with [97], the average energy loss is not very affected by the addition of collisional contributions, large differences are observed for the final jet distribution between case (3) and case (2). This is especially true for energies close to the initial parton energy E_i. As the initial parton spectrum in relativistic nucleus-nucleus collisions is steeply falling, stronger differences in R_{AA} can result.

In Fig. 5.9 we present the calculation of R_{AA} for neutral pions measured at mid-rapidity for two different impact parameters, 2.4 fm and 7.5 fm, compared with PHENIX data for the most central (0-5%) and mid-central (20-30%) collisions [84]. We present R_{AA} for purely collisional (1) and purely radiative (2) energy loss, as well as the combined case (3). One finds that while the shape of R_{AA} for case (3) is not strongly different from case (2) that has only radiative energy loss, the overall magnitude of R_{AA} changes significantly. The stronger influence on R_{AA} stems from the differences in the evolution of the parton distributions in case (2) and (3), as shown

in Fig. 5.7. This has already been discussed in the case of a constant temperature (compare Fig. 5.4). Therefore, the magnitude of R_{AA} is sensitive to the actual form of the parton distribution functions at fragmentation and not only to the average energy loss of single partons (compare Fig. 5.8).

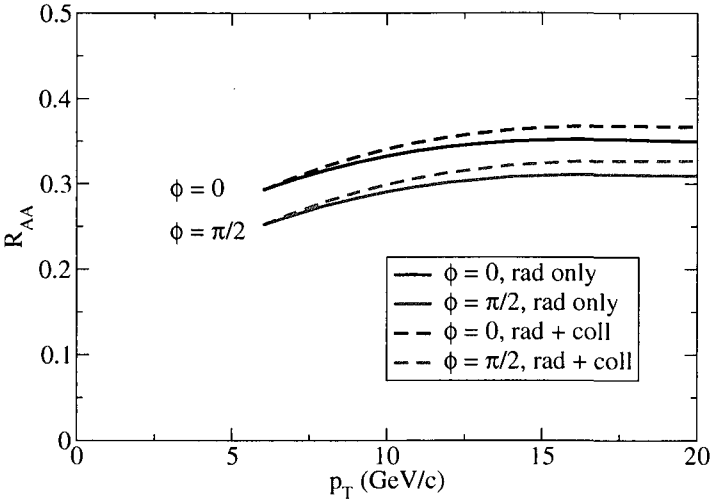

Figure 5.10: Nuclear suppression factor R_{AA} for neutral pions in plane and out of plane in mid-peripheral Au+Au collisions ($b = 7.5$ fm) at RHIC.

In Chapter 4, the observational implications on R_{AA} measurements due to only radiative energy loss is studied. There, we have presented R_{AA} for neutral pions in central collisions as a function of p_T at mid and forward rapidity and have discussed how the azimuthal asymmetry of the medium in non-central collisions allows to put stronger constraints on our understanding of jet energy loss by induced gluon radiation. We have recalculated R_{AA} versus reaction plane including elastic collisions, and only small differences are found in the shape of R_{AA} as a function of p_T and the azimuth after adjusting the coupling strength from $\alpha_s = 0.33$ to $\alpha_s = 0.27$. The effect of the inclusion of collisional energy loss on the shape of R_{AA} is also illustrated in Fig. 5.10, where we show nuclear suppression factor R_{AA} for neutral pions in plane and out of plane in mid-peripheral Au+Au collisions ($b = 7.5$ fm) at RHIC.

We may also perform the calculation of nuclear suppression factor R_{AA} for neutral pions at finite rapidity including elastic collisions. Fig. 5.11 shows R_{AA} for neutral

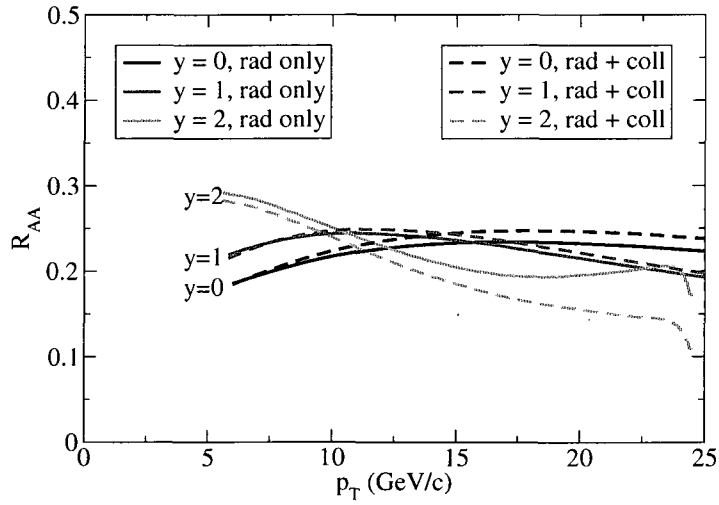

Figure 5.11: Nuclear suppression factor R_{AA} for neutral pions for different rapidities in most central Au+Au collisions (b = 2.4 fm) at RHIC.

pions in most central Au+Au collisions (b = 2.4 fm) at RHIC for three different rapidities. Compared to the results from Chapter 4 with radiative energy loss only ($\alpha_s = 0.33$), we may observe a sizable change in the shape of R_{AA} at large rapidity after the inclusion of collisional energy loss, (i.e., at higher p_T regime for $y = 2$). However, this difference is obscured by the large theoretical uncertainties of R_{AA} due to the uncertainties of the determination of the nuclear parton distribution function (see Chapter 4). Moreover, this regime is close to the kinematical limit and might be beyond the scope of experimental measurements.

5.5 Collisional jet energy loss at the LHC (in 2D hydro)

In Chapter 4, we have presented a calculation of the nuclear modification factor R_{AA} for charged hadrons at the LHC. In this section, we will present the possible effect on our prediction of R_{AA} as a function p_T after incorporating the collisional energy loss. Again, we use a boost-invariant ideal hydrodynamic model with initial conditions calculated from perturbative QCD + saturation to describe the nuclear medium created at Pb+Pb collisions at $\sqrt{s_{NN}} = 5.5$ TeV [138, 167].

As has been illustrated in the last sections, the strong coupling constant α_s at

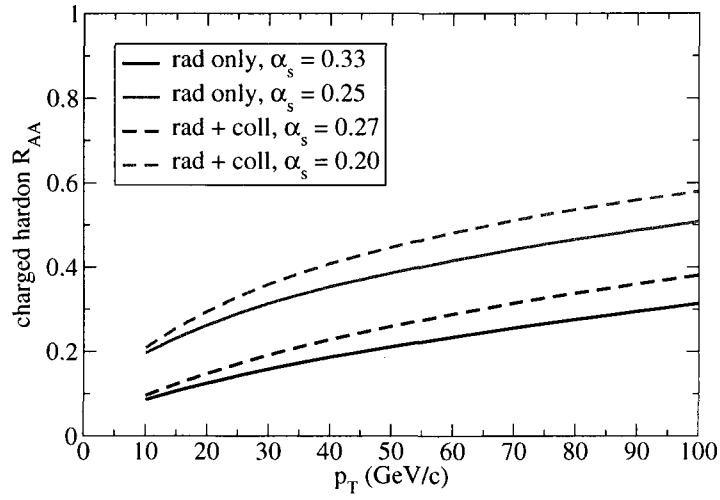

Figure 5.12: The p_T dependence of the nuclear modification factor R_{AA} for charged hadrons in central Pb+Pb collisions at mid-rapidity at the LHC.

RHIC is adjusted from $\alpha_s = 0.33$ to $\alpha_s = 0.27$ in order to describe the nuclear suppression factor R_{AA} in central Au+Au collisions at RHIC after the collisional energy loss is incorporated. The value will generate the lower bound of the prediction of R_{AA} at the LHC. The upper bound is obtained by setting the strongly coupling constant to be $\alpha_s = 0.20$ while the corresponding value for α_s from Chapter 4 with radiative energy loss only is taken to be $\alpha_s = 0.25$.

In Fig. 5.12, we compare the results for charged hadron R_{AA} in central Pb+Pb collisions at the LHC before and after we incorporate the collisional energy loss in the calculation. We observe that adding the collisional energy loss tends to increase the slope of the nuclear modification factor R_{AA} as a function of p_T. This effect might be measurable at the LHC.

5.6 Conclusions

We calculated collisional and radiative jet energy loss of hard partons in the hot and dense medium created at RHIC. We included the LPM effect for induced gluon emission and treated elastic collisions using a drag plus diffusion term reproducing the energy loss rate dE/dt and detailed balance. While we find that the additionally

induced average energy loss due to elastic collisions is small in comparison to the radiative one, the time evolution of the parton distributions $P(E,t)$ in both cases differ significantly. This is especially true for energies close to the initial parton energy. Since the initial parton spectrum is steeply falling, stronger differences in R_{AA} can result. We find that the inclusion of collisional energy loss significantly influences the quenching power quantified as the overall magnitude of neutral pion R_{AA} at RHIC, but that the shape as a function of p_T and the azimuth does not show a strong sensitivity.

6

Jet-tomography by studying the energy loss of photon-tagged jets

In this chapter, we study the photon-hadron correlations in Au+Au collisions at RHIC by incorporating all sources for the hard photons, including direct photons, fragmentation photons and jet-plasma photons [109]. The energy loss of photon-tagged jets traversing the medium is evaluated by consistently taking into account induced gluon radiation and elastic collisions. The hot and dense strongly interacting medium created in these collisions is modelled with (3+1)-dimensional relativistic hydrodynamics [137]. Our results for per-trigger yield of photon-tagged hadrons in both p+p and Au+Au collisions are consistent with the first experimental measurements. It is found that all photon sources are important to a full understanding of high z_T photon-hadron correlation studies at RHIC. Especially, the additional photon sources from jet-plasma interaction and fragmentation show significant contribution at the high p_T regime. We conclude that photon-tagged jets serve as additional probes of the interaction between high transverse momentum jets and the hot and dense medium created in relativistic heavy ion collisions.

6.1 Introduction

In Chapter 5, we have developed a consistent model to incorporate both collisional and radiative jet energy loss in the same formalism, and applied it to calculate the nuclear modification factor R_{AA} of hadrons in relativistic heavy ion collisions at RHIC. In this chapter, we continue and extend this effort by studying the correlations of back-to-back hard photon and jet.

As has been seen from earlier chapters, R_{AA} is a rather averaged quantity. The

final hadron spectrum is a convolution of the jet production cross section and the jet fragmentation functions. Therefore, the suppression of the produced hardons at a fixed p_T results from jet quenching with a wide range of initial transverse momenta. Furthermore, single jet measurements are also averaged with the nuclear overlap function accounting for the distribution of the initial hard vertices. It is therefore not particularly surprising that a wide variety of energy loss conjectures could agree with the measured R_{AA} in central Au+Au collisions at $\sqrt{s_{NN}} = 200$ GeV at RHIC.

In order to improve this situation, one may perform correlation measurements, i.e., the production of high p_T hadrons correlated with other high p_T trigger particles. One such suggested trigger is a hadron [140, 141]. But choosing a specific trigger p_T hadron does not yet confine the momentum of the away-side parton: the trigger hadron is produced by fragmentation of a parton that has also traversed the medium and lost energy.

Another promising trigger is a high p_T photon, i.e., to study jet-quenching by measuring the p_T distribution of hadrons in the opposite direction of a trigger direct photon [107, 108]. Since photons suffer no further interaction with the medium once they are produced, the momentum of the initial away-side parton before energy loss would be fixed at the direct photon's momentum. Thus photo-tagged jet may provide a calibrating probe for the study of the properties of high energy density QCD matter. There have been several theoretical studies performed along this direction [171, 172, 173].

However, all those calculations only focused on direct photons and neglected other important sources of photon production, such as fragmentation and jet-plasma interaction during or after jets traversing the plasma. As the initial away-side partonic jets could have bigger energies than the near-side trigger photon, photons produced from those processes might have significant contribution to the study of photon-hadron correlations. It is the purpose of the present work to incorporate all possible processes for hard photon production and study their relative contributions to the correlations between back-to-back hard photons and hadrons.

6.2 Hard photon production at RHIC

In Ref. [132, 174], the calculation of photon production from nuclear collisions at RHIC has been presented, by employing (1+1)-dimensional Bjorken evolution model and (2+1)-dimensional relativistic hydrodynamics to describe the hot and dense strongly interacting matter in those collisions, respectively. In this section, we present the calculation of hard photon production in the context of (3+1)-dimensional relativistic hydrodynamics for the description of the soft QCD matter.

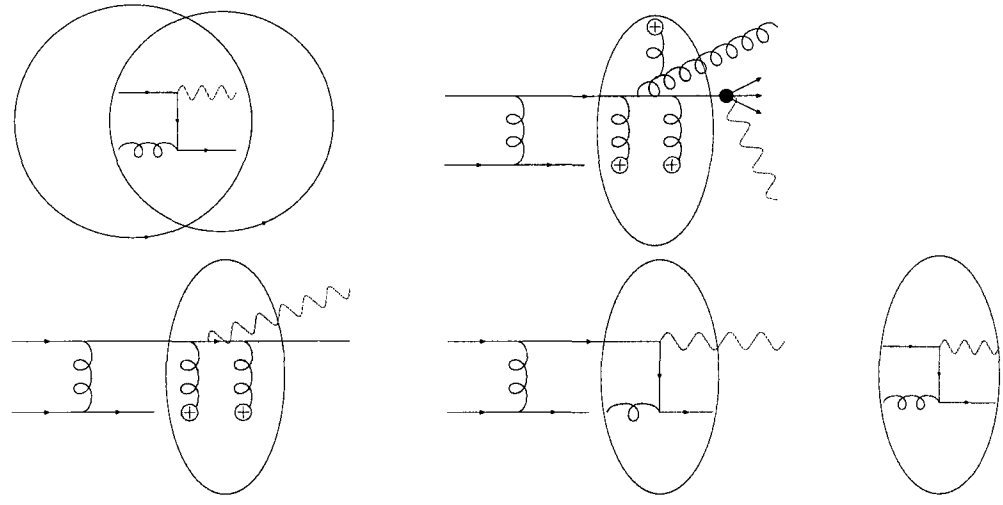

Figure 6.1: Photon production in relativistic heavy ion collisions from various sources: direct photons, fragmentation photons, bremsstrahlung photons, jet-conversion photons and thermal photons.

As is well known, photons produced in nuclear collisions may come from a variety of sources, namely direct photons, fragmentation photons, jet-plasma photons and thermal photons, as shown in Fig. 6.1. Direct photons are predominantly produced from hard collisions in the early stage of the relativistic heavy ion collisions, via quark-anti-quark annihilation ($q + \bar{q} \rightarrow g + \gamma$) and quark-gluon Compton scattering ($q(\bar{q}) + g \rightarrow q(\bar{q}) + \gamma$). Fragmentation photons are produced from the surviving high energy jets after their passing through the thermal medium. Jet-plasma photons are produced from the processes involving the interaction between jets and the surrounding medium when they are traversing through the plasma. Those include induced photon radiation (bremsstrahlung photons) and direct conversion from the high en-

ergy jets (conversion photons). It has been illustrated that those two processes are very important for the understanding the experimental data for photon production in Au+Au collisions at RHIC [132, 174, 114]. The thermal photon emission from quark-gluon plasma has negligible contribution at high p_T, and thus is excluded from consideration in the present work.

The inclusive direct photon cross section may be obtained from perturbative QCD calculations [113],

$$\frac{d\sigma^{\rm direct}_{A+B\to\gamma+X}}{d^2p_Tdy} = K\sum_{abd}\int dx_a G_{a/A}(x_a,Q)G_{b/B}(x_b,Q)\frac{1}{\pi}\frac{2x_ax_b}{2x_a-x_Te^y}\frac{d\sigma_{a+b\to\gamma+d}}{dt}, \quad (6.1)$$

with $x_T = 2p_T/\sqrt{s_{NN}}$, where $\sqrt{s_{NN}}$ is the center-of-mass energy. In the above equation, $G_{a/A}(x_a,Q)$ is the distribution function of parton a with momentum fraction x_a in the nucleus A at factorization scale Q, taken from CTEQ5 [155] including nuclear shadowing effects from EKS98 [156]. The distribution $d\sigma/dt$ is the leading order QCD differential cross section, and the K-factor accounts for next-to-leading order (NLO) effects. As for direct photon production, K-factor as a function of the transverse momentum of direct photon is obtained by employing the NLO calculation of photon production in p+p collisions [175, 176, 177], where the factorization scale Q is set to be the photon transverse momentum.

The above equation is applicable for the calculation of jet production resulting from corresponding QCD partonic processes. The fragmentation photon production is obtained by introducing the photon fragmentation function $D_{\gamma/j}(z,Q_F)$, where $z = p_T/p_T^j$ is the momentum fraction. The resulting expression is

$$\frac{d\sigma^{\rm frag}_{A+B\to\gamma+X}}{d^2p_Tdy} = \sum_j\int\frac{dz}{z^2}D_{\gamma/j}(z,Q_F)\frac{d\sigma_{A+B\to j+X}}{d^2p_T^jdy}. \quad (6.2)$$

Here the vacuum fragmentation functions of quarks and gluons into real photons are taken from Ref. [178]. The inclusive cross section for hadrons produced by fragmentation from nuclear collisions may calculated in a similar way by employing the above equation with appropriate hadron fragmentation function. To calculate the final photons and hadrons produced from fragmentation of hard jets, we need to fix

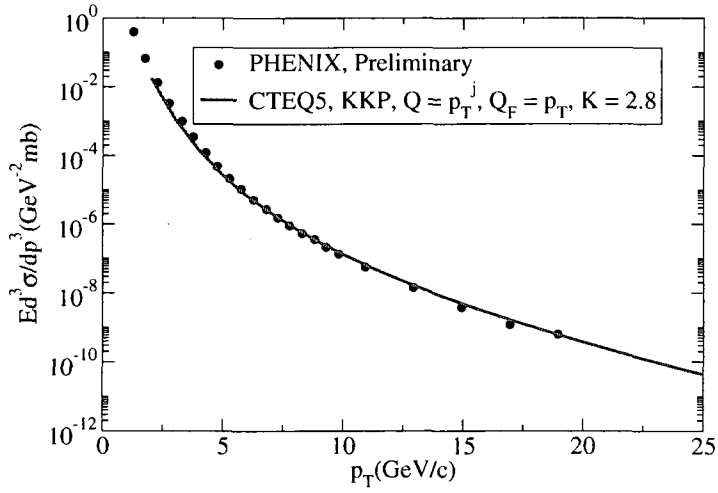

Figure 6.2: The inclusive cross section for π^0 production versus π^0 transverse momentum at mid-rapidity in pp collisions at $\sqrt{s_{NN}} = 200$ GeV, compared with PHENIX data.

K-factor in the calculation of initial jet cross section (and jet pair cross section used for fragmentation into photon-hadron pair in Eq. 6.14). If K-factor for the initial jet production (and jet pair production) is only dependent on the p_T of the jet, it should have the same value for fragmentation into photons and hadrons (as well as photon-hadron pairs). Here we fix K-factor following Ref. [138] by comparing the theoretical calculation of inclusive π^0 production at high p_T with the experimental measurements since fragmentation is the only mechanism for hadron production. In this way, K-factor is set to be 2.8 when the factorization scale Q is taken to be the transverse momentum of the initial jets, and the fragmentation scale Q_F is taken to be the transverse momentum of produced photon (or hadrons). By the above conventions, we can reproduce both the inclusive π^0 cross section (see Fig. 6.2) and the inclusive γ cross section in p+p collisions (see Fig. 6.3) at $\sqrt{s_{NN}} = 200$ GeV, where the data points are taken from [179, 180].

As for the production of fragmentation photons in Au+Au collisions at RHIC, we must include the energy loss of hard jets during their travelling through the thermal medium before fragmentation in vacuum. This is performed by taking into account both induced gluon radiation and elastic collisions during jet propagation. We may

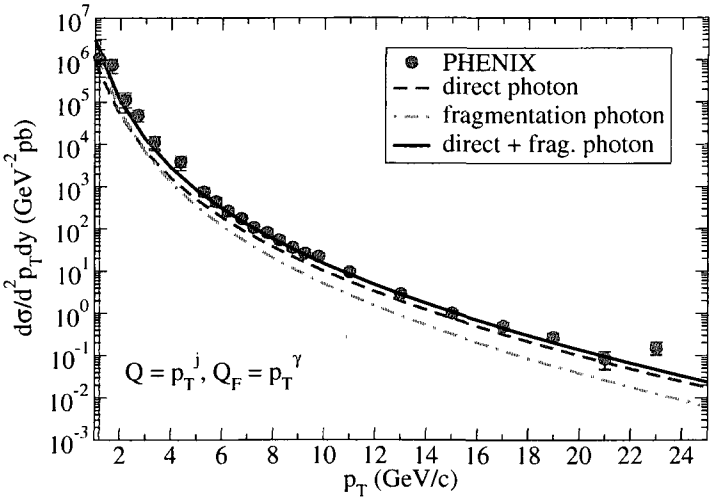

Figure 6.3: The photon production in 200 GeV p+p collisions at RHIC, compare with PHENIX data.

write the final spectrum of fragmentation photons as

$$\frac{d\sigma^{\rm frag}_{A+B\to\gamma+X}}{d^2p_T dy} = \frac{1}{2\pi}\int d^2\vec{r}_\perp \mathcal{P}_{AB}(\vec{r}_\perp)\sum_j \int \frac{dz}{z^2}\tilde{D}_{\gamma/j}(z,\vec{r}_\perp,\phi)\frac{d\sigma_{A+B\to j+X}}{d^2p_T^j dy}, \qquad (6.3)$$

where $\mathcal{P}_{AB}(\vec{r}_\perp)$ is the probability distribution of initial hard jets in the transverse position $\vec{r}_\perp$, and $\tilde{D}_{\gamma/j}(z,\vec{r}_\perp,\phi)$ is the medium-modified fragmentation function for a single jet initially created at transverse position $\vec{r}_\perp$ and propagating at azimuthal angle ϕ in the transverse plane.

As for A+B collisions at impact parameter b, the probability distribution $\mathcal{P}_{AB}(b,\vec{r}_\perp)$ of initial hard jets at $\vec{r}_\perp$ in the transverse plane is determined by the overlap geometry of two nuclei in the reaction zone,

$$\mathcal{P}_{AB}(b,\vec{r}_\perp) = \frac{T_A(\vec{r}_\perp+\vec{b}/2)T_B(\vec{r}_\perp-\vec{b}/2)}{T_{AB}(b)}, \qquad (6.4)$$

where $T_A(\vec{r}_\perp) = \int dz\rho_A(\vec{r}_\perp,z)$ and $T_{AB}(b) = \int d^2r_\perp T_A(\vec{r}_\perp)T_B(\vec{r}_\perp+\vec{b})$ are nuclear thickness function and overlap function of two nuclei, respectively. Here we use a Woods-Saxon form for the nuclear density function $\rho(\vec{r}_\perp,z) = \rho_0/[1+\exp(\frac{r-R}{d})]$. The values of the parameters $R = 6.38$ fm and $d = 0.535$ fm are taken from [63].

The medium-modified fragmentation function $\tilde{D}_{\gamma/j}(z,\vec{r}_\perp,\phi)$ for a single jet is re-

lated to the vacuum fragmentation function $D_{\gamma/j}(z)$ by,

$$\tilde{D}_{\gamma/j}(z,\vec{r}_\perp,\phi)=\sum_{j'}\int dp_{j'}\frac{z'}{z}D_{\gamma/j'}(z')P(p_{j'}|p_j,\vec{r}_\perp,\phi). \tag{6.5}$$

where $z=p_\gamma/p_j$ and $z'=p_\gamma/p_{j'}$ are two momentum fractions, and the sum overs j' is the sum over all parton species. In the above equation, the probability function $P(p_{j'}|p_j,\vec{r}_\perp,\phi)$ contains the information about the energy loss of hard jets during their propagation in the medium. It represents the probability of obtaining a jet j' with momentum $p_{j'}$ from a given jet j with momentum p_j initially created at $\vec{r}_\perp$ and propagating at ϕ direction in the transverse plane.

We have already seen, in Chapter 3, 4 and 5, the evolution of jet momentum distribution $P(E,t)=dN(E,t)/dE$ in the medium is determined by a set of coupled Fokker-Planck type rate equations with the following generic form,

$$\frac{dP_j(E,t)}{dt}=\sum_{ab}\int d\omega\left[P_a(E+\omega,t)\frac{d\Gamma_{a\to j}(E+\omega,\omega)}{d\omega dt}-P_j(E,t)\frac{d\Gamma_{j\to b}(E,\omega)}{d\omega dt}\right], \tag{6.6}$$

where $d\Gamma^{j\to a}(E,\omega)/d\omega dt$ is the transition rate for the partonic process $j\to a$, with ω the lost energy in the process. The $\omega<0$ part of the integration incorporates processes which increase a particle's energy. The radiative and collisional parts of the transition rates have been discussed in Chapter 3 and Chapter 5, respectively.

Now we present the calculation of photons produced from jet-plasma interaction when jets are propagating through the hot and dense medium. Those processes may be incorporated by solving an additional evolution equation for photons,

$$\frac{dP_\gamma^{\text{jet-plasma}}(E,t)}{dt}=\int d\omega P_{q\bar{q}}(E+\omega,t)\left(\frac{d\Gamma_{q\to\gamma}^{\text{brem}}(E+\omega,\omega)}{d\omega dt}+\frac{d\Gamma_{q\to\gamma}^{\text{conv}}(E+\omega,\omega)}{d\omega dt}\right). \tag{6.7}$$

In the above equation, $d\Gamma_{q\to\gamma}^{\text{brem}}/d\omega dt$ are transition rates for photon bremsstrahlung processes, which has been discussed in Chapter 3. The transition rates $d\Gamma_{q\to\gamma}^{\text{conv}}/d\omega dt$ for $2\to 2$ jet-photon conversion processes may be inferred from the photon emission rates in those processes.

If we define the photon emission rate per unit volume $R_\gamma=dN_\gamma/d^3xdt$, the final result of photon emission rate from $2\to 2$ processes is given by [75, 93, 94, 95] (also

see Chapter 3),

$$\frac{(2\pi)^3 dR_\gamma^{2\to 2}}{d^3k} = \sum_f \left(\frac{e_f}{e}\right)^2 \frac{8\pi\alpha_e\alpha_s T^2}{k} f_{q\bar{q}}(k) \left(\frac{1}{2}\ln\frac{kT}{m_q^2} + C_{2\to 2}(k/T)\right), \tag{6.8}$$

where m_q is the thermal quark mass, $m_q^2 = g_s^2 T^2/6$. In the limit of $k \gg T$, $C_{2\to 2}(k/T) = -0.36149$ is a constant, and $f_{q\bar{q}}(k) = (2\pi)^3/d_{q\bar{q}} \cdot dN_{q\bar{q}}(k)/d^3k d^3x$ is the phase-space distribution of quark plus anti-quark jets, with the spin and color degeneracy $d_{q\bar{q}} = 2 \cdot 2 \cdot 3 = 12$. As long as we know the local phase-space distribution of quark plus anti-quark jets, we may obtain the local phase-space distribution of photons produced from these jets by conversion. By integrating over the space-time, we will obtain the spectra of the photons produced from those processes. As $2 \to 2$ processes are dominated by t-channel diagrams, the produced photon will have almost the same energy as incoming jet. Thus the differential conversion rate from a quark (or anti-quark) to a photon is given by

$$\frac{d\Gamma_{q\to\gamma}^{\rm conv}(E,\omega)}{d\omega dt} = \sum_f \left(\frac{e_f}{e}\right)^2 \frac{2\pi\alpha_e\alpha_s T^2}{3E} \left(\frac{1}{2}\ln\frac{ET}{m_q^2} + C_{2\to 2}(E/T)\right)\delta(\omega). \tag{6.9}$$

The δ function generates the constraint that the incoming quark (or anti-quarks) experiences no energy loss in the conversion processes [1].

Putting all together, we obtain the total yield of photon production in nuclear collisions,

$$\frac{dN_{AB}^\gamma(b)}{d^2p_T dy} = \frac{N_{\rm coll}(b)}{\sigma_{NN}} \frac{d\sigma_{A+B\to\gamma+X}}{d^2p_T dy} \tag{6.10}$$

where $N_{\rm coll}$ is the number of binary collisions and the σ_{NN} is the inelastic cross section of elementary nucleon-nucleon collisions.

In Fig. 6.4, we show the photon production from different channels in most central 0-10% Au+Au collisions ($b = 2.4$ fm) at RHIC, where the number of binary collisions is taken to be $\langle N_{\rm coll}\rangle = 955$ [61, 181, 182]. Data points are taken from PHENIX [183]. The direct photon from the initial hard collisions of partons from two

[1] In the numerical computation, we discretize the evolution equation such that $\int d\omega \to \Delta_\omega \sum_{\omega=n\Delta_\omega}$ and use the approximation $\delta(\omega) \approx \frac{1}{2}[\delta(\omega-\Delta_\omega) + \delta(\omega+\Delta_\omega)]$ for small Δ_ω.

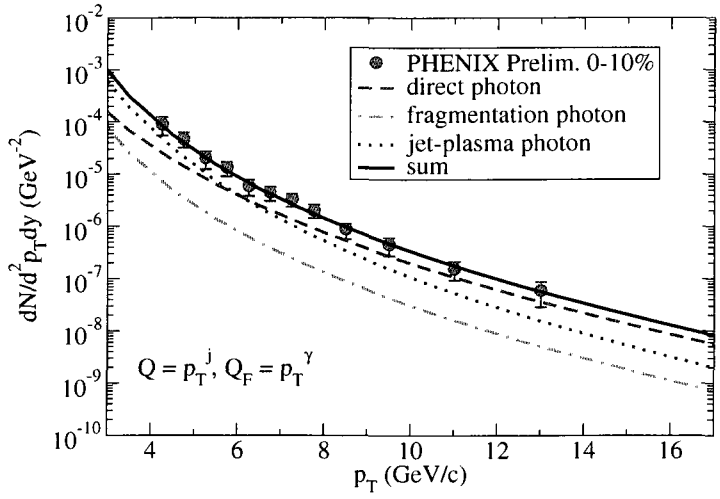

Figure 6.4: The contributions from different channels to the photon production in Au+Au collisions at RHIC for $b = 2.4$ fm compared with most 0-10% PHENIX data.

nuclei is the most dominant mechanism for photon production at very high p_T regime ($p_T > 7$ GeV). At intermediate p_T regime ($p_T \approx 3 - 6$ GeV), jet-plasma interaction gives very significant contribution to the photon production. The thermal photon is expected to be dominant at very low p_T regime ($p_T < 2$ GeV, not shown) [132, 174]. After summing over all photon production channels, our calculation agrees with the experimental measurements well. We may observe that the presence of the jet-plasma interaction is important to understand the total photon yield in Au+Au collisions at RHIC.

Photon R_{AA} is another quantity to measure the effect of the nuclear medium on the photon production. In Fig. 6.5, the photon R_{AA} is shown as a function of photon p_T for most central Au+Au collisions ($b = 2.4$ fm) at RHIC compared with 0-10% PHENIX data. As p_T is increased, the experimental data points seem to decrease, consistent with the theoretical curve. At lower p_T region, the theoretical curve is increasing due to the presence of plasma effect in Au+Au collisions, but not in p+p collisions (compare Fig. 6.3 and Fig. 6.4). However, the experimental error bars are too large to allow a strong judgement on this observation.

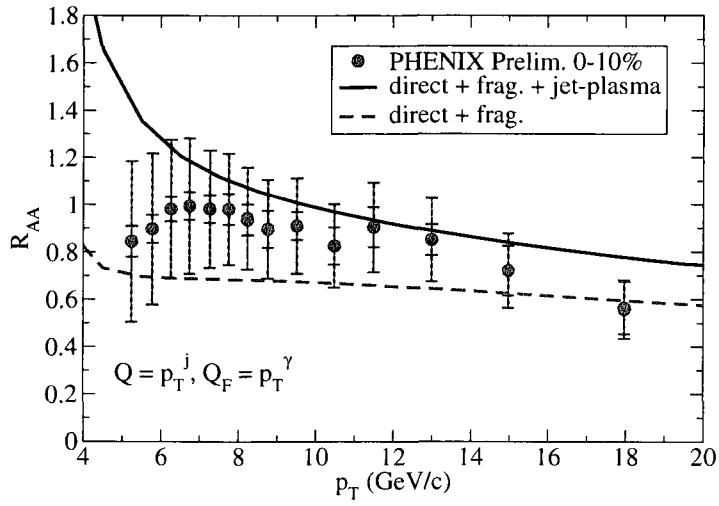

Figure 6.5: The nuclear modification factor R_{AA} for photon in Au+Au collisions at RHIC for $b = 2.4$ fm compared with most 0-10% PHENIX data.

6.3 Photon-hadron correlations in QGP

In this section, we will present the calculation of the correlations between back-to-back hard photons and hadrons in Au+Au collisions at RHIC. The hadron production in Au+Au collisions in the AMY formalism has been elaborated in Chapter 4 and Chapter 5, and the photon production has been discussed in the last section as well as in Ref. [132, 174]. The technique presented here is applicable for back-to-back hadron-hadron correlations by replacing the trigger photon with a trigger hadron. The near-side hadron-hadron correlations may also be studied similarly if we assume both the triggered and associated hadrons are produced from the fragmentation of the same jets.

One of the commonly exploited observables in correlation studies is the (differential) yield per trigger $P(p_T^h|p_T^\gamma,\phi) = 1/N_\gamma dN_{h+\gamma}(p_T^h|p_T^\gamma,\phi)/dp_T^h$, which gives the conditional probability of producing a hadron with momentum p_T^h in the away side given a trigger photon with momentum p_T^γ in the near side at an azimuthal angle ϕ in the transverse plane. From probability theory

$$P(p_T^h|p_T^\gamma,\phi) = \frac{P(p_T^h,p_T^\gamma,\phi)}{P(p_T^\gamma,\phi)}, \tag{6.11}$$

where the two-particle jointed probability and single-particle probability are related to the two-particle to single-particle cross sections,

$$P(p_T^\gamma,\phi)=\frac{1}{N_{\rm evts}}\int dy_\gamma\frac{dN_\gamma(p_T^\gamma,\phi)}{dy_\gamma dp_T^\gamma d\phi}=\frac{1}{\sigma_{\rm tot}}\int dy_\gamma\frac{d\sigma_\gamma(p_T^\gamma,\phi)}{dy_\gamma dp_T^\gamma d\phi},$$
$$P(p_T^h,p_T^\gamma,\phi)=\frac{1}{N_{\rm evts}}\int dy_h dy_\gamma\frac{dN_{h+\gamma}(p_T^h,p_T^\gamma,\phi)}{dy_h dy_\gamma dp_T^h dp_T^\gamma d\phi}=\frac{1}{\sigma_{\rm tot}}\int dy_h dy_\gamma\frac{d\sigma_{h+\gamma}(p_T^h,p_T^\gamma,\phi)}{dy_h dy_\gamma dp_T^h dp_T^\gamma d\phi}, \tag{6.12}$$

where $N_{\rm evts}$ is the number of events and $\sigma_{\rm tot}$ is the semi-inclusive cross section for that event sample. Then we obtain

$$P(p_T^h|p_T^\gamma,\phi)=\int dy_h dy_\gamma\frac{d\sigma_{h+\gamma}(p_T^h,p_T^\gamma,\phi)}{dy_h dy_\gamma dp_T^h dp_T^\gamma d\phi}\Big/\int dy_\gamma\frac{d\sigma_\gamma(p_T^\gamma,\phi)}{dy_\gamma dp_T^\gamma d\phi} \tag{6.13}$$

Notice that the yield per trigger has a strong dependence on the associated hadron rapidity y_h range (and a weak dependence on the trigger photon rapidity y_γ range due to the cancellation between the numerator and the denominator). Unless otherwise stated, in the following, all results on photon-hadron correlations are presented at mid-rapidity, which corresponds to setting $-0.5 < y_h, y_\gamma < 0.5$ in the calculation.

As for the fragmentation process, since the back-to-back hard photon and hadron are produced from a pair of back-to-back jets, we obtain,

$$P(p_T^\gamma,\phi)=\frac{1}{2\pi}\int d^2\vec{r}_\perp\mathcal{P}_{AB}(\vec{r}_\perp)\sum_j\int dp_T^j P_j(p_T^j)P(p_T^\gamma|p_T^j,\vec{r}_\perp,\phi),$$
$$P(p_T^h,p_T^\gamma,\phi)=\frac{1}{2\pi}\int d^2\vec{r}_\perp\mathcal{P}_{AB}(\vec{r}_\perp)$$
$$\times\sum_{jj'}\int dp_T^j dp_T^{j'}P_{j+j'}(p_T^j,p_T^{j'})P(p_T^\gamma|p_T^j,\vec{r}_\perp,\phi)P(p_T^h|p_T^{j'},\vec{r}_\perp,\pi+\phi). \tag{6.14}$$

In the above equation, $P_j(p_T^j)=\int dy_j d\sigma_j(p_T^j)/\sigma_{\rm tot}dy_j dp_T^j$ is the single-particle cross section of hard jets, and $P_{j+j'}(p_T^j,p_T^{j'})=\int dy_j dy_{j'}d\sigma_{j+j'}(p_T^j,p_T^{j'})/\sigma_{\rm tot}dy_j dy_{j'}dp_T^j dp_T^{j'}$ is the two-particle cross section of hard back-to-back jets. Those cross sections may be calculated from pQCD as described in the previous section. $P(p_T^\gamma|p_T^j,\vec{r}_\perp,\phi)$ ($P(p_T^h|p_T^j,\vec{r}_\perp,\phi)$) is photon (hadron) yield per trigger jet, giving the conditional probability of producing a photon (hadron) with momentum p_T^γ (p_T^h) from a jet with momentum p_T^j initially created at $\vec{r}$ and propagating in the ϕ direction in the transverse plane. To derive the above equation, we have assumed no correlation between

the individual evolutions of two partonic jets once they are produced. As has been described in previous sections, the evolution of the jet momentum distribution in the thermalized medium is controlled by a set of coupled Fokker-Planck equations,. Therefore, the photon yield per trigger jet is given by,

$$P(p_T^\gamma|p_T^j,\vec{r}_\perp,\phi) = \sum_{j'}\int dp_T^{j'} P(p_T^\gamma|p_T^{j'})P(p_T^{j'}|p_T^j,\vec{r}_\perp,\phi). \tag{6.15}$$

As for fragmentation process, the photon yield per trigger jet is related to medium-modified photon fragmentation function by

$$\tilde{D}_{\gamma/j}(z,\vec{r}_\perp,\phi) = p_T^j P(p_T^\gamma|p_T^j,\vec{r}_\perp,\phi), \quad D_{\gamma/j'}(z') = p_T^{j'} P(p_T^\gamma|p_T^{j'}), \tag{6.16}$$

where $z = p_T^\gamma/p_T^j$ and $z' = p_T^\gamma/p_T^{j'}$. At this point, Eq. (6.15) is equivalent to Eq. (6.5). The quantity I_{AA} is defined as the ratio of yield per trigger in A+A collisions to that in p+p collisions,

$$I_{AA}(p_T^h|p_T^\gamma,\phi) = \frac{P_{AA}(p_T^h|p_T^\gamma,\phi)}{P_{pp}(p_T^h|p_T^\gamma)}. \tag{6.17}$$

As is well known, photon-hadron correlations have been proposed as a calibrated probe of medium-modified fragmentation function since the momenta of away-side hadron are fixed by the trigger photons if we are capable of triggering direct photons at leading order. Thus, it is often useful to define the photon-triggered fragmentation function as [184, 185],

$$D_{AA}(z_T,p_T^\gamma,\phi) = \int dy_h dy_\gamma \frac{d\sigma_{h+\gamma}(p_T^h,p_T^\gamma,\phi)}{dy_h dy_\gamma dz_T dp_T^\gamma d\phi} \Big/ \int dy_\gamma \frac{d\sigma_\gamma(p_T^\gamma,\phi)}{dy_\gamma dp_T^\gamma d\phi}, \tag{6.18}$$

where $z_T = p_T^h/p_T^\gamma$. The yield per trigger is related to the photon-triggered fragmentation function as, $D_{AA}(z,p_T^\gamma,\phi) = p_T^\gamma P_{AA}(p_T^h|p_T^\gamma,\phi)$. Thus I_{AA} may be written as the ratio of inclusive fragmentation function in A+A collisions to that in p+p collisions,

$$I_{AA}(p_T^h|p_T^\gamma,\phi) = \frac{D_{AA}(z_T,p_T^\gamma,\phi)}{D_{pp}(z_T,p_T^\gamma)}. \tag{6.19}$$

The above equations were derived by assuming that photons and hadrons are coming from fragmentation of back-to-back jets. This is true for high p_T hadron production, and other hadronization mechanisms, such as the recombination of partons,

will be excluded for consideration here, as they assumes significance only in the lower p_T region [154]. As for high p_T photon production, we have to include all relevant photon production sources.

$$P(p_T^\gamma|p_T^j,\vec{r}_\perp,\phi) = \sum_{\rm src} P(p_T^\gamma,{\rm src}|p_T^j,\vec{r}_\perp,\phi), \tag{6.20}$$

where the sources include direct photons, fragmentation photons and jet-plasma photons. As for direct photon contribution, we may simply write the probability function (photon yield per trigger jet) as $P(p_T^\gamma,{\rm direct}|p_T^j,\vec{r}_\perp,\phi) = \delta(p_T^\gamma - p_T^j)$ since the direct photon and the away-side jet have the same momentum at the production time. To include the production of jet-plasma photons, we may obtain the probability function $P(p_T^\gamma,{\rm jet\text{–}plasma}|p_T^j,\vec{r}_\perp,\phi)$ by solving the photon evolution equation Eq. (6.7).

6.4 Results

In this section, the numerical results for the correlations between back-to-back photons and hadrons will be presented at high p_T. The product of the initial hard parton densities is determined from the overlap geometry between two nuclei in the transverse plane of the collision zone. The initial momentum distribution of hard jets is computed from perturbative QCD. The energy loss of hard jets is computed by taking into account both induced gluon radiation and elastic collisions in the hot the dense medium. The production of trigger photons at high p_T regime is obtained by taking into account all possible sources for hard photons, and the production of associated hadrons is calculated from the fragmentation of jets after their passing through the thermal plasma. The bulk properties of the medium created in Au+Au collision at RHIC is described by (3+1)-dimensional relativistic ideal hydrodynamics [137], which has been shown to give a good description of bulk properties at RHIC.

In Fig. 6.6, we show the integrated per-trigger yield of away-side hadrons as a function of the trigger photon momenta in p+p collisions at RHIC, compared with the experimental data from PHENIX [186] for two different hadron momentum regimes: $p_T^h = 2-3$ GeV and $3-5$ GeV. We may observe that our theoretical calculations can qualitatively describe the experimental measurements of photon-hadron correlations

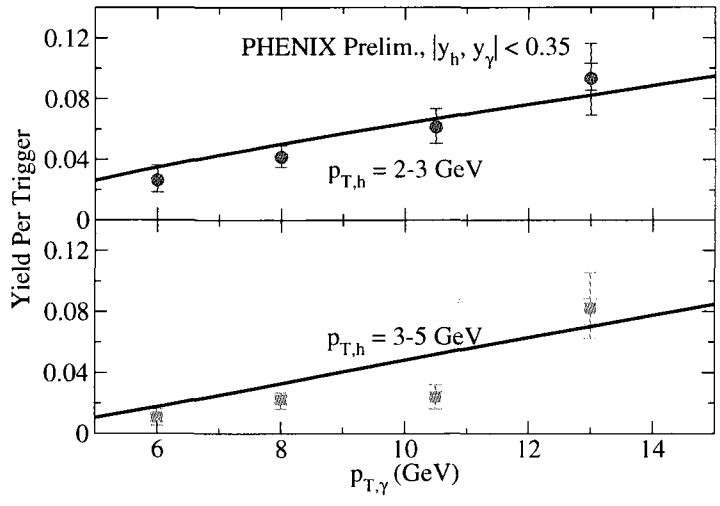

Figure 6.6: The integrated per-trigger yield of away-side hadrons as a function of the momenta of trigger photons in p+p collisions at RHIC.

in p+p collisions. The per-trigger yield is smaller in the lower panel ($p_T^h = 3 - 5$ GeV) for a given trigger photon momentum. This can be easily understood because associated hadrons with larger momenta have larger momentum fraction z_T. It should be noted that in these regimes, fragmentation may not be the only mechanism for the hadron production, especially for $p_T^h = 2 - 3$ GeV.

In Fig. 6.7, the photon-triggered fragmentation function $D_{pp}(z_T)$ is shown as a function of hadron momentum fraction z_T in p+p collisions at RHIC. We show the photon-triggered fragmentation function for three different regimes for away-side hadrons: $p_T^h = 3 - 5$ GeV, $5 - 7$ GeV and $7 - 9$ GeV. The experimental data are from PHENIX [187]. Here, we have chosen those data points with hadron p_T greater than 3 GeV as hadrons with small p_T might not produced from fragmentation. As can be clearly seen from the figure, the theoretical curves are in good agreement with the experimental data. Also, a slight difference is observed for the slope of photon-triggered fragmentation function $D_{pp}(z_T)$ for different associated hadron momenta. This difference may be traced back to the momentum (fraction) dependence of different parton distribution functions (PDF). As is well known, gluon PDF has a deeper slope than quark PDF as a function of momentum fraction. As we increase

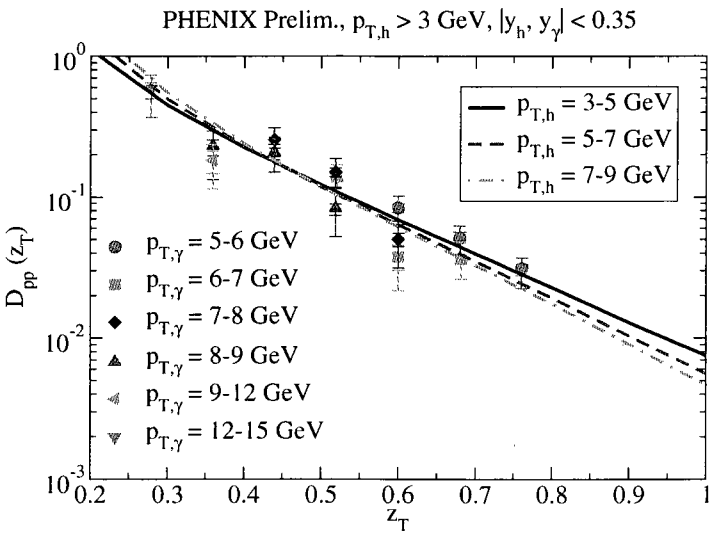

Figure 6.7: The photon-triggered hadron fragmentation function as a function of momentum fraction z_T in p+p collisions at RHIC.

the momenta of initial partons (thus the momentum fraction in PDF), more quarks appear in the initial state. As a result, more gluons will be obtained in the final state after partonic scatterings. Since photon-triggered fragmentation function $D_{pp}(z_T)$ is a weighted average over quark and gluon fragmentation functions weighted with their fractions, a deeper slope is expected for photon-triggered $D_{pp}(z_T)$ since gluon fragmentation function is deeper than quark fragmentation function. But it seems that the current experimental data are not able to resolve this difference.

We now turn to study photon-hadron correlations in Au+Au collisions. In Fig. 6.8, we show photon-triggered fragmentation function $D_{AA}(z_T)$ as a function of hadron momentum fraction z_T when we trigger photons in the near side with momenta $p_T^\gamma = 8 - 16$ GeV in central Au+Au collisions ($b = 2.4$ GeV) at RHIC. The data points are taken from STAR for both central (0-10%) and peripheral (40-80%) Au+Au collisions [188]. We may observe that the theoretical curve of photon-triggered fragmentation function $D_{AA}(z_T)$ in centrral Au+Au collisions agrees with experimental data quite well. We also compare the photon-triggered fragmentation $D_{pp}(z_T)$ in p+p collisions with the data for peripheral Au+Au collisions, and they are in good agreement.

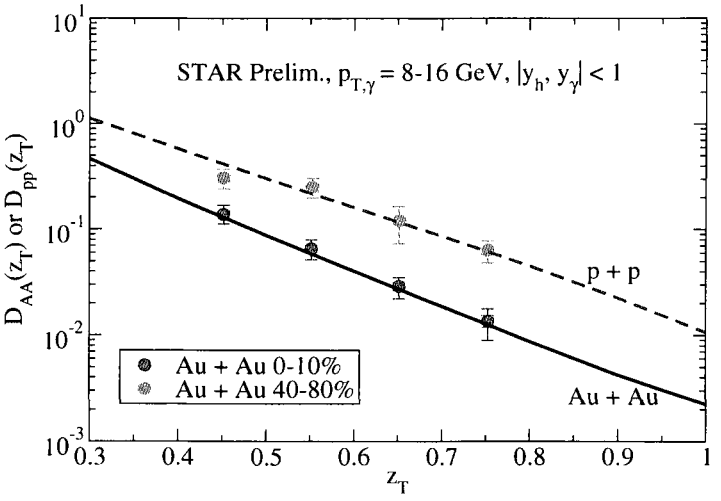

Figure 6.8: The photon-triggered fragmentation functions as a function of momentum fraction z_T in central Au+Au collisions and p+p collisions (peripheral Au+Au collisions) at RHIC.

Note that STAR has tried to remove the contribution from fragmentation photons by employing isolation cut method.

In the above plots, we have shown our calculation of the photon-hadron correlations a function of hadron transverse momentum fraction z_T for p+p collisions and most central Au+Au collisions. For Au+Au collisions, it would be interesting to study the centrality dependence of photon-hadron correlations by integrating out the transverse momenta for both triggered photons and associated hadrons. In Fig. 6.9, we show our numerical calculation of the centrality dependence of per-trigger yield of photon-tagged hadrons in Au+Au collisions at RHIC and compared the experimental measurements from STAR [188]. We compare the per-trigger yield for four different impact parameters, $b = 2.4$ fm, $b = 4.5$ fm, $b = 6.3$ fm and $b = 7.5$ fm. In the plot, we trigger photons in the near side with momenta $p_T^\gamma = 8 - 16$ GeV, and study away-side hadrons with momenta $p_T^h = 4 - 6$ GeV and $6 - 8$ GeV. We may observe that the theoretical calculations of per-trigger yield for photon-triggered hadrons are consistent with the experimental measurements. It is noted that we do not perform the calculation for very peripheral Au+Au collisions as the assumption of a thermalized medium essential for a hydrodynamical treatment is no longer fulfilled.

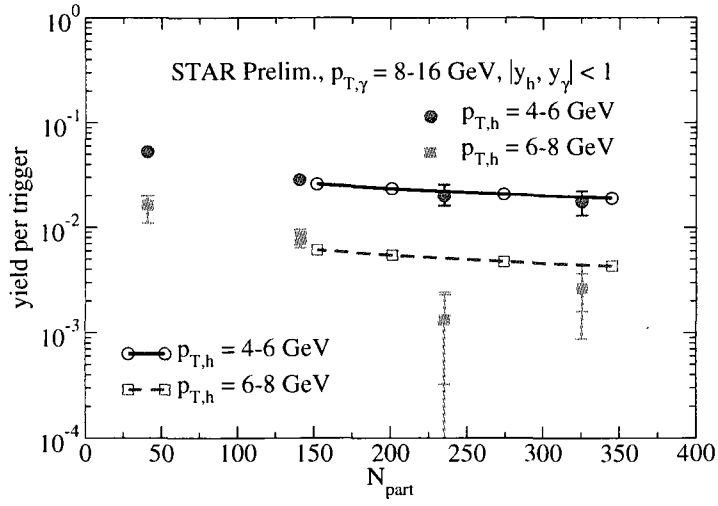

Figure 6.9: The per-trigger yield for photon-tagged hadrons in Au+A collisions at RHIC as a function of centrality. The four points in each theoretical curve correspond to four impact parameters, $b = 2.4$ fm , $b = 4.5$ fm, $b = 6.3$ fm and $b = 7.5$ fm.

The above numerical results for photon-hadron correlations have been shown by taking into account all possible sources of high p_T photons, including direct photons, fragmentation photons and jet-plasma photons. It would be highly interesting to study how different sources of photons contribute the final photon-hadron correlations. In order to address this issue, it is useful to study the momentum correlations between the initial back-to-back partonic jets and the trigger photon. Given a trigger photon produced in the near side, the momentum probability distribution of initial partonic jets at production time is given by,

$$P(p_T^j|p_T^\gamma,\phi) = \frac{\sum_{\rm src} P(p_T^\gamma, p_T^j, \phi, {\rm src})}{P(p_T^\gamma,\phi)}, \tag{6.21}$$

where $P(p_T^\gamma, p_T^j, \phi, {\rm src})$ is the two-particle momentum distribution of ,

$$P(p_T^\gamma, p_T^j, \phi, {\rm src}) = \frac{1}{2\pi}\int d^2\vec{r}_\perp \mathcal{P}_{AB}(\vec{r}_\perp) P(p_T^j) P(p_T^\gamma, {\rm src}|p_T^j, \vec{r}_\perp, \phi). \tag{6.22}$$

In the above equation, we have performed the medium average for the initial jet as we have no knowledge about where the jets are originally created in the traverse plane of the medium.

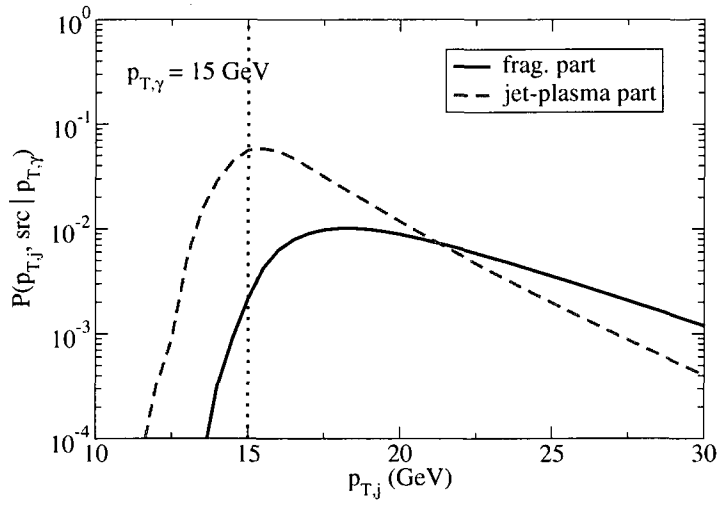

Figure 6.10: The contributions from fragmentation photon and jet-plasma photon parts to the initial jet momentum distribution at the production time when we trigger a photon with momentum p_T^γ = 15 GeV in most central Au+Au collisions (b = 2.4 fm) at RHIC. The contribution from direct photon part is a delta function with certain normalization constant at 15 GeV. The total distributions of quarks and gluons will be the sum of the contributions from those three parts (not shown).

In order to study the various contributions from different sources of high p_T photons to the total initial jet momentum distribution, we rewrite Eq. (6.21) as the sum of different parts, each tagged by a specific source of photons,

$$P(p_T^j|p_T^\gamma,\phi) = \sum_{\mathrm{src}} P(p_T^j, \mathrm{src}|p_T^\gamma,\phi). \tag{6.23}$$

In Fig. 6.10, we show the function $P(p_T^j, \mathrm{src}|p_T^\gamma)$ for different sources of photons. In the plot, we trigger a photon with momentum p_T^γ = 15 GeV, thus the probability distribution of jets tagged by direct photons is a δ function with some normalization weight determined by the fraction of direct photons to total photons at 15 GeV. In the plot, we show the distribution of jets (quarks plus gluons) tagged by those photons produced from fragmentation and jet-plasma interaction. It may be clearly seen that the initial jets may have higher momenta than the trigger photon. Jets tagged by fragmentation photons dominate at high momentum regime, while jets tagged by jet-plasma photons is prevalent at relatively lower momentum regime except at 15 GeV, where the jets are predominantly tagged by direct photons. Note that the initial

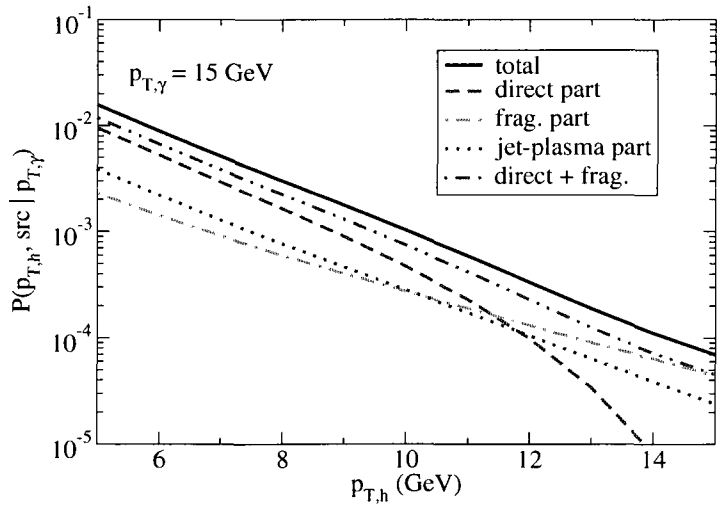

Figure 6.11: Different contributions to per-trigger yield of the away-side hadrons when we trigger a photon with momentum $p_T^\gamma = 15$ GeV in most central Au+Au collisions ($b = 2.4$ fm) at RHIC.

jets could have lower momenta than the trigger photon since we also include the absorption processes during the jet evolution in medium (see Fig. 5.4).

By applying the fragmentation function, we may also study how different parts of jet initial distribution contribute to the away-side hadron production after their passing through the medium. Similarly, we break the hadron yield per trigger into different parts associated with different photon sources,

$$P(p_T^h|p_T^\gamma,\phi) = \sum_{\mathrm{src}} P(p_T^h, \mathrm{src}|p_T^\gamma,\phi). \tag{6.24}$$

In Fig. 6.11, we show the function $P(p_T^h, \mathrm{src}|p_T^\gamma)$ for different sources of high p_T photons. As we trigger a photon in the near side, the away-side hadrons at relatively lower p_T regime is mostly produced from those jets tagged by direct photons, while at higher p_T regime, a large amount of away-side hadrons come from those jets tagged by jet-plasma photons and fragmentation photons. Especially, close to the trigger photon momentum, the away side hadron production is dominated by those jets tagged by fragmentation photons.

To further study the various contributions from different sources of photons to the photon-hadron correlations, we may consider comparing the following three scenarios:

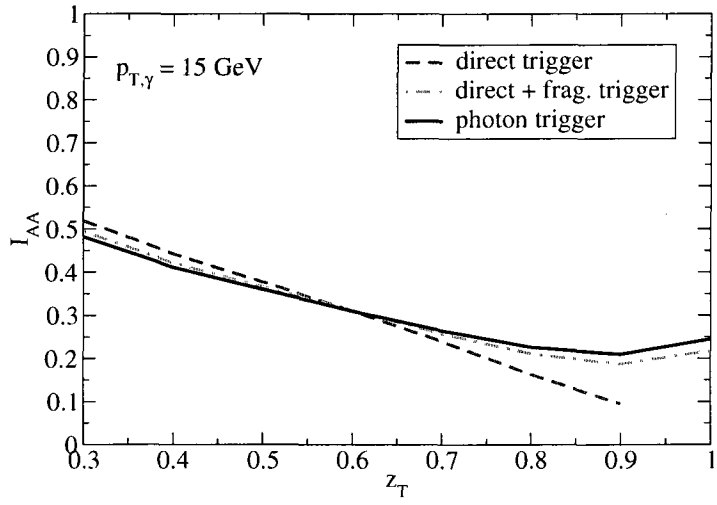

Figure 6.12: Photon-triggered I_{AA} for hadrons as a function of momentum fraction z_T in central Au+A collisions ($b = 2.4$ fm) at RHIC.

(1) only direct photons in both p+p and A+A collisions; (2) including direct and fragmentation photons in both p+p and A+A collisions, but no jet-plasma photons in A+A collisions; (3) including all possible sources of high p_T photons. One of the important reasons for studying jet-photon correlations is that the original away-side jet has a single transverse momentum fixed by the near-side tagged photon if we could trigger direct photons at leading order; this corresponds to case (1). As has been discussed, jet-plasma photons are very important for the understanding of the experimental measurements of total photon yield in Au+Au collisions at RHIC. It would be interesting to quantify their effect on jet-photon correlations, which will be investigated by comparing case (2) and (3).

In Fig. 6.12, we compare I_{AA} for photon-triggered hadron production in these three different scenarios, where the momenta of the triggered photons are chosen to be $p_T^\gamma = 15$ GeV. As expected, I_{AA} is a falling function of momentum fraction z_T if we only consider direct photon production in both p+p and Au+Au collisions. As we include fragmentation photons for both p+p and Au+Au collisions, I_{AA} is significantly enhanced at much higher z_T regime. Especially, close to the trigger photon momentum ($z_T = 1$), we observe a small rising of I_{AA} as a function of z_T. This

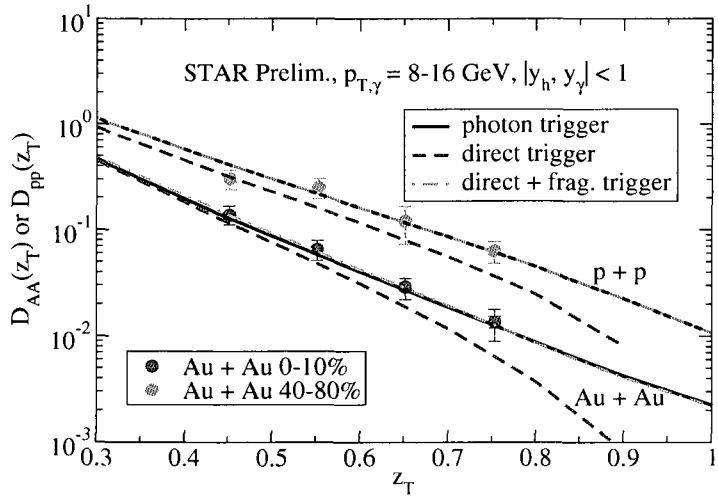

Figure 6.13: The photon-triggered hadron fragmentation functions as a function of momentum fraction z_T in p+p collisions and Au+Au collisions at RHIC.

is because those hadrons close to the trigger photon momenta are mostly produced from the jets tagged by the fragmentation photons. In this case, the initial jets tend to have higher momentum than the trigger photon (see Fig. 6.10 and Fig. 6.11). When we incorporate jet-plasma photons in Au+Au collisions, an overall change of I_{AA} is observed for hadron in all z_T range explored. This is because jets tagged by jet-plasma photons have sizeable contributions to all p_T hadron production in Au+Au collisions (see Fig. 6.11), while no jet-plasma interaction is present in p+p collisions.

It would be interesting to see whether the current data can tell the difference among these three different scenarios. In Fig. 6.13, we show the photon-triggered fragmentation function $D_{AA}(z_T)$ for these three different scenarios, compared to the experimental measurements [188] for Au+Au collisions at RHIC. From the figure, we see sizable difference when we include fragmentation photons and jet-plasma photons. But it should be mentioned that the direct photons production is obtained from leading-order pQCD calculation with a p_T-dependent K factor. If a full next-to-leading order (NLO) calculation is employed for two-particle spectrum, there will be additional contribution to the photon-hadron correlations due to the $2 \rightarrow 3$ collisions. The incorporation of a full NLO treatment will be our next step. At this point, the

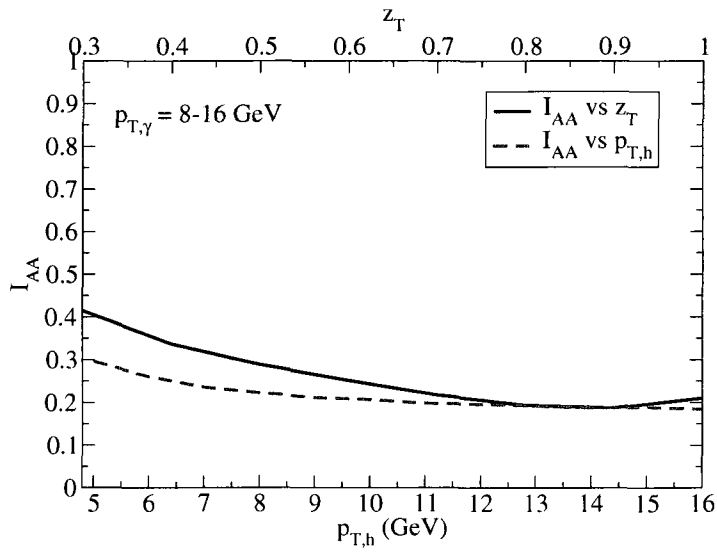

Figure 6.14: Photon-triggered I_{AA} for hadrons as a function of hadron momentum p_T or momentum fraction z_T in central Au+Au collisions (b = 2.4 fm) at RHIC.

current comparison between experimental data and our calculations seems not be able to distinguish between different scenarios. However, it should be pointed out that larger differences might be observed if we are able to measure the away-side hadrons with high z_T (and also high enough p_T for fragmentation to be dominant), where jet-plasma interaction and fragmentation assume more significance to photon-hadron correlations (see Fig. 6.11). Finally, in Fig. 6.14, we show the photon-triggered I_{AA} for hadrons as a function of hadron momentum p_T^h and momentum fraction z_T.

6.5 Conclusions

In this chapter, we have studied the nuclear suppression of high p_T photon-tagged jets in the quark-gluon plasma at RHIC. The energy loss experienced by hard jets is evaluated by consistently incorporating both collisional and radiative energy loss, combined with a fully (3+1)-dimensional hydrodynamical evolution model for the description of the thermalized medium created at RHIC. The production of hard photons in Au+Au collisions at RHIC is calculated by incorporating all the possible sources, including direct photons, fragmentation photons and jet-plasma photons.

Numerical results have been shown for the suppression of away-side hadrons tagged by hard photons in Au+Au collisions relative to p+p collisions. Our calculations of yield per trigger of photon-tagged hadron in both p+p and Au+Au collisions are consistent with the experimental measurements by both PHENIX and STAR collaborations. Our results illustrate that all sources of hard photons are important to a full understanding of the correlations between back-to-back photons and hadrons. At relatively lower z_T regime for the associated hadrons, photon-hadron correlations are found to be dominated by direct photons. At high z_T regime, jet-plasma photons and fragmentation photons become of increasing significance.

In conclusion, our study of photon-hadron correlations will allow together with earlier studies in Chapter 4 and Chapter 5 to experimentally test our understanding of the interaction between the jets and the surrounding plasma created at RHIC.

7

Summary

In Chapter 1, we briefly review the basic phenomenology in relativistic heavy ion collisions, which have been designed to create and study the strongly nuclear matter at extreme temperatures and densities by colliding two heavy nuclei at relativistic energies. According to quantum chromodynamics (QCD), a new phase of matter called quark-gluon plasma (QGP) is expected to exist at such extreme conditions. It is the hope of heavy ion collisions to create such a new phase of matter and study the critical phenomena related to the phase transition to the hadronic matter. The study of QGP is important not only for the understanding of the physics of strongly interacting QCD matter, but have an important impact on cosmology and astrophysics. However, the deconfined degrees of freedom – quarks and gluons, are not directly observable. It is one of most important tasks for physicists to find clear and unambiguous signatures for observing the formation of quark-gluon plasma and studying its properties. This thesis constitutes one of those ongoing efforts by presenting our original research work on two promising signatures in relativistic heavy ion collisions: electromagnetic radiation and high transverse momentum jets.

In Chapter 2, we present a new channel of the direct photon production from a quark-gluon plasma. This new mechanism vanishes in the vacuum and arises solely when the charge conjugation invariance is explicitly broken for the medium. Effectively, it may be described as the bremsstrahlung of a real photon from a thermal gluon in the excited QCD matter. As photon production from such channels is dependent on the gluon density of the medium, it offers a new window to probe the gluon sector of the highly excited strongly interacting matter. It is found that the photon

production rate from this process is suppressed compared to the QCD annihilation and Compton scattering for realistic temperatures and chemical potentials, but could become important in baryon-rich matter.

In Chapter 3, the photon and gluon emission from the quark-gluon plasma is presented in the Arnold-Moore-Yaffe (AMY) formalism. Although this chapter does not constitute my own work, it is important for the work in the following parts of this thesis. The induced gluon emission by jets during their propagating through the plasma is the backbones of the calculation of radiative part of jet energy loss in relativistic heavy ion collisions. The induced photon emission constitutes one of the important sources of hard photon production in QGP and play an important role in the study of photon-hadron correlations at RHIC.

In Chapter 4, we study radiative jet energy loss at high transverse momenta transverse momentum (p_T). The relativistic ideal three-dimensional hydrodynamical model is employed to describe the produced thermalized medium for the calculation of the neutral pion nuclear modification factor R_{AA} in Au+Au collisions at RHIC. We have provided a systematic analysis of R_{AA} as a function of p_T and azimuth ϕ in central and non-central collisions, at mid and forward rapidity. Our study will not only be able to reveal more information about nuclear medium, but also make for a stringent test of theoretical understanding of jet energy loss over a variety of in-medium path lengths, temperatures and initial partonic jet energies once further data become available. We also present our prediction of the nuclear modification factor R_{AA} for charged hadron production at the LHC by employing the two-dimensional ideal hydrodynamical model.

In Chapter 5, we calculate and compared the collisional and radiative energy loss of hard jets in the hot and dense medium created at RHIC. We include radiative energy loss and the additional energy loss by elastic collisions. Our treatment of both processes is complete at leading order in the coupling and accounts for the probabilistic nature of the jet energy loss. While the average energy loss due to elastic collisions is small compared to the radiative one, the time evolution of the

parton momentum distributions are significantly different. We find that the solution of the Fokker-Planck equations of the probability density distributions of partons until fragmentation is decisive for a correct calculation of the nuclear modification factor R_{AA} for pion production in heavy ion collisions. Especially, the magnitude of R_{AA} is sensitive to the inclusion of collisional and radiative energy loss while the shape as a function of p_T does not show strong sensitivity. Possible implications of the collisional energy loss on jet quenching at the LHC have also been presented.

In Chapter 6, we investigate the correlations between the back-to-back triggered photons and associated hadrons in Au+Au collisions. The energy loss of hard jets is evaluated by taking into account both radiative and collisional energy loss. The production of triggered photons is obtained by incorporating all possible sources of photons, and the production of associated hadrons is calculated from the fragmentation of jets after their passing through the hot and dense plasma. The bulk properties of the medium created in Au+Au collision at RHIC is described by (3+1)-dimensional relativistic ideal hydrodynamics. Our results for hadron yield per trigger photon in both p+p and Au+Au collisions are consistent with the experimental measurements. It is found that all photon sources are important for the understanding of high energy photon-hadron correlations.

In conclusion, this thesis constitutes a contribution to our theoretical understanding of the properties of the strongly interacting matter created in relativistic heavy ion collisions. Especially, our study of hard photon production and high momentum hadron suppression as well as their correlations will allow us to experimentally test our understanding of the interaction between the travelling jets and the surrounding plasma. A natural extension of this work will be to study the energy and system size dependence of hard photon and hadron production and their correlations, such as Au+Au collisions at lower energies, Cu+Cu collisions and especially Pb+Pb collisions at the LHC. Lepton pair production and hadron-hadron correlations would be another set of interesting topics for future investigation. Also in our present work, we focus on hadrons in high p_T regime, where fragmentation is expected to be the

dominant mechanism for hadron production. It would be nice if we could have a unified hadronization scheme which combines fragmentation and recombination naturally and describes the experimental data from lower p_T to high p_T regime consistently. Such an approach, however, does not yet exist.

A

Path integral representation of partition function

In quantum statistical mechanics, the fundamental quantity is the probability density operator ρ, from which all the macroscopic quantities of the system can be computed. For example, let A be an observable of the system, then the expectation value of the measurement (ensemble average) of this observable can be calculated from the following equation,

$$\langle A \rangle = \mathrm{Tr}[\rho A]. \tag{A.1}$$

For the canonical ensemble, the density operator $\rho(\beta)$ is give by

$$\rho(\beta) = \frac{1}{Z(\beta)} \exp(-\beta H) = \frac{e^{-\beta H}}{\mathrm{Tr} e^{-\beta H}}, \tag{A.2}$$

where H is the Hamiltonian of the system, $Z(\beta) = \mathrm{Tr} e^{-\beta H}$ is the partition function, and β is the inverse of the temperature, $\beta = 1/T$. In the above equation, we have set the Boltzmann constant to be a natural unit, $k_B = 1$. It can be easily seen that the trace of the density operator is unity, $\mathrm{Tr}\rho(\beta) = 1$. For a thermal equilibrium system of bosons, the partition function reads,

$$Z(\beta) = \sum_a \int d\phi_a \langle \phi_a | e^{-\beta H} | \phi_a \rangle, \tag{A.3}$$

where the sum runs over all states. The partition function may be rewritten as

$$Z(\beta) = \sum_a \int d\phi_a \langle \phi_a | e^{-iH(t_f - t_i)} | \phi_a \rangle = \sum_a \int d\phi_a \langle \phi_a, t_f | \phi_a, t_i \rangle, \tag{A.4}$$

with $t_i = 0$ and $t_f = -i\beta$. We are now in the position to evaluate the general transition amplitude in the quantum field theory,

$$\langle \phi_f, t_f | \phi_i, t_i \rangle = \langle \phi_f, t = 0 | e^{-iH(t_f - t_i)} | \phi_i, t = 0 \rangle = \langle \phi_f | e^{-iH(t_f - t_i)} | \phi_i \rangle, \tag{A.5}$$

where the Hamiltonian is a functional of the field operator and its conjugate momentum,

$$H = \int d^3x \mathcal{H}(\pi, \phi). \tag{A.6}$$

The path integral of this transition amplitude is obtained by discretizing the time interval $t_i < t < t_f$, into N equal small pieces $\Delta t = (t_f - t_i)/N$. At each time interval, we may insert a complete sets of states,

$$\begin{aligned}\langle \phi_f | e^{-iH(t_f - t_i)} | \phi_i \rangle = \lim_{N\to\infty} \int \left(\prod_{k=1}^{N} \frac{d\phi_k d\pi_k}{2\pi} \right) \langle \phi_f | \phi_N \rangle \langle \phi_N | e^{-iH\Delta t} | \phi_N \rangle \langle \phi_N | \pi_{N-1} \rangle \\ \cdots \langle \phi_2 | \pi_1 \rangle \langle \pi_1 | e^{-iH\Delta t} | \phi_1 \rangle \langle \phi_1 | \phi_i \rangle.\end{aligned} \tag{A.7}$$

As we know, $\langle \phi_1 | \phi_i \rangle = \delta(\phi_1 - \phi_i)$, and

$$\langle \phi_{k+1} | \pi_k \rangle = \exp\left(i \int d^3x \pi_k \phi_{k+1} \right). \tag{A.8}$$

As $\Delta t \to 0$ or $N \to \infty$, we can expand the transition amplitude as follows. Keeping terms up to the first order, we obtain

$$\langle \pi_k | e^{-iH\Delta t} | \phi_k \rangle \approx (1 - iH_k \Delta t) \langle \pi_k | \phi_k \rangle = (1 - iH_k \Delta t) \exp\left(-i \int d^3x \pi_k \phi_k \right). \tag{A.9}$$

By putting all ingredients together, the transition amplitude now reads,

$$\begin{aligned}\langle \phi_f | e^{-iH(t_f - t_i)} | \phi_i \rangle = \lim_{N\to\infty} \int \left(\prod_{k=1}^{N} \frac{d\phi_k d\pi_k}{2\pi} \right) \delta(\phi_1 - \phi_i) \\ \times \exp\left\{ i\Delta t \sum_{k=1}^{N} \int d^3x \left[\frac{\pi_k(\phi_{k+1} - \phi_k)}{\Delta t} - \mathcal{H}(\pi_k, \phi_k) \right] \right\},\end{aligned} \tag{A.10}$$

where $\phi_1 = \phi_i$ and $\phi_{N+1} = \phi_f$. Taking the continuum limit, we obtain the formal expression for the transition amplitude,

$$\begin{aligned}\langle \phi_f | e^{-iH(t_f - t_i)} | \phi_i \rangle = \int [d\pi] \int_{\phi(t_i, \vec{x}) = \phi_i}^{\phi(t_f, \vec{x}) = \phi_f} [d\phi] \\ \times \exp\left[i \int_{t_i}^{t_f} dt \int d^3x \left(\pi \frac{\partial \phi}{\partial t} - \mathcal{H}(\pi, \phi) \right) \right].\end{aligned} \tag{A.11}$$

In the above equation, the symbols $[d\pi]$ and $[d\phi]$ denote functional integration. By switching the real time variable t to the imaginary time variable τ, where $t = -i\tau$ with τ real, we obtain the final expression for the partition function [129],

$$Z(\beta) = \int [d\pi] \int [d\phi] \exp\left[\int_0^\beta d\tau \int d^3x \left(i\pi \frac{\partial \phi}{\partial t} - \mathcal{H}(\pi, \phi) \right) \right], \tag{A.12}$$

where the integration over the field ϕ is constrained by a periodic boundary condition $\phi(\beta, \vec{x}) = \phi(0, \vec{x})$.

If the system has a conserved charge, it is straightforward to generalize the result by performing the following replacement,

$$\mathcal{H} \rightarrow \mathcal{H} - \mu\mathcal{N}, \tag{A.13}$$

where $\mathcal{N}$ is the density operator of the conserved charge. The result may also readily be generalized to an arbitrary number of fields and conserved charges.

For a neutral scalar field, the general renormalizable Lagrangian is

$$\mathcal{L} = \frac{1}{2}\partial_\mu\phi\partial_\mu\phi - \frac{1}{2}m^2\phi^2 - V(\phi), \tag{A.14}$$

where $\phi(x)$ is a real field, m is the mass of scalar particles and the interaction is contained in the potential $V(\phi)$,

$$V(\phi) = g\phi^3 + \lambda\phi^4, \tag{A.15}$$

with $\lambda > 0$ for the stability of the vacuum. The momentum conjugate to this field is

$$\pi = \frac{\partial\mathcal{L}}{\partial(\partial_t\phi)} = \frac{\partial\phi}{\partial t}, \tag{A.16}$$

and the Hamiltonian is obtained through the usual Legendre transformation

$$\mathcal{H} = \pi\frac{\partial\phi}{\partial t} - \mathcal{L} = \frac{1}{2}\pi^2 + \frac{1}{2}(\nabla\phi)^2 + \frac{1}{2}m^2\phi^2 + V(\phi). \tag{A.17}$$

By performing the similar procedure as described above, we are able to obtain the partition function

$$Z = \int [d\phi] e^{S[\phi]} = \int [d\phi] \exp\left(\int_0^\beta d\tau \int d^3x\mathcal{L}\right), \tag{A.18}$$

where the functional integration of ϕ is constrained by a periodic boundary condition $\phi(\beta, \vec{x}) = \phi(0, \vec{x})$. For the case of free field, $V(\phi) = 0$, we may perform the integration by parts [129],

$$Z = \int [d\phi] \exp\left[-\frac{1}{2}\int_0^\beta d\tau \int d^3x\phi\left(-\frac{\partial^2}{\partial\tau^2} - \nabla^2 + m^2\right)\phi\right]. \tag{A.19}$$

It is similar to generalize the above result for fermions, which are described by a four-component Dirac spinor ψ. For example, the Lagrangian for the free Dirac field reads,

$$\mathcal{L} = \bar{\psi}(i\gamma^\mu \partial_\mu - m)\psi. \tag{A.20}$$

The Dirac matrices γ^μ are defined by the anticommutators $\{\gamma^\mu, \gamma^\nu\} = 2g^{\mu\nu}$. In the standard convention, they are given by

$$\gamma^0 = \begin{pmatrix} 0 & 1 \\ 1 & 0 \end{pmatrix}, \quad \vec{\gamma} = \begin{pmatrix} 0 & \vec{\sigma} \\ -\vec{\sigma} & 0 \end{pmatrix}. \tag{A.21}$$

We may write the Lagrangian out explicitly using the identity $\bar{\psi} = \psi^\dagger \gamma^0$,

$$\mathcal{L} = \psi^\dagger \gamma^0 \left(i\gamma^0 \frac{\partial}{\partial t} + i\vec{\gamma} \cdot \nabla - m \right) \psi. \tag{A.22}$$

The momentum conjugate to the field ψ is

$$\Pi = \frac{\partial \mathcal{L}}{\partial(\partial\psi/\partial t)} = i\psi^\dagger. \tag{A.23}$$

The Hamiltonian is found using the Legendre transformation

$$\mathcal{H} = \Pi \frac{\partial \psi}{\partial t} - \mathcal{L} = \bar{\psi}(-i\vec{\gamma} \cdot \nabla + m)\psi. \tag{A.24}$$

The final expression for partition function is found to be [129]

$$Z = \int [id\psi^\dagger][d\psi] \exp\left[\int_0^\beta d\tau \int d^3x \bar{\psi} \left(-\gamma^0 \frac{\partial}{\partial \tau} + i\vec{\gamma} \cdot \nabla - m \right) \psi \right], \tag{A.25}$$

where the functional integration of ψ is constrained by a periodic boundary condition $\psi(\beta, \vec{x}) = -\psi(0, \vec{x})$.

B

Thermal Green's function – Imaginary-time propagator

The thermal average of time-ordered two-point function is given by

$$\Delta(\tau_1, \vec{x}_1; \tau_2, \vec{x}_2) = \langle T(\phi(\tau_1, \vec{x}_1)\phi(\tau_2, \vec{x}_2)) \rangle. \tag{B.1}$$

The T-product in imaginary time τ operates as follows,

$$T(\phi(\tau_1, \vec{x}_1)\phi(\tau_1, \vec{x}_2) = \phi(\tau_1, \vec{x}_1)\phi(\tau_2, \vec{x}_2)\theta(\tau_1 - \tau_2) \pm \phi(\tau_2, \vec{x}_2)\phi(\tau_1, \vec{x}_1)\theta(\tau_2 - \tau_1) \tag{B.2}$$

where θ is the step-function, and $+$ and $-$ are for bosons and fermions, respectively. Now we define a function $\Delta(\tau, \vec{x})$,

$$\Delta(\tau, \vec{x}) = \Delta(\tau_2 - \tau_1, x_2 - x_1) = \Delta(\tau_1, \vec{x}_1; \tau_2, \vec{x}_2). \tag{B.3}$$

From the periodical property $\phi(\beta, \vec{x}) = \pm\phi(0, \vec{x})$, we know $\Delta(\tau, \vec{x})$ is a periodic (anti-periodic) function of imaginary time τ,

$$\Delta(\tau, \vec{x}) = \pm\Delta(\tau - \beta, \vec{x}), \tag{B.4}$$

for any vale of τ in the interval $[0, \beta]$. The Fourier transform of the imaginary-time propagator is defined as

$$\Delta(\omega_n, \vec{p}) = \int_0^\beta d\tau \int d^3x e^{i(\omega_n\tau + \vec{p}\cdot\vec{x})}\Delta(\tau, \vec{x}), \tag{B.5}$$

with the inverse formula being

$$\Delta(\tau, \vec{x}) = T\sum_n \int \frac{d^3p}{(2\pi)^3} e^{-i(\omega_n\tau + \vec{p}\cdot\vec{x})}\Delta(\omega_n, \vec{p}), \tag{B.6}$$

where n is an integer and ω_n are discrete Matsubara frequencies. Since $\tau, \Delta(\vec{x})$ is periodic (anti-periodic) in the interval $[0, \beta]$, the frequencies take discrete values

$$\omega_n = 2\pi nT, \quad \omega_n = 2\pi(n + \frac{1}{2})T, \tag{B.7}$$

for bosons and fermions, respectively. Therefore, in the imaginary time formalism, the energy variable p_0 is switched to the Matsubara frequencies ω_n, where $p_0 = i\omega_n$, with ω_n real.

For a neutral scalar field, the Lagrangian density in Minkowski space reads

$$\mathcal{L} = \frac{1}{2}\partial_\mu\phi\partial_\mu\phi - \frac{1}{2}m^2\phi^2 - V(\phi), \tag{B.8}$$

As usual in quantum field theory, we define a generating functional $Z[\beta, J]$, with $Z[\beta] = Z[\beta, J = 0]$,

$$Z[\beta, J] = \int [d\phi] \exp\left(S[\phi] + \int_0^\beta d\tau \int d^3x J\phi\right). \tag{B.9}$$

The propagator in the imaginary time formalism is obtained by functional differentiation

$$\Delta(\tau_1, \vec{x}_1; \tau_2, \vec{x}_2) = \frac{1}{Z[\beta]} \frac{\delta^2 Z[\beta, J]}{\delta J(\tau_1, x_1)\delta J(\tau_2, x_2)}\bigg|_{J=0} = \frac{1}{Z[\beta]}\int [d\phi]\phi(\tau_1, \vec{x}_1)\phi(\tau_2, \vec{x}_2)e^{S[\phi]}. \tag{B.10}$$

For the case of free field, $V(\phi) = 0$, we may perform the integration by parts. The generating function reads,

$$Z_F[\beta, J] = \int [d\phi] \exp\left[-\frac{1}{2}\int_0^\beta d\tau \int d^3x\phi\left(-\frac{\partial^2}{\partial\tau^2} - \nabla^2 + m^2\right)\phi + J\phi\right]. \tag{B.11}$$

After performing the integration over the field $\phi(x)$, we obtain

$$Z_F[\beta, J] = Z_F[\beta] \exp\left(\frac{1}{2}\int_0^\beta d\tau_1 d\tau_2 \int d^3x_1 d^3x_2 J(\tau_1, \vec{x}_1)\Delta_F(\tau_1, \vec{x}_1; \tau_2, \vec{x}_2)J(\tau_2, \vec{x}_2)\right), \tag{B.12}$$

where the two-point Green function $\Delta_F(\tau, \vec{x}) = \Delta_F(\tau_2 - \tau_1, \vec{x}_2 - \vec{x}_1) = \Delta_F(\tau_1, \vec{x}_1; \tau_2, \vec{x}_2)$ is the solution of the following partial differential equation

$$\left(-\frac{\partial^2}{\partial\tau^2} - \nabla_x^2 + m^2\right)\Delta_F(\tau, \vec{x}) = \delta(\tau)\delta^3(\vec{x}). \tag{B.13}$$

In the momentum space, the above equation reads,

$$(\omega_n^2 + \vec{p}^2 + m^2)\Delta_F(\omega_n, \vec{p}) = 1, \tag{B.14}$$

where $\omega_n = 2n\pi/\beta$, with n an integer. It is straightforward that the above equation has the following solution,

$$\Delta_F(\omega_n, \vec{p}) = -\frac{1}{(i\omega_n)^2 - (\vec{p}^2 + m^2)} = \sum_{s=\pm 1} \frac{-s}{2E_p} \frac{1}{i\omega_n - sE_p}, \tag{B.15}$$

where $E_p = \sqrt{\vec{p}^2 + m^2}$. It is often useful work in the mixed representation. Then the propagator $\Delta_F(\tau, \vec{p})$ in the mixed representation is defined as

$$\Delta_F(\tau, \vec{p}) = T \sum_n e^{-i\omega_n \tau} \Delta_F(\omega_n, \vec{p}). \tag{B.16}$$

The inverse transformation reads,

$$\Delta_F(\omega_n, \vec{p}) = \int_0^\beta d\tau e^{i\omega_n \tau} \Delta_F(\tau, \vec{p}). \tag{B.17}$$

The propagator in mixed representation may be obtained by converting the frequency sum into the contour integral [129] (see Appendix D),

$$\begin{aligned} \Delta_F(\tau, \vec{p}) &= \frac{1}{2E_p} \left([1 + f(E_p)] e^{-E_p \tau} + f(E_p) e^{E_p \tau} \right) \\ &= \sum_{s=\pm 1} \Delta_F^s(\tau, \vec{p}) = \sum_{s=\pm 1} \frac{s}{2E_p} \left[1 + f(sE_p) \right] e^{-sE_p \tau}, \end{aligned} \tag{B.18}$$

where $f(E_p) = 1/[\exp(\beta E_p) - 1]$ is the Bose-Einstein distribution function. The last step in the above equation is obtained by using the identity, $1 + f(E) + f(-E) = 0$. The propagator in coordinate space $\Delta_F(\tau, \vec{x})$ may be obtained by

$$\Delta_F(\tau, \vec{x}) = T \sum_n \int \frac{d^3p}{(2\pi)^3} e^{-i(\omega_n \tau + \vec{p} \cdot \vec{x})} \Delta_F(\omega_n, \vec{p}) = \int \frac{d^3p}{(2\pi)^3} e^{-i\vec{p} \cdot \vec{x}} \Delta_F(\tau, \vec{p}). \tag{B.19}$$

For a free Dirac field, the general Lagrangian reads,

$$\mathcal{L} = \bar{\psi}(i\gamma^\mu \partial_\mu - m)\psi. \tag{B.20}$$

The free propagator for fermions in the imaginary time can be obtained following the same procedure,

$$S_F(\omega_n, \vec{p}) = -\frac{\gamma_0(i\omega_n) - \vec{\gamma} \cdot \vec{p} + m}{(i\omega_n)^2 - (\vec{p}^2 + m^2)}. \tag{B.21}$$

where $\omega_n = (2n+1)\pi/\beta$, with n an integer. Now we define the quantity $\tilde{\Delta}_F(i\omega_n, E_p)$

$$\tilde{\Delta}_F(i\omega_n, E_p) = -\frac{1}{(i\omega_n)^2 - (\vec{p}^2 + m^2)} = \sum_{s=\pm 1} \frac{-s}{2E_p} \frac{1}{i\omega_n - sE_p}. \tag{B.22}$$

Similarly, its mixed representation $\tilde{\Delta}_F(\tau, \vec{p})$ may also be defined,

$$\tilde{\Delta}_F(\tau, \vec{p}) = T \sum_n e^{-i\omega_n \tau} \tilde{\Delta}_F(\omega_n, \vec{p}). \tag{B.23}$$

The inverse transformation reads,

$$\tilde{\Delta}_F(\omega_n, \vec{p}) = \int_0^\beta d\tau e^{i\omega_n \tau} \tilde{\Delta}_F(\tau, \vec{p}). \tag{B.24}$$

By computing the similar contour integral [129], we obtain the propagator in mixed representation (see Appendix D),

$$\begin{aligned} \tilde{\Delta}_F(\tau, \vec{p}) &= \frac{1}{2E_p} \left([1 - \tilde{f}(E_p)] e^{-E_p \tau} - \tilde{f}(E_p) e^{E_p \tau} \right) \\ &= \sum_{s=\pm 1} \tilde{\Delta}_F^s(\tau, \vec{p}) = \sum_{s=\pm 1} \frac{s}{2E_p} \left[1 - \tilde{f}(sE_p) \right] e^{-sE_p \tau}, \end{aligned} \tag{B.25}$$

where $\tilde{f}(E_p) = 1/[\exp(\beta E_p) + 1]$ is Fermi-Dirac distribution function. Note now $1 - \tilde{f}(E) - \tilde{f}(-E) = 0$. The propagator in coordinate space $\tilde{\Delta}_F(\tau, \vec{x})$ is then obtained by

$$\tilde{\Delta}_F(\tau, \vec{x}) = T \sum_n \int \frac{d^3p}{(2\pi)^3} e^{-i(\omega_n \tau + \vec{p} \cdot \vec{x})} \tilde{\Delta}_F(\omega_n, \vec{p}) = \int \frac{d^3p}{(2\pi)^3} e^{-i\vec{p} \cdot \vec{x}} \tilde{\Delta}_F(\tau, \vec{p}) \tag{B.26}$$

The above result can be generalized to the case of non-zero chemical potential $\mu \neq 0$ by replacing $i\omega_n$ in the the propagator with $i\omega_n + \mu$, and E_p in the thermal distribution function with $E_p - \mu$, respectively.

C

Spectral functions

The two basic two-point correlation functions in the real time are $D^{>}(t,\vec{x})$ and $D^{>}(t,\vec{x})$, defined as,

$$iD^{>}(t,\vec{x}) = \langle\phi(t,\vec{x})\phi(0,\vec{0})\rangle, \quad iD^{<}(t,\vec{x}) = \langle\phi(0,\vec{0})\phi(t,\vec{x})\rangle \tag{C.1}$$

Their Fourier transformations and the inverse transformations read

$$\begin{aligned} D^{>}(p_0,\vec{p}) &= \int d^4x e^{i(p_0t-\vec{p}\cdot\vec{x})}D^{>}(t,\vec{x}), \quad D^{>}(t,\vec{x}) = \int \frac{d^4p}{(2\pi)^4}e^{-i(p_0t-\vec{p}\cdot\vec{x})}D^{>}(p_0,\vec{p}), \\ D^{<}(p_0,\vec{p}) &= \int d^4x e^{i(p_0t-\vec{p}\cdot\vec{x})}D^{<}(t,\vec{x}), \quad D^{<}(t,\vec{x}) = \int \frac{d^4p}{(2\pi)^4}e^{-i(p_0t-\vec{p}\cdot\vec{x})}D^{<}(p_0,\vec{p}). \end{aligned} \tag{C.2}$$

By using the cylindrical properties of the trace, we obtain

$$\begin{aligned} D^{>}(t,\vec{x}) &= \frac{1}{Z[\beta]}\mathrm{Tr}\left[e^{-\beta H}\phi(t,\vec{x})\phi(0,\vec{0})\right] = \frac{1}{Z[\beta]}\mathrm{Tr}\left[\phi(t+i\beta,\vec{x})e^{-\beta H}\phi(0,\vec{0})\right] \\ &= \frac{1}{Z[\beta]}\mathrm{Tr}\left[e^{-\beta H}\phi(0,\vec{0})\phi(t+i\beta,\vec{x})\right] = D^{<}(t+i\beta,\vec{x}). \end{aligned} \tag{C.3}$$

Going to the momentum space, the above relation reads,

$$D^{>}(p_0,\vec{p}) = e^{\beta p_0}D^{<}(p_0,\vec{p}). \tag{C.4}$$

The physical interpretation of this result is related to the microscopic detailed balance. It is often useful to to define the normal correlation function $D^{n}(t,\vec{x})$ in the real time,

$$iD^{n}(t,\vec{x}) = \langle[\phi(t,\vec{x}),\phi(0,\vec{0})]\rangle = iD^{>}(t,\vec{x}) - iD^{<}(t,\vec{x}). \tag{C.5}$$

By doing Fourier transformations, we obtain its expression in momentum space,

$$D^{n}(p_0,\vec{p}) = \int d^4x e^{i(p_0t-\vec{p}\cdot\vec{x})}D^{n}(t,\vec{x}). \tag{C.6}$$

The spectral function is now defined as

$$\rho(p_0,\vec{p}) = iD^n(p_0,\vec{p}) = iD^>(p_0,\vec{p}) - iD^<(p_0,\vec{p}). \tag{C.7}$$

Therefore, we may rewrite the correlation functions $D^>(p_0,\vec{p})$ and $D^<(p_0,\vec{p})$ in terms of the spectral function as follows,

$$iD^>(p_0,\vec{p}) = [1+f(p_0)]\rho(p_0,\vec{p}), \quad iD^<(p_0,\vec{p}) = f(p_0)\rho(p_0,\vec{p}), \tag{C.8}$$

where $f(p_0) = 1/[\exp(\beta p_0) - 1]$ is the Bose-Einstein thermal distribution function.

In linear response theory, the most relevant correlations are the retarded and advanced correlation functions $D^R(t,\vec{x})$ and $D^A(t,\vec{x})$, defined as follows,

$$\begin{aligned} iD^R(t,\vec{x}) &= \langle\theta(t)[\phi(t,\vec{x}),\phi(0,\vec{0})] = \theta(t)iD^n(t,\vec{x})\rangle \\ iD^A(t,\vec{x}) &= -\langle\theta(-t)[\phi(t,\vec{x}),\phi(0,\vec{0})]\rangle = -\theta(-t)iD^n(t,\vec{x}). \end{aligned} \tag{C.9}$$

It is easily to see

$$\left[iD^R(t,\vec{x})\right]^\dagger = -\left[iD^A(t,\vec{x})\right] \Longrightarrow \left[D^R(t,\vec{x})\right]^\dagger = \left[D^A(t,\vec{x})\right]. \tag{C.10}$$

The Fourier transforms in the momentum space read

$$D^R(p_0,\vec{p}) = \int d^4x e^{i(p_0t-\vec{p}\cdot\vec{x})}D^R(t,\vec{x}), \quad D^A(p_0,\vec{p}) = \int d^4x e^{i(p_0t-\vec{p}\cdot\vec{x})}D^R(t,\vec{x}). \tag{C.11}$$

From the definitions of $D^R(t,\vec{x})$ and $D^A(t,\vec{x})$, we obtain

$$iD^R(t,\vec{x}) - iD^A(t,\vec{x}) = iD^n(t,\vec{x}) = iD^>(t,\vec{x}) - iD^<(t,\vec{x}). \tag{C.12}$$

Therefore, we may also write the following expression for the spectral function

$$\rho(p_0,\vec{p}) = iD^R(p_0,\vec{p}) - iD^A(p_0,\vec{p}). \tag{C.13}$$

From the usual representation of the θ-function,

$$\theta(t) = i\int_{-\infty}^{\infty}\frac{d\omega}{2\pi}\frac{e^{-i\omega t}}{\omega+i\epsilon}, \tag{C.14}$$

we find that the retarded and advanced correlation functions may be expressed as the integrals of the spectral function,

$$iD^R(p_0,\vec{p}) = -i\int_{-\infty}^{\infty}\frac{d\omega}{2\pi}\frac{\rho(\omega,\vec{p})}{\omega-p_0-i\epsilon}, \quad iD^A(p_0,\vec{p}) = -i\int_{-\infty}^{\infty}\frac{d\omega}{2\pi}\frac{\rho(\omega,\vec{p})}{\omega-p_0+i\epsilon} \tag{C.15}$$

From the identity

$$\frac{1}{x \pm i\epsilon} = P\left[\frac{1}{x}\right] \mp i\pi\delta(x), \tag{C.16}$$

where P represent the Couchy principle value, the above equations imply that the spectral function is related to the imaginary part of two-point functions,

$$\rho(p_0, \vec{p}) = -2\mathrm{Im}D^R(p_0, \vec{p}), \quad \rho(p_0, \vec{p}) = 2\mathrm{Im}D^A(p_0, \vec{p}). \tag{C.17}$$

The real parts of retarded and advanced correlation functions are equal,

$$\mathrm{Re}D^R(p_0, \vec{p}) = \mathrm{Re}D^A(p_0, \vec{p}). \tag{C.18}$$

The imaginary-time propagator in the finite temperature field theory may also be connected to the spectral function. Performing the Fourier transformation, we obtain

$$\Delta(\omega_n, \vec{p}) = \int_0^\beta d\tau \int d^3x e^{i(\omega_n\tau + \vec{p}\cdot\vec{x})}\Delta(\tau, \vec{x}) = \int_\infty^\infty \frac{d\omega}{2\pi}\frac{\rho(\omega, \vec{p})}{\omega - i\omega_n}. \tag{C.19}$$

This implies that the retarded and advanced propagators may be obtained from the imaginary-time propagator by analytical continuation as follows,

$$D^R(p_0, \vec{p}) = -\Delta(\omega_n, \vec{p})|_{i\omega_n = p_0 + i\epsilon}, \quad D^A(p_0, \vec{p}) = -\Delta(\omega_n, \vec{p})|_{i\omega_n = p_0 - i\epsilon}. \tag{C.20}$$

From the imaginary-time propagator of a free field for bosons,

$$\Delta_F(\omega_n, \vec{p}) = -\frac{1}{(i\omega_n)^2 - (\vec{p}^2 + m^2)}, \tag{C.21}$$

we obtain

$$\rho(p_0, \vec{p}) = 2\pi\mathrm{sign}(p_0)\delta(p_0^2 - \vec{p}^2 - m^2). \tag{C.22}$$

Thus the spectral function has the weight concentrated on the mass shell of the particle. Generally, for interacting particle in the medium, this weight will get spread out over a range of energies.

It is also of great interest to take a look at the real-time propagator $D(t, \vec{x})$ in the finite temperature, defined as

$$iD(t, \vec{x}) = \langle T\phi(t, \vec{x})\phi(0, \vec{0})\rangle = \theta(t)iD^>(t, \vec{x}) + \theta(-t)iD^<(t, \vec{x}). \tag{C.23}$$

In terms of spectral function, it reads [126],

$$iD(p_0,\vec{p}) = -i\int_{\infty}^{\infty}\frac{d\omega}{2\pi}\frac{\rho(\omega,\vec{p})}{\omega - p_0 - i\epsilon} + f(p_0)\rho(p_0,\vec{p}). \tag{C.24}$$

It is easy to find the free propagator in the real time by substituting the free spectral function [126],

$$iD_F(p_0,\vec{p}) = \frac{i}{p_0^2 - \vec{p}^2 - m^2 + i\epsilon} + 2\pi n(p_0)\delta(p_0^2 - \vec{p}^2 - m^2), \tag{C.25}$$

where $n(p_0) = 1/[\exp(\beta|p_0|) - 1]$. The first term is the zero temperature part, and the second term is the thermal part which vanishes in the zero temperature.

D

Matsubara frequency sum

In the imaginary-time formalism, the zeroth components of four momenta are discrete Matsubara frequencies. In this appendix, we will present some techniques to perform the sum of Matsubara frequencies encountered in the computation of Feynman diagrams.

The first frequency sum we are going to compute is the mixed representation of free propagators of fermions with zero chemical potential (the generalization to Eq. (2.13) with $\mu \neq 0$ is straightforward),

$$\tilde{\Delta}_F(\tau, \vec{p}) = T \sum_n e^{-i\omega_n \tau} \tilde{\Delta}_F(i\omega_n, \vec{p}), \tag{D.1}$$

where the propagator in the momentum space is given by

$$\tilde{\Delta}_F(i\omega_n, \vec{p}) = -\frac{1}{(i\omega_n)^2 - E_p^2}, \tag{D.2}$$

with $E_p = \sqrt{\vec{p}^2 + m^2}$, and $p^0 = i\omega_n = i(2n+1)\pi T$. As has been stated in [129], the sum over the Matsubara frequencies can be converted into contour integrals in the complex plane. Here for $p^0 = i\omega_n = i(2n+1)\pi T$, we have

$$T \sum_{p^0} f(p^0) = \frac{1}{2\pi i} \int_C dp^0 f(p^0) \left[\frac{1}{2} - \frac{1}{e^{\beta p^0} + 1} \right]. \tag{D.3}$$

where the contour C is shown as in the left figure, which is equivalent to $C_1 + C_2$ in the middle figure.

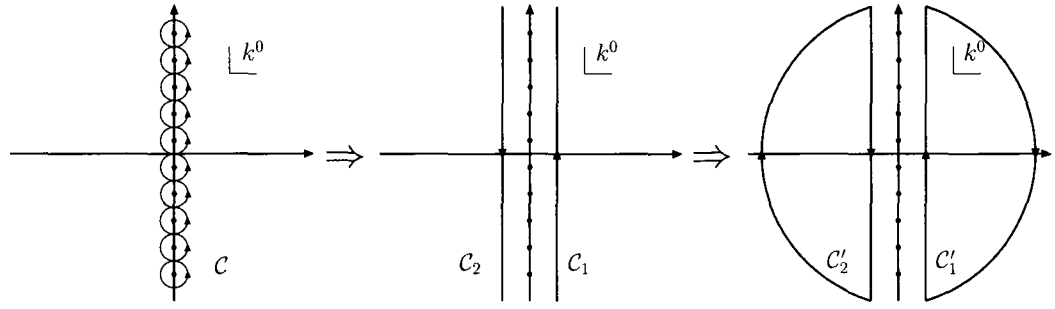

Therefore, we obtain

$$\tilde{\Delta}_F(\tau,\vec{p}) = -\frac{1}{2\pi i}\int_{C_1+C_2} dp^0 e^{-p^0\tau}\frac{1}{(p^0)^2-E_p^2}\left[\frac{1}{2}-\frac{1}{e^{\beta p^0}+1}\right]. \tag{D.4}$$

Note that $1/(e^{-\beta p^0}+1) = 1 - 1/(e^{\beta p^0}+1)$, we have

$$\begin{aligned}\tilde{\Delta}_F(\tau,\vec{p}) = &-\frac{1}{2\pi i}\int_{C_1} dp^0 e^{-p^0\tau}\frac{1}{(p^0)^2-E_p^2}\left[\frac{1}{2}-\frac{1}{e^{\beta p^0}+1}\right]\\ &-\frac{1}{2\pi i}\int_{C_2} dp^0 e^{-p^0\tau}\frac{1}{(p^0)^2-E_p^2}\left[-\frac{1}{2}+\frac{1}{e^{-\beta p^0}+1}\right].\end{aligned} \tag{D.5}$$

To further evaluate the contour integral, we need to close the integral contour, $C_1 \to C_1'$ and $C_2 \to C_2'$.

$$\begin{aligned}\tilde{\Delta}_F(\tau,\vec{p}) = &-\frac{1}{2\pi i}\int_{C_1\to C_1'} dp^0 e^{-p^0\tau}\frac{1}{(p^0)^2-E_p^2}\left[1-\frac{1}{e^{\beta k^0}+1}\right]\\ &-\frac{1}{2\pi i}\int_{C_2\to C_2'} dp^0 e^{-p^0\tau}\frac{1}{(p^0)^2-E_p^2}\frac{1}{e^{-\beta p^0}+1}.\end{aligned} \tag{D.6}$$

Note that we have put the constant $-1/2$ in the second term to the first term in order to make the integral in the second term zero as $p^0 \to -\infty$. Evaluating the residues at $p^0 = E_p$ in contour C_1' and $p^0 = -E_p$ in contour C_2', we obtain the final result for the mixed representation of Fermion propagator,

$$\tilde{\Delta}_F(\tau,\vec{p}) = \frac{1}{2E_p}\left([1-\tilde{n}(E_p)]e^{-E_p\tau} - \tilde{n}(E_p)e^{E_p\tau}\right). \tag{D.7}$$

Second, we compute the following product of two imaginary-time fermion propagators (corresponding to setting $\mu = 0$ in Eq. (2.18), and the generalization to non-zero chemical potential is straightforward),

$$S(i\omega_n) = T\sum_n \tilde{\Delta}_{s_2}(i\omega_n, E_2)\tilde{\Delta}_{s_1}(i\omega_n + i\omega_k, E_1), \tag{D.8}$$

where $\omega_n = (2n+1)\pi T$, $\omega_k = 2n_k\pi T$, and

$$\tilde{\Delta}_s(i\omega_n, E) = \frac{s}{2E} e^{-sE\tau} \left(1 - \tilde{f}(sE)\right). \tag{D.9}$$

From the Fourier transformation of mixed propagator, we obtain

$$S(i\omega_n) = T\sum_n \int_0^\beta d\tau_2 \int_0^\beta d\tau_1 e^{i\omega_n\tau_2} e^{(i\omega_n + i\omega_k)\tau_1} \tilde{\Delta}_{s_2}(\tau_2, E_2)\tilde{\Delta}_{s_1}(\tau_1, E_1). \tag{D.10}$$

As $\tau_1, \tau_2 \in (0, \beta)$, we have the identity

$$T\sum_n e^{i\omega_n(\tau_1+\tau_2)} = \delta(\tau_1 + \tau_2 - \beta). \tag{D.11}$$

Substituting the above identity and the following equation,

$$\tilde{\Delta}_s(\tau, E) = \frac{s}{2E}\left[1 - \tilde{f}(sE)\right] e^{-sE\tau}, \tag{D.12}$$

we obtain

$$S(i\omega_n) = \int_0^\beta d\tau_1 e^{(i\omega_k - s_1E_1 + s_2E_2)\tau_1} \frac{s_1s_2}{4E_1E_2}\left[1 - \tilde{f}(s_2E_2)\right] e^{-s_2E_2\beta}\left[1 - \tilde{f}(s_1E_1)\right]. \tag{D.13}$$

Performing the integral over τ_1 gives us,

$$S(i\omega_n) = \frac{s_1s_2}{4E_1E_2}\frac{e^{-s_1E_1\beta} - e^{-s_2E_2\beta}}{i\omega_k - s_1E_1 + s_2E_2}\left[1 - \tilde{f}(s_2E_2)\right]\left[1 - \tilde{f}(s_1E_1)\right]. \tag{D.14}$$

From the identity

$$e^{-\beta sE} = \frac{\tilde{f}(sE)}{1 - \tilde{f}(sE)}, \tag{D.15}$$

we obtain the final result for the product of two imaginary-time propagator,

$$S(i\omega_n) = \frac{s_1s_2}{4E_1E_2}\frac{\tilde{f}(s_1E_1) - \tilde{f}(s_2E_2)}{i\omega_k - s_1E_1 + s_2E_2}. \tag{D.16}$$

Finally, we compute the following expression, which appears in Chapter 2 when we evaluate the photon production rate by cutting self-energy diagrams (see Eq. (2.39)),

$$\mathrm{Disc}T\sum_{k^0} f(k^0)g(p^0 - k^0), \tag{D.17}$$

In the above equation, p^0 and k^0 are imaginary discrete Matsubara frequencies, $p^0 = n_p i2\pi T$, $k^0 = n_k i2\pi T$, with integers n_p, n_k ranging from $-\infty$ to ∞. The discontinuity

of a complex function $f(z)$ across real axis is defined as $\mathrm{Disc}f(z) = f(z+i\epsilon)-f(z-i\epsilon)$, where $\epsilon = 0^+$ is any tiny number. In order to evaluate the above expression, we first recall the Cauchy theorem for the contour integral,

$$f(a) = \frac{1}{2\pi i}\int_C \frac{f(z)}{z-a}dz, \tag{D.18}$$

where the contour C is taken counter-clockwise. We may take the integral contour C across the real axis, such that

$$f(a) = \frac{1}{2\pi i}\left[\int_{-\infty-i\epsilon}^{\infty-i\epsilon} + \int_{\infty+i\epsilon}^{-\infty+i\epsilon}\right]\frac{f(z)}{z-a}dz = -\frac{1}{2\pi i}\int_{-\infty}^{\infty}\frac{f(z+i\epsilon)-f(z-i\epsilon)}{z-a}dz. \tag{D.19}$$

Therefore,

$$f(a) = -\frac{1}{2\pi i}\int_{-\infty}^{\infty}\frac{\mathrm{Disc}f(z)}{z-a}dz = -\int_{-\infty}^{\infty}\frac{\rho(z)}{z-a}dz, \tag{D.20}$$

where we the spectral function $\rho(z)$ of $f(z)$ has been defined as $\rho(z) = \mathrm{Disc}f(z)/(2\pi i)$. Now we may also rewrite Eq. (D.17) in terms of the spectral functions of $f(k^0)$ and $g(p^0-k^0)$ as follows,

$$\mathrm{Disc}T\sum_{k^0} f(k^0)g(p^0-k^0) = \mathrm{Disc}T\sum_{k^0}\int_{-\infty}^{\infty}d\omega\frac{\rho_1(\omega)}{\omega-k^0}\int_{-\infty}^{\infty}d\omega'\frac{\rho_2(\omega')}{\omega'-p^0+k^0}. \tag{D.21}$$

Now our task becomes to evaluate the following expression,

$$\mathrm{Disc}T\sum_{k^0}\frac{1}{\omega-k^0}\frac{1}{\omega'-p^0+k^0}. \tag{D.22}$$

As has been stated in [129], the sum over the Matsubara frequencies can be converted into contour integrals over a complex k^0, i.e., for any function $f(k^0)$,

$$T\sum_{k^0} f(k^0) = \frac{1}{2\pi i}\int_C dk^0 f(k^0)\left[\frac{1}{2}+\frac{1}{e^{\beta k^0}-1}\right], \tag{D.23}$$

where the contour C is shown as the left figure, which is equivalent to C_1+C_2 in the middle figure. C_1+C_2.

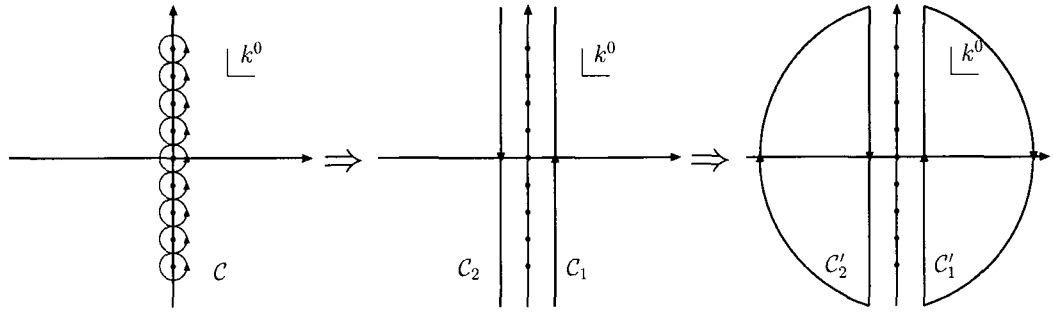

Therefore, we obtain

$$T\sum_{k_0}\frac{1}{\omega-k^0}\frac{1}{\omega'-p^0+k^0}=\frac{1}{2\pi i}\int_{C_1+C_2}dk^0\frac{1}{\omega-k^0}\frac{1}{\omega'-p^0+k^0}\left[\frac{1}{2}+\frac{1}{e^{\beta k^0}-1}\right]. \quad \text{(D.24)}$$

To further evaluate the contour integral, we need to close the integral contour, $C_1 \to C_1'$ and $C_2 \to C_2'$. Taking the residues of the function inside the integral at $k^0=\omega$ and $k^0=p^0-\omega'$,

$$T\sum_{k_0}\frac{1}{\omega-k^0}\frac{1}{\omega'-p^0+k^0}=\frac{1}{\omega'-p^0+\omega}\left(\frac{1}{2}+\frac{1}{e^{\beta\omega}-1}\right) -\frac{1}{\omega-p^0+\omega'}\left(\frac{1}{2}+\frac{1}{e^{-\beta\omega'}-1}\right), \quad \text{(D.25)}$$

where the identity $\exp(\beta p^0)=1$ has been implicitly employed. The above expression may be simplified to be,

$$T\sum_{k_0}\frac{1}{\omega-k^0}\frac{1}{\omega'-p^0+k^0}=\frac{1}{\omega'+\omega-p^0}\left[1+f(\omega)+f(\omega')\right], \quad \text{(D.26)}$$

by using the fact that $1+f(\omega)+f(-\omega)=0$, where $f(\omega)=1/(e^{\omega/T}-1)$. Now taking the discontinuity across the real axis,

$$\mathrm{Disc}T\sum_{k^0}\frac{1}{\omega-k^0}\frac{1}{\omega'-p^0+k^0}=\mathrm{Disc}\left[\frac{1}{\omega'+\omega-p^0}\right]\left[1+f(\omega)+f(\omega')\right]. \quad \text{(D.27)}$$

It is straightforward to show that when $p^0 \to E \pm i\epsilon$,

$$\mathrm{Disc}\left[\frac{1}{\omega'+\omega-p^0}\right]=2\pi i\delta(\omega+\omega'-E). \quad \text{(D.28)}$$

Putting all together, we obtain the desired formula,

$$\mathrm{Disc}T\sum_{k^0}f(k^0)g(p^0-k^0)=2\pi i\int d\omega\int d\omega'\rho_1(\omega)\rho_1(\omega') \times\delta(\omega+\omega'-E)(1+f(\omega)+f(\omega')). \quad \text{(D.29)}$$

By employing the following identity,

$$1+f(\omega)+f(\omega')=[e^{(\omega+\omega')/T}-1]f(\omega)f(\omega'), \quad \text{(D.30)}$$

we obtain

$$\mathrm{Disc}T\sum_{k^0}f(k^0)g(p^0-k^0)=2\pi i(e^{E/T}-1)\int d\omega\int d\omega'\rho_1(\omega)\rho_1(\omega') \times\delta(\omega+\omega'-E)f(\omega)f(\omega'). \quad \text{(D.31)}$$

BIBLIOGRAPHY

[1] PHENIX, K. Adcox *et al.*, Nucl. Phys. **A757**, 184 (2005), [nucl-ex/0410003].

[2] BRAHMS, I. Arsene *et al.*, Nucl. Phys. **A757**, 1 (2005), [nucl-ex/0410020].

[3] B. B. Back *et al.*, Nucl. Phys. **A757**, 28 (2005), [nucl-ex/0410022].

[4] STAR, J. Adams *et al.*, Nucl. Phys. **A757**, 102 (2005), [nucl-ex/0501009].

[5] M. Gyulassy and L. McLerran, Nucl. Phys. **A750**, 30 (2005), [nucl-th/0405013].

[6] B. Muller and J. L. Nagle, Ann. Rev. Nucl. Part. Sci. **56**, 93 (2006), [nucl-th/0602029].

[7] B. Muller, Acta Phys. Polon. **B38**, 3705 (2007), [0710.3366].

[8] Particle Data Group, W. M. Yao *et al.*, J. Phys. **G33**, 1 (2006).

[9] M. Gell-Mann, Austral. J. Phys. **29**, 473 (1976).

[10] W. J. Marciano and H. Pagels, Phys. Rept. **36**, 137 (1978).

[11] J. Kuti, J. Polonyi and K. Szlachanyi, Phys. Lett. **B98**, 199 (1981).

[12] L. D. McLerran and B. Svetitsky, Phys. Rev. **D24**, 450 (1981).

[13] F. Karsch and E. Laermann, hep-lat/0305025.

[14] T. D. Lee, Nucl. Phys. **A538**, 3c (1992).

[15] J. W. Harris and B. Muller, Ann. Rev. Nucl. Part. Sci. **46**, 71 (1996), [hep-ph/9602235].

[16] M. E. Peskin and D. V. Schroeder, *An Introduction To Quantum Field Theory* (Frontiers in Physics), Westview Press (1995).

[17] W. Greiner and J. Reinhardt, *Field Quantuization*, Springer-Verlag Berlin Heidelberg (1996).

[18] W. Greiner and B. Muller, *Quantum Mechanics*, Springer-Verlag Berlin Heidelberg (1994).

[19] W. Greiner and A. Schafer, *Quantum Chromodynamics*, Springer-Verlag Berlin Heidelberg (1994).

[20] H. D. Politzer, Phys. Rept. **14**, 129 (1974).

[21] K. G. Wilson, Phys. Rev. **D10**, 2445 (1974).

[22] E. Eichten, K. Gottfried, T. Kinoshita, K. D. Lane and T.-M. Yan, Phys. Rev. **D21**, 203 (1980).

[23] H. Pagels, Phys. Rev. **D19**, 3080 (1979).

[24] J. Goldstone, A. Salam and S. Weinberg, Phys. Rev. **127**, 965 (1962).

[25] M. G. Alford, K. Rajagopal and F. Wilczek, Phys. Lett. **B422**, 247 (1998), [hep-ph/9711395].

[26] J. Berges and K. Rajagopal, Nucl. Phys. **B538**, 215 (1999), [hep-ph/9804233].

[27] S. Weinberg, Muenchen 1977, 269p.

[28] B. Muller and D. K. Srivastava, nucl-th/0407010.

[29] http://www.gsi.de/fair/experiments/CBM/1intro_e.html, http://na50.web.cern.ch/NA50/physics.html .

[30] A. Chodos, R. L. Jaffe, K. Johnson, C. B. Thorn and V. F. Weisskopf, Phys. Rev. **D9**, 3471 (1974).

[31] S. Weinberg, Physica **A96**, 327 (1979).

[32] J. Gasser and H. Leutwyler, Ann. Phys. **158**, 142 (1984).

[33] J. Gasser and H. Leutwyler, Nucl. Phys. **B250**, 465 (1985).

[34] J. Gasser and H. Leutwyler, Phys. Lett. **B184**, 83 (1987).

[35] J. Gasser and H. Leutwyler, Phys. Lett. **B188**, 477 (1987).

[36] G. 't Hooft, Nucl. Phys. **B61**, 455 (1973).

[37] K. G. Wilson and J. B. Kogut, Phys. Rept. **12**, 75 (1974).

[38] http://www.lip.pt/divulgacao/quark-gluon/space_time2.html, http://na50.web.cern.ch/NA50/figures/evol.gif .

[39] M. Gyulassy and X.-N. Wang, Comput. Phys. Commun. **83**, 307 (1994), [nucl-th/9502021].

[40] X.-N. Wang, Phys. Rept. **280**, 287 (1997), [hep-ph/9605214].

[41] K. Geiger, Phys. Rept. **258**, 237 (1995).

[42] B. Muller, Int. J. Mod. Phys. **E12**, 165 (2003).

[43] E. Iancu and R. Venugopalan, hep-ph/0303204.

[44] J. D. Bjorken, Phys. Rev. **D27**, 140 (1983).

[45] R. B. Clare and D. Strottman, Phys. Rept. **141**, 177 (1986).

[46] A. Dumitru and D. H. Rischke, Phys. Rev. **C59**, 354 (1999), [nucl-th/9806003].

[47] P. F. Kolb and U. W. Heinz, nucl-th/0305084.

[48] P. Huovinen, nucl-th/0305064.

[49] T. Hirano and K. Tsuda, Phys. Rev. **C66**, 054905 (2002), [nucl-th/0205043].

[50] P. F. Kolb, J. Sollfrank and U. W. Heinz, Phys. Rev. **C62**, 054909 (2000), [hep-ph/0006129].

[51] U. W. Heinz and P. F. Kolb, Nucl. Phys. **A702**, 269 (2002), [hep-ph/0111075].

[52] U. W. Heinz and P. F. Kolb, hep-ph/0204061.

[53] F. Cooper and G. Frye, Phys. Rev. **D10**, 186 (1974).

[54] Y. Yariv and Z. Fraenkel, Phys. Rev. **C20**, 2227 (1979).

[55] J. Cugnon, Phys. Rev. **C22**, 1885 (1980).

[56] Y. Pang, T. J. Schlagel and S. H. Kahana, Phys. Rev. Lett. **68**, 2743 (1992).

[57] S. A. Bass *et al.*, Prog. Part. Nucl. Phys. **41**, 255 (1998), [nucl-th/9803035].

[58] M. Bleicher *et al.*, J. Phys. **G25**, 1859 (1999), [hep-ph/9909407].

[59] R. J. Glauber, *Lectures in Theoretical Physics*, vol.1. New York: Interscience (1959).

[60] R. J. Glauber and G. Matthiae, Nucl. Phys. **B21**, 135 (1970).

[61] PHENIX, S. S. Adler *et al.*, Phys. Rev. Lett. **91**, 072301 (2003), [nucl-ex/0304022].

[62] M. L. Miller, K. Reygers, S. J. Sanders and P. Steinberg, Ann. Rev. Nucl. Part. Sci. **57**, 205 (2007), [nucl-ex/0701025].

[63] C. W. De Jager, H. De Vries and C. De Vries, Atom. Data Nucl. Data Tabl. **14**, 479 (1974).

[64] UA5, K. Alpgard *et al.*, Phys. Lett. **B107**, 315 (1981).

[65] PHOBOS, B. B. Back *et al.*, Phys. Rev. Lett. **87**, 102303 (2001), [nucl-ex/0106006].

[66] BRAHMS, I. G. Bearden *et al.*, Phys. Rev. Lett. **88**, 202301 (2002), [nucl-ex/0112001].

[67] R. C. Hwa and K. Kajantie, Phys. Rev. **D32**, 1109 (1985).

[68] J. I. Kapusta, L. D. McLerran and D. Kumar Srivastava, Phys. Lett. **B283**, 145 (1992).

[69] PHOBOS, B. B. Back *et al.*, Phys. Rev. **C65**, 061901 (2002), [nucl-ex/0201005].

[70] J. Rafelski and B. Muller, Phys. Rev. Lett. **48**, 1066 (1982).

[71] P. Koch, B. Muller and J. Rafelski, Phys. Rept. **142**, 167 (1986).

[72] T. Matsui and H. Satz, Phys. Lett. **B178**, 416 (1986).

[73] L. D. McLerran and T. Toimela, Phys. Rev. **D31**, 545 (1985).

[74] K. Kajantie, J. I. Kapusta, L. D. McLerran and A. Mekjian, Phys. Rev. **D34**, 2746 (1986).

[75] J. I. Kapusta, P. Lichard and D. Seibert, Phys. Rev. **D44**, 2774 (1991).

[76] M. Asakawa, U. W. Heinz and B. Muller, Phys. Rev. Lett. **85**, 2072 (2000), [hep-ph/0003169].

[77] S. Jeon and V. Koch, Phys. Rev. Lett. **85**, 2076 (2000), [hep-ph/0003168].

[78] V. Koch, A. Majumder and J. Randrup, Phys. Rev. Lett. **95**, 182301 (2005), [nucl-th/0505052].

[79] M. Gyulassy and M. Plumer, Phys. Lett. **B243**, 432 (1990).

[80] M. Gyulassy, I. Vitev, X.-N. Wang and B.-W. Zhang, nucl-th/0302077.

[81] G.-Y. Qin, A. Majumder and C. Gale, Phys. Rev. **C75**, 064909 (2007), [hep-ph/0703312].

[82] G.-Y. Qin, C. Gale and A. Majumder, International Journal of Modern Physics **E16**, 2350 (2007), [hep-ph/0703026].

[83] PHENIX, K. Adcox *et al.*, Phys. Rev. Lett. **88**, 022301 (2002), [nucl-ex/0109003].

[84] STAR, C. Adler *et al.*, Phys. Rev. Lett. **89**, 202301 (2002), [nucl-ex/0206011].

[85] STAR, C. Adler *et al.*, Phys. Rev. Lett. **90**, 082302 (2003), [nucl-ex/0210033].

[86] M. Gyulassy and X.-n. Wang, Nucl. Phys. **B420**, 583 (1994), [nucl-th/9306003].

[87] A. B. Migdal, Phys. Rev. **103**, 1811 (1956).

[88] R. Baier, Y. L. Dokshitzer, A. H. Mueller, S. Peigne and D. Schiff, Nucl. Phys. **B483**, 291 (1997), [hep-ph/9607355].

[89] M. Gyulassy, P. Levai and I. Vitev, Nucl. Phys. **B594**, 371 (2001), [nucl-th/0006010].

[90] A. Kovner and U. A. Wiedemann, hep-ph/0304151.

[91] B. G. Zakharov, JETP Lett. **63**, 952 (1996), [hep-ph/9607440].

[92] W.-F. Wang, Chin. Phys. Lett. **18**, 997 (2001).

[93] P. Arnold, G. D. Moore and L. G. Yaffe, JHEP **12**, 009 (2001), [hep-ph/0111107].

[94] P. Arnold, G. D. Moore and L. G. Yaffe, JHEP **11**, 057 (2001), [hep-ph/0109064].

[95] P. Arnold, G. D. Moore and L. G. Yaffe, JHEP **06**, 030 (2002), [hep-ph/0204343].

[96] J. D. Bjorken, FERMILAB-PUB-82-059-THY.

[97] B. G. Zakharov, JETP Lett. **86**, 444 (2007), [0708.0816].

[98] T. Renk, Phys. Rev. **C76**, 064905 (2007), [0708.4319].

[99] M. G. Mustafa and M. H. Thoma, Acta Phys. Hung. **A22**, 93 (2005), [hep-ph/0311168].

[100] M. G. Mustafa, Phys. Rev. **C72**, 014905 (2005), [hep-ph/0412402].

[101] A. K. Dutt-Mazumder, J.-e. Alam, P. Roy and B. Sinha, Phys. Rev. **D71**, 094016 (2005), [hep-ph/0411015].

[102] A. Adil, M. Gyulassy, W. A. Horowitz and S. Wicks, Phys. Rev. **C75**, 044906 (2007), [nucl-th/0606010].

[103] S. Wicks and M. Gyulassy, J. Phys. **G34**, S989 (2007), [nucl-th/0701088].

[104] G.-Y. Qin, J. Ruppert, C. Gale, S. Jeon, G. D. Moore and M. G. Mustafa, Phys. Rev. Lett. **100**, 072301 (2008), [0710.0605].

[105] G.-Y. Qin, J. Ruppert, C. Gale, S. Jeon, G. D. Moore and M. G. Mustafa, 0805.4594.

[106] G.-Y. Qin, J. Ruppert, S. Turbide, C. Gale, C. Nonaka and S. A. Bass, Phys. Rev. **C76**, 064907 (2007), [0705.2575].

[107] X.-N. Wang, Z. Huang and I. Sarcevic, Phys. Rev. Lett. **77**, 231 (1996), [hep-ph/9605213].

[108] X.-N. Wang and Z. Huang, Phys. Rev. **C55**, 3047 (1997), [hep-ph/9701227].

[109] G.-Y. Qin, J. Ruppert, C. Gale, S. Jeon and G. D. Moore, (in preparation).

[110] E. V. Shuryak, Phys. Rept. **61**, 71 (1980).

[111] A. Majumder and C. Gale, Phys. Rev. **D63**, 114008 (2001), [hep-ph/0011397].

[112] A. Majumder, A. Bourque and C. Gale, Phys. Rev. **C69**, 064901 (2004), [hep-ph/0311178].

[113] J. F. Owens, Rev. Mod. Phys. **59**, 465 (1987).

[114] R. J. Fries, B. Muller and D. K. Srivastava, Phys. Rev. Lett. **90**, 132301 (2003), [nucl-th/0208001].

[115] A. von Keitz *et al.*, Phys. Lett. **B263**, 353 (1991).

[116] PHOBOS, A. Olszewski *et al.*, J. Phys. **G28**, 1801 (2002).

[117] N. Hammon, H. Stoecker and W. Greiner, Phys. Rev. **C61**, 014901 (2000), [hep-ph/9903527].

[118] A. Dumitru, D. H. Rischke, H. Stoecker and W. Greiner, Mod. Phys. Lett. **A8**, 1291 (1993).

[119] A. Dumitru *et al.*, Phys. Rev. Lett. **70**, 2860 (1993).

[120] H. Vija and M. H. Thoma, Phys. Lett. **B342**, 212 (1995), [hep-ph/9409246].

[121] C. T. Traxler, H. Vija and M. H. Thoma, Phys. Lett. **B346**, 329 (1995), [hep-ph/9410309].

[122] W. H. Furry, Phys. Rev. **56**, 1184 (1939).

[123] C. Itzykson and J. B. Zuber, *Quantum Field Theory*, McGraw Hill, New York (1980).

[124] C.-N. Yang, Phys. Rev. **77**, 242 (1950).

[125] E. Braaten and R. D. Pisarski, Nucl. Phys. **B337**, 569 (1990).

[126] M. Le Bellac, *Thermal Field Theory*, Cambridge University Press (1996).

[127] R. D. Pisarski, Nucl. Phys. **B309**, 476 (1988).

[128] C. Gale and J. I. Kapusta, Nucl. Phys. **B357**, 65 (1991).

[129] J. I. Kapusta and C. Gale, *Finite-Temperature Field Theory: Principles and Applications*, Cambridge University Press (1996).

[130] E. Braaten, R. D. Pisarski and T.-C. Yuan, Phys. Rev. Lett. **64**, 2242 (1990).

[131] S. Jeon and G. D. Moore, Phys. Rev. **C71**, 034901 (2005), [hep-ph/0309332].

[132] S. Turbide, C. Gale, S. Jeon and G. D. Moore, Phys. Rev. **C72**, 014906 (2005), [hep-ph/0502248].

[133] P. Aurenche, F. Gelis, R. Kobes and H. Zaraket, Phys. Rev. **D58**, 085003 (1998), [hep-ph/9804224].

[134] P. Aurenche, F. Gelis and H. Zaraket, JHEP **05**, 043 (2002), [hep-ph/0204146].

[135] R. Baier, D. Schiff and B. G. Zakharov, Ann. Rev. Nucl. Part. Sci. **50**, 37 (2000), [hep-ph/0002198].

[136] G.-Y. Qin, J. Ruppert, S. Turbide, C. Gale and S. Jeon, 0705.4468.

[137] C. Nonaka and S. A. Bass, Phys. Rev. **C75**, 014902 (2007), [nucl-th/0607018].

[138] K. J. Eskola, H. Honkanen, H. Niemi, P. V. Ruuskanen and S. S. Rasanen, Phys. Rev. **C72**, 044904 (2005), [hep-ph/0506049].

[139] PHENIX, S. S. Adler *et al.*, Phys. Rev. **C76**, 034904 (2007), [nucl-ex/0611007].

[140] H. Zhang, J. F. Owens, E. Wang and X.-N. Wang, Phys. Rev. Lett. **98**, 212301 (2007), [nucl-th/0701045].

[141] T. Renk and K. Eskola, Phys. Rev. **C75**, 054910 (2007), [hep-ph/0610059].

[142] J. Ruppert and T. Renk, 0710.4124.

[143] T. Renk and J. Ruppert, Phys. Rev. **C76**, 014908 (2007), [hep-ph/0702102].

[144] A. Dainese, C. Loizides and G. Paic, Eur. Phys. J. **C38**, 461 (2005), [hep-ph/0406201].

[145] A. Majumder, Phys. Rev. **C75**, 021901 (2007), [nucl-th/0608043].

[146] T. Hirano and Y. Nara, Prog. Theor. Phys. Suppl. **151**, 133 (2003).

[147] T. Renk, J. Ruppert, C. Nonaka and S. A. Bass, Phys. Rev. **C75**, 031902 (2007), [nucl-th/0611027].

[148] S. A. Bass, T. Renk, J. Ruppert and C. Nonaka, J. Phys. **G34**, S979 (2007), [nucl-th/0702079].

[149] A. Majumder, C. Nonaka and S. A. Bass, Phys. Rev. **C76**, 041902 (2007), [nucl-th/0703019].

[150] J. Sollfrank *et al.*, Phys. Rev. **C55**, 392 (1997), [nucl-th/9607029].

[151] C. M. Hung and E. V. Shuryak, Phys. Rev. **C57**, 1891 (1998), [hep-ph/9709264].

[152] D. H. Rischke, M. I. Gorenstein, H. Stoecker and W. Greiner, Z. Phys. **C51**, 485 (1991).

[153] P. F. Kolb, U. W. Heinz, P. Huovinen, K. J. Eskola and K. Tuominen, Nucl. Phys. **A696**, 197 (2001), [hep-ph/0103234].

[154] R. J. Fries, B. Muller, C. Nonaka and S. A. Bass, Phys. Rev. **C68**, 044902 (2003), [nucl-th/0306027].

[155] CTEQ, H. L. Lai *et al.*, Eur. Phys. J. **C12**, 375 (2000), [hep-ph/9903282].

[156] K. J. Eskola, V. J. Kolhinen and C. A. Salgado, Eur. Phys. J. **C9**, 61 (1999), [hep-ph/9807297].

[157] B. Jager, A. Schafer, M. Stratmann and W. Vogelsang, Phys. Rev. **D67**, 054005 (2003), [hep-ph/0211007].

[158] G. G. Barnafoldi, G. I. Fai, P. Levai, G. Papp and Y. Zhang, J. Phys. **G27**, 1767 (2001), [nucl-th/0004066].

[159] PHENIX, S. S. Adler *et al.*, Phys. Rev. Lett. **98**, 172302 (2007), [nucl-ex/0610036].

[160] B. A. Kniehl, G. Kramer and B. Potter, Nucl. Phys. **B582**, 514 (2000), [hep-ph/0010289].

[161] http://www.phenix.bnl.gov/WWW/plots/show_plot.php?editkey=p0439 .

[162] STAR, J. Adams *et al.*, Phys. Rev. Lett. **97**, 152302 (2006), [nucl-ex/0602011].

[163] A. D. Martin, R. G. Roberts, W. J. Stirling and R. S. Thorne, Phys. Lett. **B531**, 216 (2002), [hep-ph/0201127].

[164] T. Renk, hep-ph/0608333.

[165] T. Renk and J. Ruppert, Phys. Rev. **C72**, 044901 (2005), [hep-ph/0507075].

[166] M. Hirai, S. Kumano and T. H. Nagai, Phys. Rev. **C70**, 044905 (2004), [hep-ph/0404093].

[167] K. J. Eskola, K. Kajantie, P. V. Ruuskanen and K. Tuominen, Nucl. Phys. **B570**, 379 (2000), [hep-ph/9909456].

[168] R. Cutler and D. W. Sivers, Phys. Rev. **D17**, 196 (1978).

[169] B. L. Combridge, J. Kripfganz and J. Ranft, Phys. Lett. **B70**, 234 (1977).

[170] M. H. Thoma, Phys. Lett. **B273**, 128 (1991).

[171] T. Renk, Phys. Rev. **C74**, 034906 (2006), [hep-ph/0607166].

[172] K. Filimonov, Acta Phys. Hung. **A25**, 363 (2006), [nucl-ex/0505008].

[173] F. Arleo, J. Phys. **G34**, S1037 (2007), [hep-ph/0701207].

[174] S. Turbide, C. Gale, E. Frodermann and U. Heinz, Phys. Rev. **C77**, 024909 (2008), [0712.0732].

[175] P. Aurenche, R. Baier, M. Fontannaz and D. Schiff, Nucl. Phys. **B297**, 661 (1988).

[176] F. Aversa, P. Chiappetta, M. Greco and J. P. Guillet, Nucl. Phys. **B327**, 105 (1989).

[177] P. Aurenche *et al.*, Eur. Phys. J. **C9**, 107 (1999), [hep-ph/9811382].

[178] L. Bourhis, M. Fontannaz and J. P. Guillet, Eur. Phys. J. **C2**, 529 (1998), [hep-ph/9704447].

[179] PHENIX, S. S. Adler *et al.*, Phys. Rev. Lett. **98**, 012002 (2007), [hep-ex/0609031].

[180] PHENIX, A. Adare *et al.*, 0804.4168.

[181] PHENIX, S. S. Adler *et al.*, Phys. Rev. **C69**, 034909 (2004), [nucl-ex/0307022].

[182] PHENIX, S. S. Adler *et al.*, Phys. Rev. **C69**, 034910 (2004), [nucl-ex/0308006].

[183] PHENIX, T. Isobe, J. Phys. **G34**, S1015 (2007), [nucl-ex/0701040].

[184] X.-N. Wang, Phys. Lett. **B595**, 165 (2004), [nucl-th/0305010].

[185] X.-N. Wang, Phys. Lett. **B579**, 299 (2004), [nucl-th/0307036].

[186] M. Nguyen, talk in Quark Matter 2008 Conference for PHENIX, *High p_T direct photon-hadron correlations using the PHENIX detector* (2008), [0805.1225].

[187] J. Frantz, talk in Hard Probes 2008 Conference for PHENIX, *Two-particle direct photon-jet correlation measurement in PHENIX* (2008).

[188] A. M. Hamed, talk in Quark Matter 2008 Conference for STAR, *Probing the medium with γ-jet correlation measurements*; talk in Hard Probes 2008 Conference for STAR, *Direct γ-charged hadron azimuthal correlation measurements* (2008), [0806.2190].